



저작자표시-비영리-변경금지 2.0 대한민국

이용자는 아래의 조건을 따르는 경우에 한하여 자유롭게

- 이 저작물을 복제, 배포, 전송, 전시, 공연 및 방송할 수 있습니다.

다음과 같은 조건을 따라야 합니다:



저작자표시. 귀하는 원저작자를 표시하여야 합니다.



비영리. 귀하는 이 저작물을 영리 목적으로 이용할 수 없습니다.



변경금지. 귀하는 이 저작물을 개작, 변형 또는 가공할 수 없습니다.

- 귀하는, 이 저작물의 재이용이나 배포의 경우, 이 저작물에 적용된 이용허락조건을 명확하게 나타내어야 합니다.
- 저작권자로부터 별도의 허가를 받으면 이러한 조건들은 적용되지 않습니다.

저작권법에 따른 이용자의 권리는 위의 내용에 의하여 영향을 받지 않습니다.

이것은 [이용허락규약\(Legal Code\)](#)을 이해하기 쉽게 요약한 것입니다.

[Disclaimer](#)

Doctoral Thesis

**HYBRID NANOSTRUCTURED MATERIALS
FOR SUPERCAPACITORS**

Suresh Kannan Balasingam

Department of Chemistry

Graduate School of UNIST

2016

HYBRID NANOSTRUCTURED MATERIALS FOR SUPERCAPACITORS

Suresh Kannan Balasingam

**Department of Chemistry
Graduate School of UNIST**

Hybrid Nanostructured Materials for Supercapacitors

A dissertation
submitted to the Graduate School of UNIST
in partial fulfillment of the
requirements for the degree of
Doctor of Philosophy

Suresh Kannan Balasingam

01.13.2016

Approved by



Advisor

Prof. Jae Sung Lee

Hybrid Nanostructured Materials for Supercapacitors

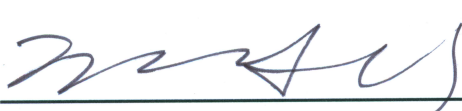
Suresh Kannan Balasingam

This certifies that the dissertation of Suresh Kannan Balasingam is
approved.

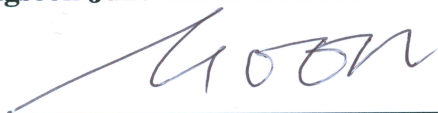
01. 13. 2016



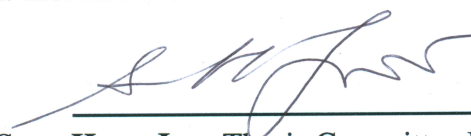
Advisor: Prof. Jae Sung Lee



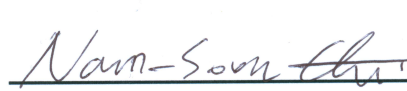
Prof. Yongseok Jun: Thesis Committee Member#1



Prof. Hoi Ri Moon: Thesis Committee Member#2



Prof. Sang Hoon Joo: Thesis Committee Member#3



Prof. Nam-Soon Choi: Thesis Committee Member#4

Dedication

To my beloved mother

Abstract

The recent development of modern electronic devices and the progressive research on renewable energy-based electrochemical energy conversion systems have fuelled the drive toward advanced high-performance energy storage devices. Among the various types of energy storage devices, supercapacitors have been recognized as one of the most promising candidates for high-power applications due to their outstanding properties, including high power density, long cycle life, fast charge/discharge rate, and better safety. Basically, carbon materials are best known for their double layer capacitance behavior, which provides the high power density to the capacitors. Also, pseudocapacitors (metal oxides, polymers, metal sulfides and metal selenide) generally have high specific capacitance. However, the low specific capacitance of carbon-based materials and the poor cycling stability and low conductivity of the pseudocapacitive materials limits the effective utilization of these electroactive materials in the energy storage field. To enhance the energy density of supercapacitors, suitable pseudocapacitance materials have been under progressive research. The suitable pseudocapacitance materials having good electrical conductivity and high surface area is one of the key issues in the field of supercapacitor. Also, the nanostructured electrode-electrolyte interface is the heart of every supercapacitor, which determines energy storage capacity of the device. With the above motivation of enhanced electrochemical performance as well as to overcome those issues, the design of a hybrid nanostructure based on metal oxide, metal sulfide and metal selenides with a carbon matrix have been intensively studied in this thesis. The hierarchical hybrid nanostructures combining of EDLCs and pseudocapacitors have large surface area, good electrical conductivity, and short path for ion diffusion. All the electroactive materials were synthesized using hydrothermal method with various conditions. The physico-chemical properties of as-synthesized nanomaterials are investigated in detail and its effect on electrochemical performance and charge storage behavior are also explored.

Part-I of this dissertation covers the synthesis and electrochemical characterization of vanadium pentoxide nanobelts and high electrical conductivity graphene decorated vanadium pentoxide nanobelts. The various ratio of graphene to vanadium pentoxide was tailored and the corresponding charge storage behavior are studied in detail. Among the V_xG_y group of electro-active materials, the vanadium-rich composite V_3G_1 showed the maximum C_s value of around 288 F g^{-1} at the scan rate of 10 mV s^{-1} and excellent cyclic stability; the capacitance retention of about 82%, even after 5000 cycles in three electrode system.

To improve the surface area and the effective utilization of electrolyte ions to all the electroactive surfaces, a layered two dimensional materials were synthesized, characterized and evaluated as supercapacitor electrodes in part-II. Mainly focuses on the molybdenum disulfide (MoS_2), molybdenum diselenide (MoSe_2) based TMDCs and its corresponding composites with various carbon materials such as graphene and carbon fiber paper (CFP). When compared to TMDCs, transition metal oxides (TMOs) have good stability, high pseudocapacitance etc., However, the electrical conductivity of oxides are comparatively lower than the TMDCs.

The performance of the high surface area MoS₂ sponge electrode material was tested by assembling a symmetric supercapacitor with an aqueous electrolyte. The symmetric cell exhibited a device and single electrode capacitance is 128 F g⁻¹ and 510 F g⁻¹ at a scan rate of 2 mV s⁻¹, which is the highest value reported to date for this material. In addition, the symmetric supercapacitor revealed a high energy density of approximately 6.15 Wh kg⁻¹ and good cyclic stability over 4000 cycles. The amorphous MoS_x thin film coated carbon fiber paper (CFP/a-MoS_x) as a binder-free three-dimensional (3-D) electrode was delivered a device capacitance value of 41.96 mF cm⁻² at a scan rate of 1 mV s⁻¹. More interestingly, the long term cycle test showed the substantial increase in capacitance retention of up to 600% for 4750 cycles is obtained. The increasing in specific capacitance trends indicates the electroactivation process, allowing more effective intercalation of cations between the layers (exfoliation of 2D materials).

The electrochemical energy-storage behavior of MoSe₂ nanosheets and its carbon matrix was investigated for supercapacitor applications using symmetric cell configuration is discussed in the last section. The MoSe₂ nanosheets electrode exhibited a maximum specific capacitance of 198.9 F g⁻¹ and the symmetric device showed 49.7 F g⁻¹ at a scan rate of 2 mV s⁻¹ with capacitance retention of approximately 75% was observed even after 10,000 cycles at a high charge–discharge current density of 5 A g⁻¹. The MoS₂/rGO nanosheets electrode exhibited a specific capacitance of 211 F g⁻¹ with excellent cycling stability (180% capacitance retention for 10,000 cycles), compared to its pristine MoSe₂. The amorphous MoSe_x nanostructures (nanoneedles and nanoparticles) were grown on carbon fiber paper 3D substrate. There were two different pre-treatment methods (plasma cleaning and electro etching) were employed to induce the hydrophilicity of CFP. Interestingly, different pre-treatment methods induced the formation of different MoSe_x) nanostructure formation on the CFP. The amorphous MoSe_x) coated CFP electrodes were tested for the supercapacitor applications. The surface pre-treatment played an important role on the electrochemical performance. The overall enhanced electrochemical performance of the hybrid nanostructure electrode is mainly attributed to the improved electron and ion transfer mechanism involving synergistic effects of both the pseudocapacitance and the electric double layer charge-storage behavior. These results demonstrate that enhanced electrochemical performance of hybrid nanostructure electrode based on layered transition metal compounds with carbon matrix has the great potential application for next generation high-performance supercapacitor devices.

Keywords: Supercapacitor, Reduced graphene oxide, Transition metal dichalcogenides, Vanadium pentoxide, Molybdenum disulfide, Molybdenum diselenide and Energy storage device

Contents

Abstract	iii
List of Figures	x
1 Introduction	1
1.1 Global Energy Crisis and the Significance of Energy Storage Devices	1
1.2 Principle and Reaction Mechanism of Supercapacitors	2
1.2.1 Electrochemical double layer capacitors (EDLCs)	2
1.2.2 Pseudocapacitors	3
1.2.3 Hybrid supercapacitors	5
1.3 Primary Objectives of Present Work	7
References	7
2 Material Synthesis, Physico-chemical and Electrochemical Characterizations	10
2.1 Materials Synthesis	10
2.1.1 Hydrothermal synthesis of nanomaterials	10
2.1.2 Synthesis of graphene oxide by modified Hummer's method	10
2.2 Physico-chemical Characterization	11
2.2.1 X-ray diffraction	11
2.2.2 Raman spectroscopy	11
2.2.3 Field-emission scanning electron microscopy	12
2.2.4 High-resolution transmission electron microscopy	12
2.2.5 X-ray photoelectron spectroscopy	12
2.3 Electrode Fabrication and Symmetric Cell Assembly	12
2.3.1 Electrode fabrication	12
2.3.2 Symmetric cell assembly	13
2.4 Electrochemical Characterization	13
2.4.1 Cyclic voltammetry	13
2.4.2 Galvanostatic charge/discharge	13
2.4.3 Electrochemical impedance spectroscopy	13
2.5 Calculation of Electrode and Symmetric Cell Performance	14
2.5.1 A single electrode performance using three-electrode setup	14
2.5.2 Symmetric cell and its single electrode performance using two-electrode setup	15
References	16

I Nanostructured Transition Metal Oxide/Carbon Electrodes	17
3 Graphene Decorated V₂O₅ Nanobelts*	18
3.1 Introduction	18
3.2 Experimental	19
3.2.1 Preparation of graphene oxide and reduced graphene oxide	19
3.2.2 Synthesis of graphene decorated V ₂ O ₅ nanobelt composites	19
3.2.3 Materials characterization	20
3.2.4 Electrochemical characterization	20
3.3 Results and Discussion	20
3.3.1 Physico-chemical analysis	20
3.3.2 Electrochemical performance	24
3.4 Summary	28
References	28
II Nanostructured Transition Metal Dichalcogenides/rGO Electrodes	34
4 Freeze-dried MoS₂ Nanosheets	35
4.1 Introduction	35
4.2 Experimental	35
4.2.1 Synthesis of MoS ₂ sponge material	35
4.2.2 Materials characterization	37
4.2.3 Cell fabrication and electrochemical measurement of supercapacitors	37
4.3 Results and Discussion	37
4.3.1 Physico-chemical analysis	37
4.3.2 Electrochemical performance of symmetrical cells	38
4.4 Summary	43
References	43
5 Amorphous MoS_x Thin-layer Coated Carbon Fiber Paper	47
5.1 Introduction	47
5.2 Experimental	48
5.2.1 Synthesis of amorphous-MoS _x on carbon fiber paper	48
5.2.2 Material characterization	48
5.3 Results and Discussion	48
5.3.1 Physico-chemical analysis	48
5.3.2 Electrochemical performance of symmetric cells	51
5.4 Summary	56
References	57
6 A Few-layered MoSe₂ Nanosheets*	59
6.1 Introduction	59

6.2	Experimental	60
6.2.1	Material synthesis	60
6.2.2	Materials characterization	60
6.2.3	Cell fabrication and electrochemical measurements	60
6.3	Results and Discussion	61
6.3.1	Physico-chemical analysis	61
6.3.2	Electrochemical performance of symmetrical cells	63
6.4	Summary	68
	References	68
7	MoSe₂/rGO Hybrid Nanosheets Electrode	73
7.1	Introduction	73
7.2	Experimental	75
7.2.1	Synthesis of MoSe ₂ /reduced graphene oxide nanosheets	75
7.2.2	Materials characterization	75
7.2.3	Electrochemical characterization	75
7.3	Results and Discussion	76
7.3.1	Physico-chemical analysis	76
7.3.2	Electrochemical performance of MoSe ₂ /rGO and MoSe ₂ electrodes	78
7.4	Summary	83
	References	84
8	Amorphous MoSe_x Nanostructures Coated Carbon Fiber Paper	89
8.1	Introduction	89
8.2	Experimental	90
8.2.1	Synthesis of amorphous MoSe _x nanostructures coated carbon fiber paper	90
8.2.2	Materials characterization	90
8.2.3	Cell fabrication and electrochemical characterization	90
8.3	Results and Discussion	91
8.3.1	Physico-chemical analysis	91
8.3.2	Electrochemical performance	92
8.4	Summary	101
	References	102
9	Concluding Remarks and Future Prospects	104
	Appendix A Graphene Decorated V₂O₅ Nanobelts	106
A.1	Raman spectrum of GNVNs	106
A.2	XPS spectra of V2p	106
A.3	XPS spectra of C1s	107
A.4	AFM image of GNVNs	107
	Appendix B Freeze-dried MoS₂ Nanosponges	108

B.1 SEM images of normal-dried MoS ₂ particles and freeze-dried MoS ₂ sponge materials	108
Appendix C Amorphous MoS_x Thin-layer Coated CFP	109
C.1 XRD pattern of amorphous MoS _x thin film coated CFP	109
C.2 Raman spectrum of amorphous MoS _x thin film coated CFP	110
List of Publications	111
Acknowledgments	113

List of Figures

1.1	Helmholtz double-layer model.	2
1.2	Guoy-Chapman diffused layer model.	3
1.3	Stern model showing the Stern plane marks the distance of closest approach of ions to the charged electrode surface.	3
1.4	Schematic representation of EDLCs showing charged (top) and discharged state (bottom).	4
1.5	Underpotential deposition of lead on gold electrode surface.	5
1.6	Redox pseudocapacitance of protons on the RuO ₂ electrode surface.	6
1.7	Intercalation pseudocapacitance of lithium ions into the Nb ₂ O ₅ layered host electrode.	6
2.1	Schematic illustration of laboratory scale autoclave.	11
3.1	Schemes (a) and (b) represent the absence of nanobelts formation in case of rGO addition and without carbon material, respectively, via low-temperature hydrothermal synthesis. Scheme (c) represents the formation of GNVNs by mixing of GO into VO dispersion under the same hydrothermal conditions.	21
3.2	SEM images of (a) pristine VO particles, (b) VO after the hydrothermal treatment, (c) VO with rGO after the hydrothermal treatment, and calcined GNVNs with the following ratios of VO and GO: (d) 3:1, (e) 1:1, and (f) 1:3.	22
3.3	XRD spectra of pristine V ₂ O ₅ , composite GNVNs, and rGO measured in the 2θ range of 5° to 60°.	23
3.4	BF-TEM image of VNB and corresponding SAED (inset) (a), HAADF-STEM image of VNB (b), the corresponding EELS elemental mapping of vanadium (c) and carbon (d), and EELS spectrum (e) acquired at the point of Fig. (d).	23
3.5	(a) CV curves of rGO, pristine VO particles, V ₁ G ₃ , V ₁ G ₁ , and V ₃ G ₁ electroactive materials measured at a scan rate of 10 mV s ⁻¹ in 1 M Na ₂ SO ₄ solution; (b) CV curves of the V ₃ G ₁ electrode measured at different scan rates ranging from 5 to 125 mV s ⁻¹ ; and (c) Specific capacitance calculated from the CV curves of Fig. (b) of the V ₃ G ₁ electrode at various scan rates.	26

- 3.6 (a) Galvanostatic charge-discharge curves of rGO, pristine VO particles, V_1G_3 , V_1G_1 , and V_3G_1 electroactive materials measured at a constant current density of 0.5 A g^{-1} in $1 \text{ M Na}_2\text{SO}_4$ solution; (b) Galvanostatic charge-discharge curves of V_3G_1 electrode material measured at various current densities; and (c) Electrochemical impedance spectra of rGO pristine V_2O_5 particles, V_1G_3 , V_1G_1 , and V_3G_1 electroactive materials measured in $1 \text{ M Na}_2\text{SO}_4$ solution. The inset shows an enhanced view of the high-to-medium frequency region. 27
- 3.7 (a) Specific capacitance retention of the V_3G_1 electrode as a function of cycle number, measured by CV at a scan rate of 200 mV s^{-1} in $1 \text{ M Na}_2\text{SO}_4$ solution; and (b) EIS analysis of the V_3G_1 electrode at the initial stage and after 5000 cycles. 28
- 4.1 Schematic illustration of the synthesis of MoS_2 sponge material by the hydrothermal method followed by freeze-drying. 36
- 4.2 XRD spectrum of as-synthesized MoS_2 sponge materials. 38
- 4.3 Raman spectrum of the MoS_2 sponges showing A_{1g} and E_{2g}^1 Raman modes. 38
- 4.4 FE-SEM images of MoS_2 sponges at low (top left) and higher magnification (top right). TEM images of MoS_2 sponges at low (bottom left) and high magnification (bottom right) with inset indicating the FFT pattern. 39
- 4.5 Cyclic voltammograms of MoS_2 sponge electrode-based symmetric cells measured at various scan rates from 2 mV s^{-1} to 125 mV s^{-1} . 40
- 4.6 Specific gravimetric capacitance of a single electrode versus scan rate. 40
- 4.7 Charge-discharge curves of MoS_2 sponge electrode-based symmetric cells measured at different current densities. 41
- 4.8 Specific gravimetric capacitance of a single electrode at various current densities (0.01 A g^{-1} to 3 A g^{-1}), derived from charge-discharge measurements. 41
- 4.9 Ragone plot of a symmetric device showing the gravimetric energy and power densities. 42
- 4.10 Nyquist plot from the EIS measurements (the inset shows the high frequency region). 42
- 4.11 Long term cycling stability of the device at a current density of 2 A g^{-1} . 43
- 5.1 SEM images of bare CFP at (a) low magnification and (b) high magnification, and SEM images of CFP/a- MoS_x at (c) low magnification and (d) high magnification. 49
- 5.2 (a) HR-TEM cross-sectional image of CFP/a- MoS_x with inset displaying the FFT pattern; (b) HAADF-STEM cross-sectional image of CFP/a- MoS_x where the area within green dotted rectangle indicates the thin layer of MoS_x ; and (c) a small area EDS spectrum of MoS_x taken at the red highlighted square in Fig. (b). 50
- 5.3 STEM image and elemental maps of CFP/a- MoS_x . Reprinted with permission from [2]. Copyright 2015 American Chemical Society. 50
- 5.4 High resolution XPS spectra of (a) Mo 3d, and (b) S 2p regions of a- MoS_x . 51
- 5.5 CV curves of CFP/a- MoS_x at various scan rates ranging from 1 mV s^{-1} to 125 mV s^{-1} . 52
- 5.6 Relationship between specific capacitance of electrode and scan rate. 53
- 5.7 Charge-discharge curves of CFP/a- MoS_x at current densities. 53
- 5.8 Relationship between specific capacitance of electrode and current densities. 54

5.9	EIS spectrum of the symmetric supercapacitor with inset showing the high-frequency region.	55
5.10	Long term stability of device measured as a function of capacitance retention vs. cycle number.	56
5.11	CV curves of 1 st cycle and after 4750 cycles of long term stability test.	56
6.1	XRD spectrum of MoSe ₂ nanosheets.	61
6.2	Raman spectrum of MoSe ₂ nanosheets showing two distinct A _{1g} and E _{2g} ¹ Raman modes.	61
6.3	(a) High resolution XPS spectra of Mo 3d, and (b) Se 3d regions of MoSe ₂ nanosheets.	62
6.4	TEM images of MoSe ₂ nanosheets. (a) and (b) show low magnification, (c) high magnification; and inset of (c) shows the FFT pattern.	63
6.5	(a) Cyclic voltammograms of MoSe ₂ nanosheets in 0.5 M H ₂ SO ₄ electrolyte measured at different scan rates ranging from 2 mV s ⁻¹ to 125 mV s ⁻¹ , and (b) Specific capacitance value calculated from the CV curves of Fig (a) at different scan rates.	64
6.6	(a) Galvanostatic charge-discharge curves of MoSe ₂ nanosheets in 0.5 M H ₂ SO ₄ electrolyte measured at different current densities ranging from 0.1 A g ⁻¹ to 5 A g ⁻¹ , and (b) Specific capacitance value calculated from the CD curves of Fig. (a) at different current densities.	65
6.7	(a) Specific capacitance retention of the MoSe ₂ nanosheets as a function of cycle number, measured by charge-discharge at a high current density of 5 A g ⁻¹ in 0.5 M H ₂ SO ₄ electrolyte, and (b) Electrochemical impedance spectra of a symmetric device measured at the initial stage and after 10000 cycles (The inset shows an enhanced view of the high-to-medium frequency region).	67
7.1	XRD spectrum of MoSe ₂ /reduced graphene oxide nanosheets.	76
7.2	Raman spectrum of MoSe ₂ /reduced graphene oxide nanosheets.	77
7.3	FE-SEM images of MoSe ₂ /rGO nanosheets at (a) lower and (b) higher magnifications.	77
7.4	XPS spectra of MoSe ₂ /reduced graphene oxide nanosheets (a) survey, (b) Mo 3d, (c) Se 3d, and (d) C 1s .	78
7.5	Cyclic voltammetry curves of MoSe ₂ and MoSe ₂ /rGO nanosheets electrodes at a scan rate of 25 mV s ⁻¹ .	79
7.6	CV curves of MoSe ₂ /rGO nanosheets electrode at various scan rates	80
7.7	Specific capacitance of MoSe ₂ and MoSe ₂ /rGO nanosheets electrodes at different scan rates.	80
7.8	Galvanostatic charge-discharge curves of MoSe ₂ and MoSe ₂ /rGO nanosheets electrodes.	81
7.9	GCD curves of MoSe ₂ /rGO nanosheets electrode at different current densities.	81
7.10	Specific capacitance vs. current density of MoSe ₂ /rGO nanosheets electrode.	82
7.11	Cycling performance of MoSe ₂ /rGO nanosheets electrode at 5 A g ⁻¹ for 10,000 cycles. The inset shows the charge-discharge curves of the initial and the final four cycles.	83
7.12	Nyquist plots of MoSe ₂ and MoSe ₂ /rGO nanosheets at the initial cycle and after 10000 cycles. The inset indicates the magnified portion of the high-frequency EIS.	84

8.1	FE-SEM images of (a-c) PC-CFP/a-MoSe _x and (d-f) EE-CFP/a-MoSe _x at different magnifications.	91
8.2	XRD pattern of bare CFP and EE-CFP/a-MoSe _x	92
8.3	Raman spectra of bare CFP and EE-CFP/a-MoSe _x	92
8.4	XPS spectra of (a) survey, (b) Mo 3d, (c) Se 3d and (d) C 1s for EE-CFP/a-MoSe _x	93
8.5	Cyclic voltammetry curves of CFP, PC-CFP/a-MoSe _x and EE-CFP/a-MoSe _x at a scan rate of 5 mV s ⁻¹	93
8.6	Galvanostatic charge/discharge curves of CFP, PC-CFP/a-MoSe _x and EE-CFP/a-MoSe _x at a current density of 0.1 mA cm ⁻² .	94
8.7	Cyclic voltammetry profiles (a) and specific capacitances (b) of PC-CFP/a-MoSe _x -based supercapacitors at various scan rates,	95
8.8	GCD curves (a) and specific capacitances (b) of PC-CFP/a-MoSe _x -based supercapacitors at various current densities.	96
8.9	Cyclic voltammetry curves (a) and specific capacitances (b) of EE-CFP/a-MoSe _x -based supercapacitors at various scan rates	98
8.10	GCD curves (a) and specific capacitances (b) of EE-CFP/a-MoSe _x -based supercapacitors at various current densities.	99
8.11	(a) Cycling performance of PC-CFP/a-MoSe _x -based supercapacitors. (b) EIS spectra of before and after 10000th cycles; inset is the magnified portion of high-frequency region.	100
8.12	(a) Cycling performance of EE-CFP/a-MoSe _x -based supercapacitors. (b) EIS spectra of EE-CFP/a-MoSe _x -based supercapacitors before and after 25000th cycles; inset is the magnified portion of high-frequency region.	101
A.1	Raman spectra of (a) GVNBS (V ₃ G ₁) composites and (b) comparison between the G bands of rGO and GVNBS composites.	106
A.2	XPS spectrum of (a) V ₂ O ₅ raw particles, (b) V ₂ O ₅ mixed with GO in DI water after 1 day, (c) GVNBS (V ₃ G ₁) after hydrothermal treatment.	106
A.3	C1s XPS spectra of (a) GO before the hydrothermal treatment, (b) GO without V ₂ O ₅ after the hydrothermal treatment, (c) mixture of GO and V ₂ O ₅ (V ₃ G ₁) after the hydrothermal treatment.	107
A.4	(a) AFM image of GVNBS prepared in the ratio V ₃ G ₁ , (b) thickness analysis along the white line shown in frame (a), and (c) surface topographical AFM image of GVNBS.	107
B.1	Scanning electron microscopic images of hydrothermally synthesized MoS ₂ material. The agglomerated MoS ₂ microparticles obtained by the normal air-drying method at various levels of magnification are shown in (a)-(d). The high surface area MoS ₂ sponge electrodes obtained by freeze-drying method at various magnifications are shown in (e)-(f). For comparison purposes, similar scale bars are used.	108
C.1	X-ray diffraction pattern of CFP/a-MoS _x showing the characteristic peak of CFP. No characteristic peaks of MoS ₂ are observed.	109
C.2	Raman spectrum of CFP/a-MoS _x . No distinctive Raman active modes of MoS ₂ are observed.	110

CHAPTER 1

Introduction

1.1 Global Energy Crisis and the Significance of Energy Storage Devices

Ensuring the availability of energy is a serious concern faced worldwide, and therefore, alternative energy-conversion systems based on renewable energy sources (solar, wind, hydroelectric, geothermal, and biomass etc.) have been in the focus of research. The transportation of that kind of sustainable energy from the point of generation to the end user is yet another challenging task that involves power grids for large-distance and high-capacity energy-storage devices for small-scale and mobile applications [1]. Moreover, the intermittent nature of such renewable energy resources (for example, the availability of sunlight only in day time, seasonal wind flow etc.), an efficient energy storage devices are in demand in order to store the excess energy and then weehile releasing it when in high demand. Therefore, the energy storage devices play a vital role to promote the entire reliability and effective usage of whole renewable energy based power system from the point of generation through transmission and then distribution to the end user[2].

In recent years, the discovery of modern electronic devices also a requires advanced high-performance energy storage devices. To date batteries and electrochemical capacitors are considered as most promising energy storage devices available in the market. The key difference between batteries and electrochemical capacitors are based on the different electrochemical charge storage mechanism. Batteries stores the electrical energy via faradaic redox reaction, when charging Li^+ ions move from anode to cathode through a separator, while discharging the Li^+ ions move to the opposite way (from cathode to anode) and the discharge current flows through the external circuit [3]. In day to day life, batteries play vital role in all portable electronic/medical devices, automobiles, industrial equipments etc., due to its light weight, high energy density and recharging option without memory effect. Although batteries having high energy density which can be useful for small-scale applications, however, they are limited by a low power density, slow charge/discharge rate, short cycle life, physical/chemical change of electrode materials and its crystal structure between the charge and discharge state [4]. On the other hand, traditional capacitors are best known for their high power density, but have a fundamental flaw in their low energy density [5]. By combining the figure of merit of these two systems, supercapacitors (also known as ultracapacitors or electrochemical capacitors, ECs) are being developed, resulting in higher power density and energy density than conventional batteries and traditional capacitors, respectively. The long cycle life and short charging time of supercapacitors are considered to be some of the important merits rather than batteries [6].

1.2 Principle and Reaction Mechanism of Supercapacitors

In a typical Electrochemical capacitors consists of a pair of polarizable electrodes attached on a current collector substrate (positive and negative electrode), a dielectric porous separator and aqueous or organic/ionic liquid based electrolyte, which resembles a battery structure. When the voltage is applied between the electrode terminals, the electrodes attracts the oppositely charged ions, for example the positive electrode attracts the negative ions from the electrolyte and negative electrode attracts positive ions as counter reaction. The charges accumulate on the both electrode surface releases electrical energy while discharging. The charge storage mechanism of electrochemical capacitors are divided into two types (i) electrochemical double-layer capacitance and (ii) pseudocapacitance [7]

1.2.1 Electrochemical double layer capacitors (EDLCs)

Basically, carbon materials are best known for their double layer capacitance behavior, in which the electrical energy stores via electrostatic accumulation of ions on the surface of carbon pores [8]. The concept of double layer represents the two array layers of opposite charges separated at the electrode/electrolyte interface during the polarization of constant electrode surface area A (m^2). This model was first proposed by von Helmholtz, which describes that under the polarization, the ions of opposite charge diffuse via the electrolyte to form a condensed layer (with a thickness of few nanometer) which is parallel to the electrode [9]. This phenomenon of accumulation of charges on the electrode surface is called as electrical double layer (EDL). Figure. 1.1 represents the compact structure of Helmholtz double layer model.

Since the Helmholtz double layer model does not consider the diffusion limitation of ions in the electrolyte solution and the interaction between the dipole moment of solvent on the electrolyte ions and the electrode, Guoy-Chapman diffuse layer model was proposed in which the electrolyte ions are solvated and they are not arranged in a perfect plane [9]. Instead, the solvated ions are diffuse from the electrode surface to the bulk electrolyte based on the exponential potential difference from the electrode to bulk liquid as shown in Fig. 1.2. since Guoy-Chapman model is insufficient to explain the highly charge doble layers, In 1924, Stern proposed a hybrid model which is the combination of Helmholt and Guoy-Chapman models [9]. He included the hydrodynamic motion of ionic species in the diffusion layer and the accumulation of ions close to the electrode surface as shown in Fig. 1.3.

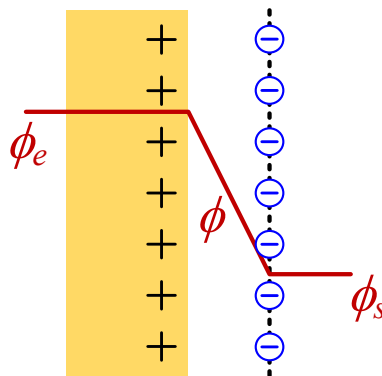


Fig. 1.1 Helmholtz double-layer model.

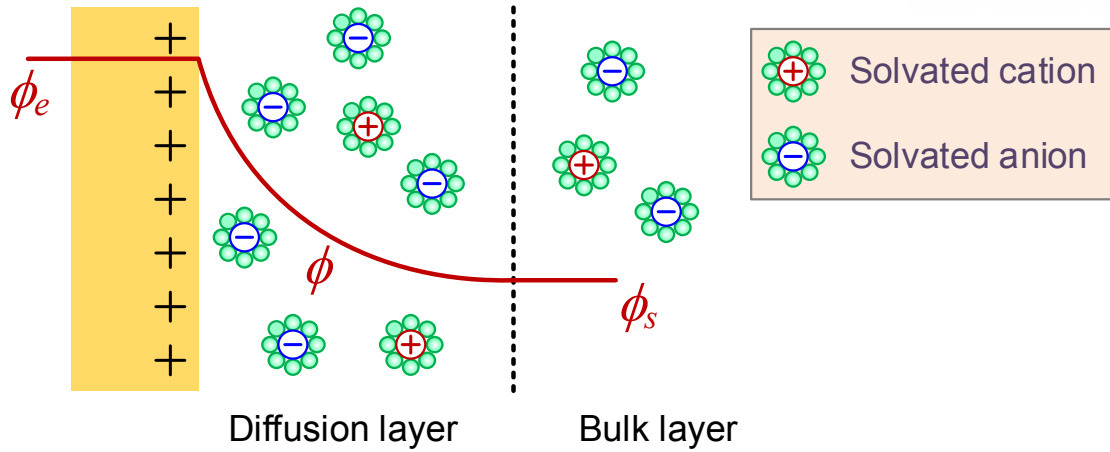


Fig. 1.2 Guoy-Chapman diffused layer model.

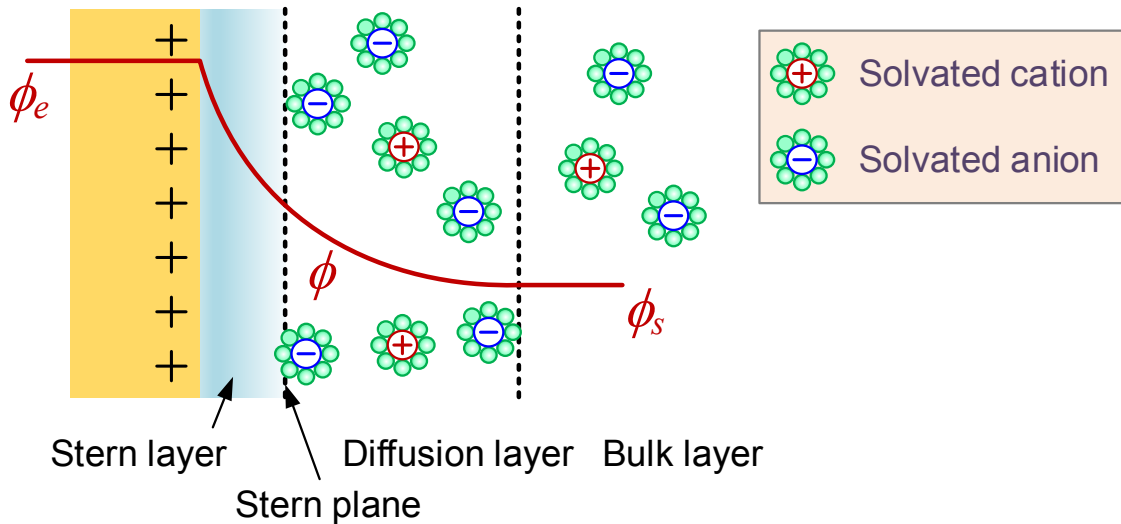


Fig. 1.3 Stern model showing the Stern plane marks the distance of closest approach of ions to the charged electrode surface.

In case of symmetric capacitors, two porous carbon based electrodes assembled with a porous separator immersed in an electrolyte medium, when the potential applied between two electrodes, the positively charged ions are attracted towards negative electrode, simultaneously negatively charged ions are moved towards positive electrode while in charged state as shown in Fig. 1.4 (top). while discharging, the electrons are moving from anode to cathode the external circuit via load, and the electrolyte ions are moving opposite manner as shown in Fig. 1.4 (bottom).

1.2.2 Pseudocapacitors

Pseudocapacitor, where the energy is stored through fast reversible redox reactions between the electrolyte and the electroactive species on the electrode surface [10]. The accumulation of electrons at the electrode is a Faradaic process where the electrons generated by the redox reaction are transferred across the electrolyte/electrode interface. Unlike redox process in battery, the Faradaic processes in a pseudocapacitor are arises due to the thermodynamic change of potential (δV) during charge accumulation (δQ)

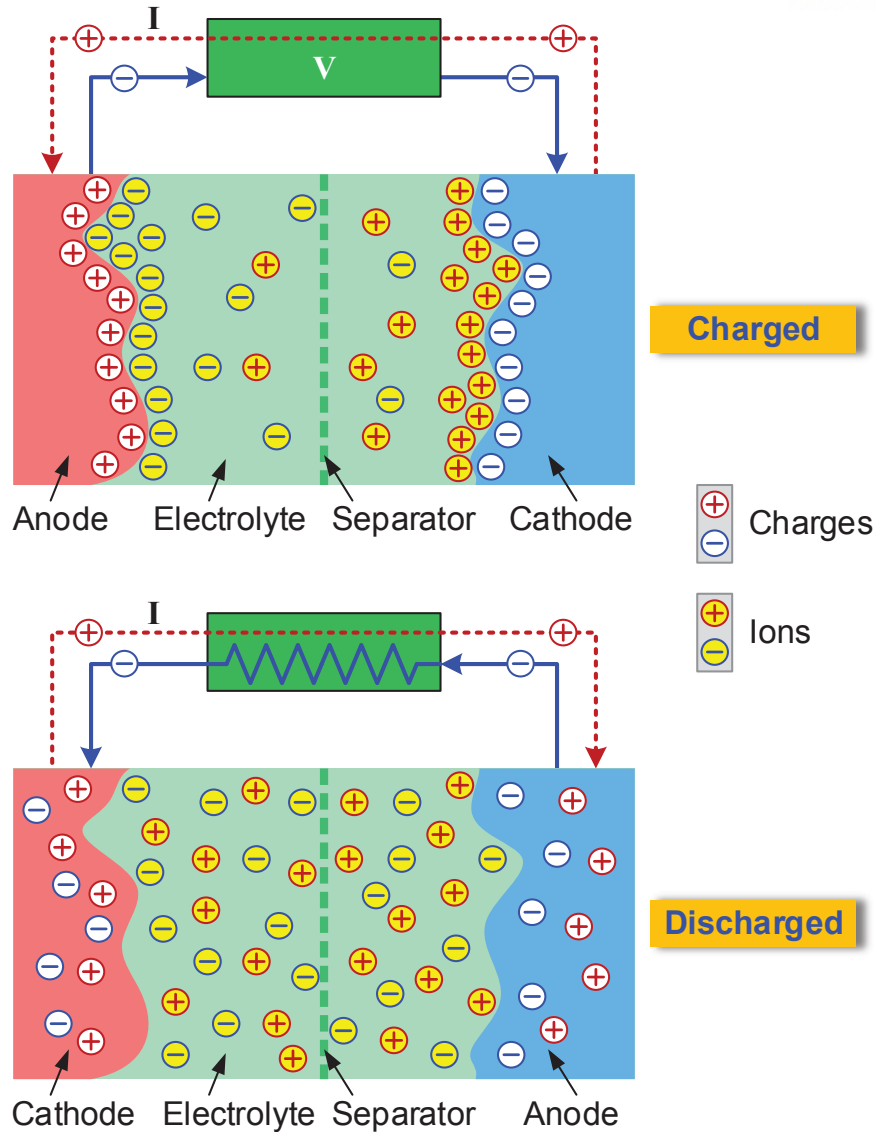


Fig. 1.4 Schematic representation of EDLCs showing charged (top) and discharged state (bottom).

and have better reversibility. The derivative $C = d(\delta Q)/d(\delta V)$ corresponds to the capacitance, which is referred to as pseudocapacitance. The theoretical pseudo-capacitance of metal oxide can be calculated using the Eq. (1.1)

$$C = \frac{nF}{MV} \quad (\text{F}) \quad (1.1)$$

where n is the mean number of the electrons transferred in the redox reaction, F is the Faraday constant, M is the molar mass of the metal oxide and V is the operating potential window

1.2.2.1 Types of pseudocapacitive mechanisms

The capacitive behavior of electrochemical system is due to the following faradaic mechanisms: (i) under potential deposition, (ii) redox pseudocapacitance, and (iii) intercalation pseudocapacitance, which have

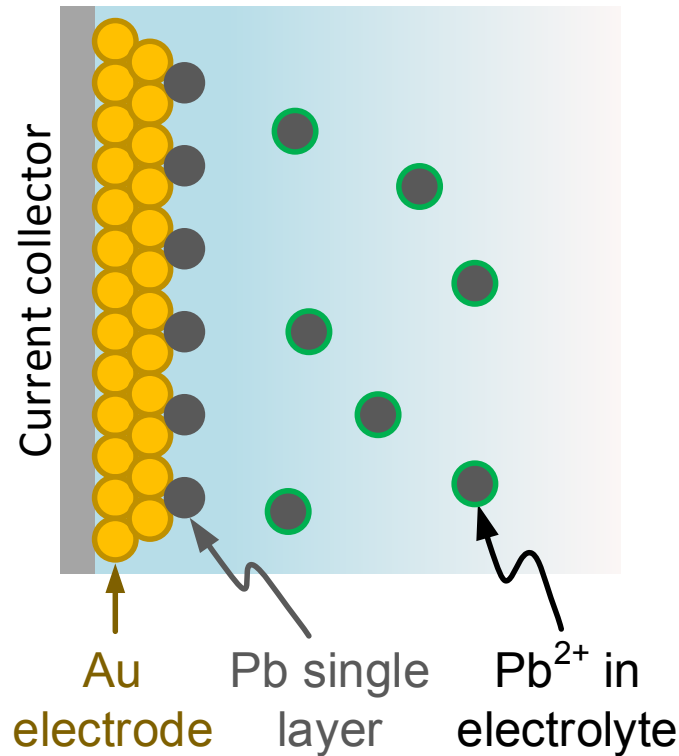


Fig. 1.5 Underpotential deposition of lead on gold electrode surface.

been identified by Conway [9]. Under potential deposition occurs due to the adsorption of monolayer at a surface of metal electrode well above its redox potential. Figure. 1.5 shows the typical schematic illustration of underpotential deposition of lead atoms on the surface of gold electrode [11].

Pseudocapacitive redox reactions occurs when electrolyte ions are electrochemically adsorbed onto the surface/near surface of a electrode material with the occurrence of simultaneous faradaic charge-transfer as shown in Fig. 1.6, the redox reaction of protons on the surface of RuO_2 [12]. There is another type of pseudocapacitance occurs on the layered electroactive materials when electrolyte ions intercalate into the tunnels/layers of host redox active electrode material followed by faradaic charge-transfer reaction without any phase change of the crystal structure. For example, Fig. 1.7, shown the intercalation of lithium ions into the Nb_2O_5 layered crystal structure [13].

1.2.3 Hybrid supercapacitors

There is a special type of capacitors called ‘hybrid capacitors’ which has been made of combination of both EDLC and pseudocapacitor materials [14]. The aim of the development of hybrid capacitors is to utilize both Faradaic and non-Faradaic energy storage process there by achieve higher energy density and power density with good cycling stability. There is a special category of hybrid capacitors called asymmetric hybrid supercapacitors [15], in which faradaic reaction takes place on one of the electrodes and EDLC charge (non-Faradaic) charge storage occurs on the opposite electrode in a single device. The hybrid supercapacitors are further classified into two different categories such as (i) battery-like hybrids and (ii) composite hybrids. In general, hybrid supercapacitors were developed based on the combination of various electrode materials to improve the cell performance. The well-known non-Faradaic EDLC type

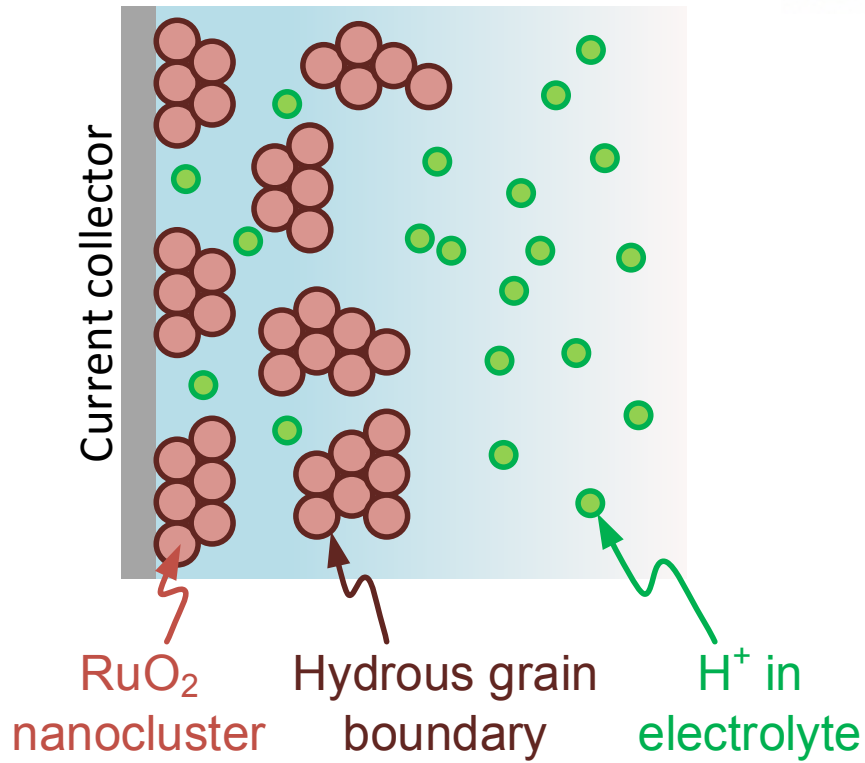


Fig. 1.6 Redox pseudocapacitance of protons on the RuO₂ electrode surface.

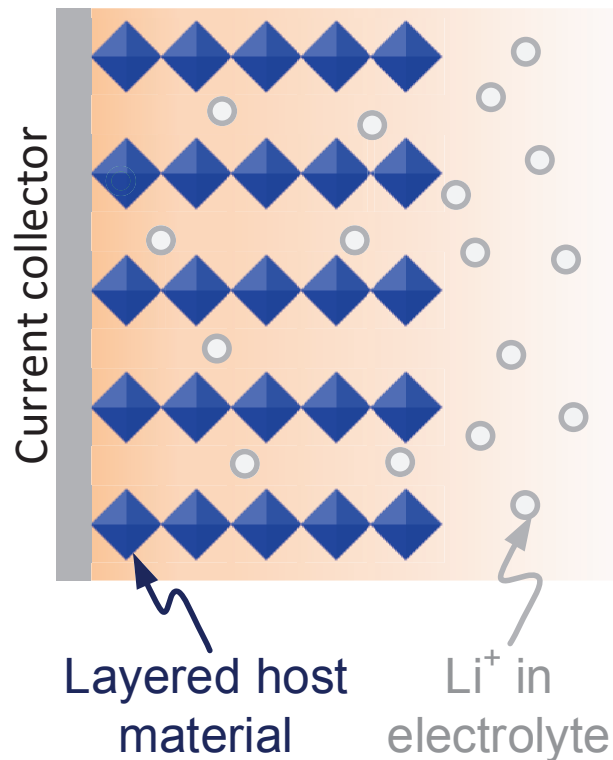


Fig. 1.7 Intercalation pseudocapacitance of lithium ions into the Nb₂O₅ layered host electrode.

charge storage materials are activated carbon, carbon nanotubes, and graphene-based active materials with high surface area [16]. The typical pseudocapacitors are based on the electrochemical redox reactions, the

examples of pseudocapacitive materials including transition metal oxides (TMOs) such as Fe_3O_4 , MnO_2 , RuO_2 , and NiO [10] and electrically conducting redox active polymers such as polypyrroles, polyanilines and polythiophenes [17].

1.3 Primary Objectives of Present Work

The major goal of the present thesis is to design, synthesis, physico-chemical characterization and the evaluation of electrochemical performance of hybrid nanostructured materials based on transition metal oxide and transition metal dichalcogenides with a carbon matrix to achieve high-energy density, high-power density, and long cycle life supercapacitors. Following are the primary objectives of the present study:

- (1) Investigation of the effective charge storage performance of V_2O_5 materials by grafting with highly conducting reduced graphene oxide nanosheets to form graphene decorated vanadium pentoxide nanobelts (GVNBs).
- (2) Investigation of the essential electrochemical properties of transition metal dichalcogenides (TMDCs) by preparing the layered two-dimensional materials such as molybdenum disulfide (MoS_2), molybdenum diselenide (MoSe_2) nanostructures with controllable morphology and high surface area materials as supercapacitor electrodes.
- (3) Design of nanostructured composite materials consist of TMDCs and reduced graphene oxides for high-performance supercapacitor applications.
- (4) Design and synthesis of amorphous phase TMDCs having high defect sites there by enhance the effective ion intercalation and charge storage. To overcome the poor conductivity issue of amorphous phase TMDCs, reduction of internal resistance, and also enhance the fast ion/electron transportation, a novel approach of direct binder-free growth of TMDCs on highly conducting 3D carbon fiber paper network has been designed for high performance and long-cycle life symmetric capacitors.

In order to achieve the above mentioned objectives, a series of methods were used for the synthesis of electroactive materials which include hydrothermal, freeze drying, and modified Hummer's methods. The physico-chemical properties were well characterized using XRD, Raman, FE-SEM, HR-TEM, BET, and XPS techniques. The electrochemical performance were evaluated using cyclic voltammetry, galvanostatic charge/discharge and electrochemical impedance spectroscopy methods. The outcome of this thesis may provide a facile and effective approach to fabricate the layered two-dimensional materials (TMDCs) with carbon matrix as the potential electrode materials for high-performance supercapacitors.

References

- [1] Wang, H., Dai, H., Strongly coupled inorganic-nano-carbon hybrid materials for energy storage, *Chem. Soc. Rev.* 2013, 42, 3088–3113. doi:[10.1039/C2CS35307E](https://doi.org/10.1039/C2CS35307E).

- [2] Lee, M., Balasingam, S.K., Jeong, H.Y., Hong, W.G., Lee, H.B.R., Kim, B.H., Jun, Y.A., One-step hydrothermal synthesis of graphene decorated V_2O_5 nanobelts for enhanced electrochemical energy storage, *Scientific Reports* 2015, 5, 8151. doi:[10.1038/srep08151](https://doi.org/10.1038/srep08151).
- [3] Goodenough, J.B., Park, K.S., The li-ion rechargeable battery: A perspective, *Journal of the American Chemical Society* 2013, 135 (4), 1167–1176. doi:[10.1021/ja3091438](https://doi.org/10.1021/ja3091438). URL: <http://dx.doi.org/10.1021/ja3091438>. PMID: 23294028.
- [4] Simon, P., Gogotsi, Y., Dunn, B., Where do batteries end and supercapacitors begin?, *Science* 2014, 343 (6176), 1210–1211. doi:[10.1126/science.1249625](https://doi.org/10.1126/science.1249625). URL: <http://www.sciencemag.org/content/343/6176/1210.short>.
- [5] Balasingam, S.K., Lee, J.S., Jun, Y., Few-layered $MoSe_2$ nanosheets as an advanced electrode material for supercapacitors, *Dalton Transactions* 2015, 44 (35), 15491–15498. doi:[10.1039/C5DT01985K](https://doi.org/10.1039/C5DT01985K).
- [6] Ellis, B.L., Knauth, P., Djenizian, T., Three-dimensional self-supported metal oxides for advanced energy storage, *Advanced Materials* 2014, 26 (21), 3368–3397. doi:[10.1002/adma.201306126](https://doi.org/10.1002/adma.201306126).
- [7] Simon, P., Gogotsi, Y., Materials for electrochemical capacitors, *Nature materials* 2008, (11). doi:[10.1038/nmat2297](https://doi.org/10.1038/nmat2297).
- [8] Yu, G., Xie, X., Pan, L., Bao, Z., Cui, Y., Hybrid nanostructured materials for high-performance electrochemical capacitors, *Nano Energy* 2013, 2 (2), 213–234. doi:[10.1016/j.nanoen.2012.10.006](https://doi.org/10.1016/j.nanoen.2012.10.006). Cited By 216.
- [9] Conway, B.E., *Electrochemical supercapacitors: scientific fundamentals and technological applications*, Springer Science & Business Media, 2013.
- [10] Augustyn, V., Simon, P., Dunn, B., Pseudocapacitive oxide materials for high-rate electrochemical energy storage, *Energy and Environmental Science* 2014, 7 (5), 1597–1614. doi:[10.1039/c3ee44164d](https://doi.org/10.1039/c3ee44164d). Cited By 143.
- [11] Enrique Herrero, ., Buller, L.J., Abruna, H.D., Underpotential deposition at single crystal surfaces of au, pt, ag and other materials, *Chemical Reviews* 2001, 101 (7), 1897–1930. doi:[10.1021/cr9600363](https://doi.org/10.1021/cr9600363). PMID: 11710235.
- [12] Sugimoto, W., Kizaki, T., Yokoshima, K., Murakami, Y., Takasu, Y., Evaluation of the pseudocapacitance in RuO_2 with a RuO_2/gc thin film electrode, *Electrochimica Acta* 2004, 49 (2), 313 – 320. doi:<http://dx.doi.org/10.1016/j.electacta.2003.08.013>.
- [13] Kong, L., Zhang, C., Zhang, S., Wang, J., Cai, R., Lv, C., Qiao, W., Ling, L., Long, D., High-power and high-energy asymmetric supercapacitors based on Li^+ -intercalation into a T– $Nb_2O_5/graphene$ pseudocapacitive electrode, *J. Mater. Chem. A* 2014, 2, 17962–17970. doi:[10.1039/C4TA03604B](https://doi.org/10.1039/C4TA03604B).
- [14] Sahu, V., Goel, S., Sharma, R.K., Singh, G., Zinc oxide nanoring embedded lacey graphene nanoribbons in symmetric/asymmetric electrochemical capacitive energy storage, *Nanoscale* 2015. doi:[10.1039/C5NR06083D](https://doi.org/10.1039/C5NR06083D).

- [15] Yan, J., Fan, Z., Sun, W., Ning, G., Wei, T., Zhang, Q., Zhang, R., Zhi, L., Wei, F., Advanced asymmetric supercapacitors based on Ni(OH)₂/graphene and porous graphene electrodes with high energy density, *Advanced Functional Materials* 2012, 22 (12), 2632–2641. doi:[10.1002/adfm.201102839](https://doi.org/10.1002/adfm.201102839).
- [16] Huang, J., Sumpter, B., Meunier, V., Theoretical model for nanoporous carbon supercapacitors, *Angewandte Chemie International Edition* 2008, 47 (3), 520–524. doi:[10.1002/anie.200703864](https://doi.org/10.1002/anie.200703864).
- [17] Shown, I., Ganguly, A., Chen, L.C., Chen, K.H., Conducting polymer-based flexible supercapacitor, *Energy Science & Engineering* 2015, 3 (1), 2–26. doi:[10.1002/ese3.50](https://doi.org/10.1002/ese3.50).

CHAPTER 2

Material Synthesis, Physico-chemical and Electrochemical Characterizations

2.1 Materials Synthesis

2.1.1 Hydrothermal synthesis of nanomaterials

The nanomaterials can be synthesized by several ways, this dissertation mainly focused on the hydrothermal synthesis method due to the following merits: (i) facile low temperature process, (ii) variety of nanostructures can be obtained by tuning the pH, temperature, precursor concentration, precursor volume etc., (iii) green and environmental friendly technique, (iv) the resultant products are mostly high purity defect free materials and (v) ease of scaling, simple metal salt based precursors, no toxic solvents and additives.

The hydrothermal process is not such an innovative method. Geological researchers got inspired by the natural formation of rocks and minerals under high pressure hot water circulation inside the earth crust. This principle has been adopted by chemists and the varieties of inorganic materials were synthesized from 18th century. The hydrothermal synthesis is a one of the types of *solvo*thermal process, in which the chemical reaction takes place in a solvent medium at the temperature above the boiling point of solvent at a pressure of above 1 bar. If the solvent used is a water then the process is termed as *hydro*thermal. By definition, hydrothermal synthesis refers to the heterogeneous reaction in aqueous media at the temperature of above 100 °C and at the pressure of above 1 bar. A batch reactor is used for conventional hydrothermal synthesis process. Figure 2.1 shows schematic representation of the laboratory scale reactor (100 ml capacity) used in this research. The water soluble precursors were dissolved and the precursor solution was transferred into the Teflon-lined stainless steel autoclave. The autoclave was sealed tightly, transferred inside the electric oven and then heated to the desired temperature for particular duration. Depending on the degree of filling inside the autoclave the pressure up to several hundred bar can be created inside the chamber even at a low temperature heating process.

2.1.2 Synthesis of graphene oxide by modified Hummer's method

GO was prepared from natural graphite powder according to the modified Hummer's method [1]. 12 g of graphite powder (SP-1, Bay carbon), 10 g of $K_2S_2O_8$ (Sigma Aldrich, $\geq 99.0\%$), and 10 g of P_2O_5 (Sigma Aldrich, 99.99%) were added to 50 mL of concentrated H_2SO_4 solution and heated to 80 °C. The

resultant mixture was kept overnight with 2 L of DI water. The mixture was then filtered and washed with DI water several times. The suspension was dried in vacuum under ambient conditions. This pretreated flake-like graphite was mixed with 460 mL of H_2SO_4 at 0°C , and then 60 g of KMnO_4 (Sigma Aldrich, $\geq 99.0\%$) was added slowly for further oxidation. The mixture was stirred for 2 h at 35°C and, subsequently, 920 mL of DI water was added. Shortly afterwards, 2.8 L of DI water and 50 mL of 30% H_2O_2 (SAMCHUN pure chemical) were added into the concentrated H_2SO_4 solution. The GO suspension was centrifuged and washed with 5 L of 10% HCl (SAMCHUN pure chemical) solution and, repeatedly, with 5 L of DI water, followed by filtering of the graphite-oxide solution through dialysis (dialysis membrane: Spectrum Laboratories, MWCO-12-14,000) for 2 weeks. Finally, GO sheets were prepared through drying the resulting suspension at 50°C for 3 days.

2.2 Physico-chemical Characterization

The synthesized nanostructured materials were analyzed using a few characterization techniques in order to examine the crystal phase, surface morphology, microstructure, particle size, elemental composition and surface area. The detailed experimental conditions are given below.

2.2.1 X-ray diffraction

X-ray diffraction (XRD) is a non-destructive analytical method to determine the crystal phase, purity, size and structure. The as-prepared samples were measured by using Bruker (D8 Advance) with $\text{Cu K}\alpha$ radiation, $\lambda = 1.54178 \text{ \AA}$ in the range of $10\text{-}80^\circ$ with a step of 0.02° .

2.2.2 Raman spectroscopy

The Raman analysis is sensitive towards the crystallization, structural disorders and defects in nanostructured materials. Therefore, Raman spectroscopic analysis have been performed for the as-synthesized nanomaterials. Further, it is also one of the ideal too to investigate the bonding nature of various carbon materials such as defect free-graphene, graphene oxide and reduced graphene oxide (rGO) and its extension of reduction. Raman spectra of the samples were studied using a Raman spectroscopy (Alpha 300S,

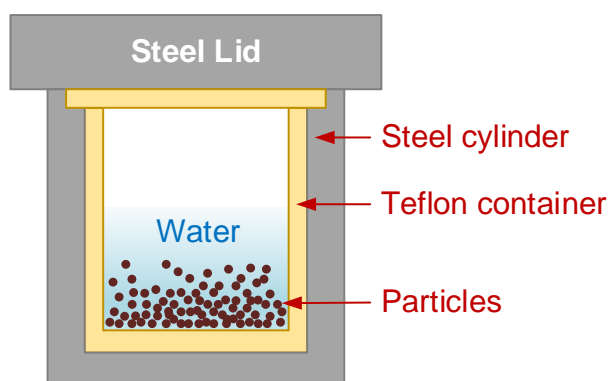


Fig. 2.1 Schematic illustration of laboratory scale autoclave.

WITec) using a He-Ne laser with a laser excitation wavelength of 532 nm, after calibrating the Raman shift with a standard silicon reference at 521 cm^{-1} . The Raman system was operated at various range of laser power from 1mW to 10 mW, depending on the properties of material.

2.2.3 Field-emission scanning electron microscopy

The surface morphology, and particle size of the prepared materials were examined using the field emission scanning electron microscope (FE-SEM (Nano230, FEI co.) with different acceleration voltage and filament currents based on the nature of samples. Before measurement, the as-prepared samples were fixed onto a double-face conducted tape mounted on a metal stud and coated with a very thin layer of platinum/gold using the sputter coater.

2.2.4 High-resolution transmission electron microscopy

The particle size, microstructure, and crystalline phase of the nanomaterials were investigated using the high-resolution transmission electron microscopy (HR-TEM, JEOL– 2100F, FEI-Titan3 G2 60-300, FEI-Talos F200X) with various range of accelerating voltage. For TEM observations, the nanomaterial samples were prepared by dispersing the NPs in ethanol followed by ultrasonic vibration for 5 min, and then dropped a drop of the dispersion onto a copper grid, which must be dried before loading in to the instrument. BFTEM, electron diffraction pattern, and EELS were performed with an image-side aberration-corrected TEM (Titan3 G2 60-300, FEI) which was operated at 80 kV. High-angle annular dark field (HAADF) scanning transmission electron microscopy (STEM) was carried out using a probe-side aberration-corrected TEM (JEOL-2100F, FEI-Talos F200X) operated at 200 kV. To investigate the microstructure of thin-layer coated CFP material, a slice of TEM sample was prepared using a focused ion beam equipped scanning electron microscope (FEI, Quanta 3D), after depositing a thin layer of epoxy/Pt on the surface of samples.

2.2.5 X-ray photoelectron spectroscopy

The chemical composition and the oxidation state of elements present in the outermost part of samples were investigated using X-ray photoelectron spectroscopy (XPS, Thermo Fisher, UK). Here, a monochromatic X-ray beam source of Al $K\alpha$ radiation at 1486.6 eV (Aluminum anode) and 14 kV was used to scan upon the sample surface. A high flux X-ray source with Aluminum anode was used for X-ray generation, and a quartz crystal monochromator was used to focus and scan the X-ray beam on the sample.

2.3 Electrode Fabrication and Symmetric Cell Assembly

2.3.1 Electrode fabrication

The working-electrodes of supercapacitors were prepared by various method depending on the nature of the electroactive materials. In a typical electrode fabrication process, the as-synthesized samples, conducting acetylene black and poly(tetrafluoroethylene) (PTFE) or polyvinylidene difluoride (PVDF)

were mixed in the mass ratio of 80:10:10 and ground in a mortar using an N-methyl pyrrolidone (NMP) or ethanol solvent. The resulting homogeneous paste was then coated on a stainless steel or nickel-foam substrate (mass loading of approximately ~ 3 to 5 mg/cm^2) using the spatula and then dried at $120 \text{ }^\circ\text{C}$ for 12 h in a vacuum oven. The mass loading of the electrode active material was measured using balance before and after loading of electroactive materials on the substrate. The direct deposition of transition metal dichalcogenides (TMDCs) onto the carbon fiber paper (CFP) electrodes are used as such as a binder-free electrodes.

2.3.2 Symmetric cell assembly

The working electrodes were fabricated as mentioned in section 2.3.1. An exactly 1 cm^2 ($1 \text{ cm} \times 1 \text{ cm}$) area of electroactive materials-coated SS substrate was used as a single electrode. A mass loading of each electrode was controlled in the range of $3\text{-}5 \text{ mg cm}^{-2}$. Also, an exactly 1 cm^2 ($1 \text{ cm} \times 1 \text{ cm}$) area of binder-free TMDCs coated CFP electrode was used as a single electrode with the mass loading of around $30 \mu \text{ cm}^{-2}$. Two electrodes were sandwiched together with Whatman filter paper as a separator. The assembled electrodes were placed in a test cell rig, and a few drops of 0.5 M sulfuric acid were added as the electrolyte. The test cell was sealed with an O-ring and then left for a few minutes to ensure the uniform soaking of the electrodes into the electrolyte solution before the electrochemical measurements.

2.4 Electrochemical Characterization

2.4.1 Cyclic voltammetry

CV is generally considered to be an appropriate tool investigate the difference between the non-Faradic and Faradic processes in an electrochemical reaction. In CV measurement, the voltage is swept between a lower limit to an upper limit at a fixed rate. The voltage scan rate is calculated from the slope of the line. The current evolution was measured as a function of the voltage. The characteristics of the cyclic voltammogram recorded depend on a rate of the electron transfer reaction, chemical reactivity of the active species and the voltage scan rate. The cyclic voltammetry (CV) data of the electrodes were obtained for various scan rates such as 1, 2, 5, 10, 25, 50, 75, 100, 125, 200 and 500 mV s^{-1} .

2.4.2 Galvanostatic charge/discharge

The galvanostatic charge/discharge (GCD) measurements are one of the most important and direct approach to evaluate the real-time application of electrode materials for supercapacitors. A repetitive loop of charging and discharging is called a cycle. Most often, charge and discharge process are conducted at a constant current (Galvanostatic mode) until a set potential is reached. The galvanostatic charge-discharge (GCD) curves were recorded for various current densities.

2.4.3 Electrochemical impedance spectroscopy

Electrochemical Impedance Spectroscopy (EIS) is a powerful tool to understand the capacitive behavior and resistance associated with the as-prepared electrode surface. The advantage of EIS is that it is

generally a non-destructive technique which will not affect the electrode/cell system. This enables the possibility for further electrochemical measurements and post-mortem investigations. EIS is the most common method to measure the equivalent series resistance (ESR) of supercapacitors. It also allows creating models to describe the underlying reaction mechanisms. With these models, ideal capacitive behavior and the extent of deviation from ideality (non-ideal behavior) can also be investigated. Generally, a sinusoidal AC excitation signal is applied into the investigated system during an EIS experiment and the AC response is measured. Frequency sweeping in a wide range from high-to low-frequency region enables the reaction steps with different rate constants, such as mass transport, charge transfer, and chemical reaction, to be separated.

In the present research, the EIS experiments for the prepared electrodes and the assembled symmetric capacitors samples were measured at a frequency range of 0.1 Hz to 100 kHz. The EIS data were analyzed using the Nyquist plots by plotting the imaginary component ($-Z''$) of the impedance against the real component (Z'), which shows the frequency response of the electrode/electrolyte system.

2.5 Calculation of Electrode and Symmetric Cell Performance

The electrochemical performance of the electrode materials was characterized using three-electrode configuration and the device performance of the symmetric cells was measured using two-electrode configuration. The electrochemical parameters, such as specific capacitance (C), energy (E), and power density (P) are important parameters for the investigation of the capacitive behavior of electrochemical cells.

2.5.1 A single electrode performance using three-electrode setup

2.5.1.1 Gravimetric specific capacitance

The specific capacitance of electrode (C_s , $F g^{-1}$) can be calculated based on the CV measurements using the following equation [2]:

$$C_s = \frac{\int I(V) dv}{vm\Delta V} \quad (F g^{-1}) \quad (2.1)$$

where, m is the mass of the electroactive material (g), v is the scan rate ($V s^{-1}$), ΔV is the potential window (V), and $\int I(V) dv$ is the integral area of the CV loop.

From the GCD curves, the specific capacitance of electrode (C_s , $F g^{-1}$) can also be computed as [2]:

$$C_s = \frac{I\Delta t}{m\Delta V} \quad (F g^{-1}) \quad (2.2)$$

where, I is the discharge current (A), Δt is the discharge time (s), m is the mass of the electroactive material (g), and ΔV is the potential window (V)

2.5.2 Symmetric cell and its single electrode performance using two-electrode setup

2.5.2.1 Gravimetric specific capacitance

From the CV measurements, the specific capacitance of the symmetric cell (C_m , F g^{-1}) was computed according to the following equation [3]:

$$C_m = \frac{\int I(V) dv}{vm\Delta V} \quad (\text{F g}^{-1}) \quad (2.3)$$

where, C_m is the gravimetric specific capacitance of the device (F g^{-1}), m is the total mass of the electroactive material in the both positive and negative electrodes (g), v is the scan rate (V s^{-1}), ΔV is the potential window (V), and $\int I(V) dv$ is the integral area of the CV loop.

From the GCD curves, the specific capacitance of the symmetric cells (C_m) was determined as [3]:

$$C_m = \frac{I\Delta t}{m\Delta V} \quad (\text{F g}^{-1}) \quad (2.4)$$

where, C_m is the gravimetric specific capacitance of the device (F g^{-1}), I is the discharge current (A), m is the total mass of the electroactive material in the both positive and negative electrodes (g), ΔV is the potential window (V), and Δt is the discharge time (s).

The specific capacitance of the single electrode (C_s , F g^{-1}) can be determined as follows [3]:

$$C_s = 4 \times C_m \quad (\text{F g}^{-1}) \quad (2.5)$$

where, C_s is the gravimetric specific capacitance of a single electrode (F g^{-1}), C_m is the gravimetric specific capacitance of the device (F g^{-1}), which can be obtained either from CV or GCD measurements given by Eqs. (2.3) and (2.4).

2.5.2.2 Areal specific capacitance

From the CV measurements, the device capacitance of the symmetric cell (C_{cell} , F) was determined according to the following equation [4]:

$$C_{cell} = \frac{\int I(V) dv}{v\Delta V} \quad (\text{F}) \quad (2.6)$$

where, C_{cell} is the measured device capacitance (F), v is the scan rate (V s^{-1}), ΔV is the potential window (V), and $\int I(V) dv$ is the integral area of the CV loop.

From the GCD curves, the device capacitance of the symmetric cell (C_{cell} , F) was determined as [5]:

$$C_{cell} = \frac{I\Delta t}{\Delta V} \quad (\text{F}) \quad (2.7)$$

where, C_{cell} is the measured device capacitance (F), I is the discharge current (A), ΔV is the potential window (V), and Δt is the discharge time (s).

The areal specific capacitance of the device (C_m) and the areal specific capacitance of a electrode (C_s) was calculated as follows [4, 5]:

$$C_m = \frac{C_{cell}}{A} \quad (\text{F cm}^{-2}) \quad (2.8)$$

$$C_e = 2 \times C_{cell} \quad (\text{F}) \quad (2.9)$$

$$C_s = \frac{C_e}{A} \quad (\text{F cm}^{-2}) \quad (2.10)$$

where, C_{cell} is the measured device capacitance (F), which can be obtained either from CV or GCD curves using Eqs. (2.6) and (2.7), C_e is the single electrode capacitance (F), A is the geometric area of an electrode (cm^2), C_m areal specific capacitance of the device (F cm^{-2}), and C_s is the areal specific capacitance of a single electrode (F cm^{-2}).

2.5.2.3 Energy and Power density

$$E = \frac{1000 \times C_m V^2}{(2 \times 3600)} \quad (\text{Wh kg}^{-1}) \quad (2.11)$$

$$P = \frac{E \times 3600}{\Delta t} \quad (\text{W kg}^{-1}) \quad (2.12)$$

where, E is the energy density (Wh kg^{-1}) C_m is the gravimetric specific capacitance of the device (F g^{-1}) calculated using Eq. (2.4), V is the potential window (V), P is the power density (W kg^{-1}), and Δt is the discharge time (s).

References

- [1] Tung, V.C., Allen, M.J., Yang, Y., Kaner, R.B., High-throughput solution processing of large-scale graphene, *Nature Nanotechnology* 2009, 4 (1), 25–29. doi:[10.1038/nnano.2008.329](https://doi.org/10.1038/nnano.2008.329).
- [2] Lee, M., Balasingam, S.K., Jeong, H.Y., Hong, W.G., Lee, H.B.R., Kim, B.H., Jun, Y., One-step hydrothermal synthesis of graphene decorated V_2O_5 nanobelts for enhanced electrochemical energy storage, *Scientific Reports* 2015, 5, 8151. doi:[10.1038/srep08151](https://doi.org/10.1038/srep08151).
- [3] Balasingam, S.K., Lee, J.S., Jun, Y., Few-layered MoSe_2 nanosheets as an advanced electrode material for supercapacitors, *Dalton Transactions* 2015, 44 (35), 15491–15498. doi:[10.1039/C5DT01985K](https://doi.org/10.1039/C5DT01985K).
- [4] Wu, Z.S., Parvez, K., Feng, X., Müllen, K., Graphene-based in-plane micro-supercapacitors with high power and energy densities, *Nature communications* 2013, 4, 2487. doi:[10.1038/ncomms3487](https://doi.org/10.1038/ncomms3487).
- [5] Cao, L., Yang, S., Gao, W., Liu, Z., Gong, Y., Ma, L., Shi, G., Lei, S., Zhang, Y., Zhang, S., Vajtai, R., Ajayan, P.M., Direct laser-patterned micro-supercapacitors from paintable MoS_2 films, *Small* 2013, 9 (17), 2905–2910. doi:[10.1002/sml.201203164](https://doi.org/10.1002/sml.201203164).

Part I

Nanostructured Transition Metal Oxide/Carbon Electrodes

CHAPTER 3

Graphene Decorated V_2O_5 Nanobelts*

**Reproduced in part from S. K. Balasingam et al., Scientific Reports 2015, 5, 8151.*

Copyright 2015 Nature Publishing Group (NPG).

3.1 Introduction

In general, carbon materials are best known for their double layer capacitance behavior, which provides the high power density to the capacitors. To enhance the energy density of supercapacitors, suitable pseudocapacitance materials have been combined with the carbon-based materials. Various carbon materials, such as activated carbon, graphite, carbon nanotubes, and graphene have been used. Among these, graphene, a new class of carbon material has attracted great interest due to its high surface area and excellent electrical, mechanical, chemical, and thermal properties [1, 2]. In case of pseudocapacitance materials, conducting polymers and transition-metal oxides are primarily used in order to enhance the energy density of supercapacitors [3]. Among the various transition-metal oxides, V_2O_5 (VO) has widely been investigated as a high-potential candidate material because of the following merits: low cost, abundant resources, layered structure, high energy density, and wide potential window arising from its multivalent oxidation states [4, 5]. Although VO-based materials have achieved remarkable benchmark properties in various fields, such as in lithium-ion batteries, field-effect transistors, gas sensors, and supercapacitors, their poor electronic conductivity and bulk material properties prevent enhanced device performance [6–10].

In this regard, a large number of VO nanostructures, such as nanowires, nanotubes, and nanobelts have recently been fabricated in order to obtain a high surface area [11, 12]. Moreover, the combination of commercially available carbon allotropes and their derivatives with metal-oxide materials enhances the electronic conductivity of the composites and also prevents agglomeration of metal-oxide nanoparticles during cycling tests [13–15]. Enhanced electrochemical energy storage using nanostructured VO/graphene composites have been reported recently [16–19]. However, the preparation of nanostructures of VO/graphene composites commonly followed two-step processes in which reduced graphene oxide (rGO) was usually prepared either by chemical reduction or by a thermal treatment in order to obtain higher conductivity [20–23]. Further, very recently, our group synthesized graphene decorated nanostructured VO by simple mixing of VO particles and graphene oxide (GO) in DI water. However, this process takes a long time (approximately eight weeks) to fabricate nanostructure [24]. In this paper, we have reported a facile low-temperature hydrothermal process for the rapid synthesis of graphene-decorated

VO nanobelts (GVNBs) without any harmful oxidizing or reducing chemical agents and surfactants. During the synthesis of GVNBs, VO particles were converted into uniformly distributed nanobelts with simultaneous reduction of GO into rGO, even at low temperature. GO played a vital role in this study. Initially, GO might act as a mild oxidizing agent to synthesize V_2O_5 nanobelts in DI water under hydrothermal conditions, in which GO is converted into rGO (generally, oxidizing agents reduce themselves while chemical reaction occurs). Once the GVNBs are synthesized, the highly conducting reduced GO provides double layer capacitance (in turn high power density) to the supercapacitors. Overall, the nanostructured VO involves in the faradaic reaction (pseudocapacitance), which provides high energy density and the highly conducting rGO having large surface area implicates double layer capacitance, which delivers high power density to the supercapacitors. The as-prepared GVNBs having vanadium rich composition showed the enhanced specific capacitance of 288 F g^{-1} due to the combination of pseudocapacitance and double-layer capacitance behaviour.

3.2 Experimental

3.2.1 Preparation of graphene oxide and reduced graphene oxide

GO was prepared from natural graphite powder according to the modified Hummer's method [25]. 12 g of graphite powder (SP-1, Bay carbon), 10 g of $K_2S_2O_8$ (Sigma Aldrich, $\geq 99.0\%$), and 10 g of P_2O_5 (Sigma Aldrich, 99.99%) were added to 50 mL of concentrated H_2SO_4 solution and heated to 80°C . The resultant mixture was kept overnight with 2 L of DI water. The mixture was then filtered and washed with DI water several times. The suspension was dried in vacuum under ambient conditions. This pretreated flake-like graphite was mixed with 460 mL of H_2SO_4 at 0°C , and then 60 g of $KMnO_4$ (Sigma Aldrich, $\geq 99.0\%$) was added slowly for further oxidation. The mixture was stirred for 2 h at 35°C and, subsequently, 920 mL of DI water was added. Shortly afterwards, 2.8 L of DI water and 50 mL of 30% H_2O_2 (SAMCHUN pure chemical) were added into the concentrated H_2SO_4 solution. The GO suspension was centrifuged and washed with 5 L of 10% HCl (SAMCHUN pure chemical) solution and, repeatedly, with 5 L of DI water, followed by filtering of the graphite-oxide solution through dialysis (dialysis membrane: Spectrum Laboratories, MWCO-12-14,000) for 2 weeks. Finally, GO sheets were prepared through drying the resulting suspension at 50°C for 3 days. In this work, two kinds of rGO were separately prepared by different methods. The first type of rGO was prepared by pyrolysis of GO in a quartz tube furnace at 1100°C for 2 h under Ar flow for comparison purpose with GO used for the synthesis of GVNBs [26]. The other type of rGO was obtained via the hydrothermal route [27] and annealed in a vacuum furnace to investigate the characteristics of supercapacitors under the same conditions like those of GVNBs.

3.2.2 Synthesis of graphene decorated V_2O_5 nanobelt composites

Different ratios (3:1, 1:1, 1:3) of pristine V_2O_5 (VO) particles (Aldrich) and of as-synthesized GO were dispersed in 30 mL of DI water and then stirred vigorously for 2 h at room temperature. The obtained yellow/brownish slurry was transferred into a 50 mL Teflon-lined stainless-steel autoclave and maintained at 120°C for 24 h in a muffle furnace. Then, the autoclave was cooled naturally to room temperature

inside the muffle furnace. The resulting material was freeze-dried for 72 h to obtain GVNBS with high surface area. The final product was transferred into a vacuum furnace and annealed at 400 °C for 2 h under Ar gas in order to improve the crystallinity of the GVNBS.

3.2.3 Materials characterization

The crystalline structure of the as-prepared samples was characterized using XRD (Bruker D8 Advance with Cu K α radiation, $\lambda = 1.54178 \text{ \AA}$). The morphologies of the samples were observed by FE-SEM (Nano230, FEI co.). XPS (Thermo Fisher, UK) measurements were performed with monochromatic Al K α radiation as X-ray source for the investigation of the surface states. To gain further insight into the structure of the products, they were additionally investigated by Raman spectroscopy (Alpha 300S, WITec) using a He-Ne laser with 532 nm in wavelength. The thickness of a single GNVN on SiO₂ substrate was measured using AFM (Multimode V, Veeco). BF-TEM, electron diffraction pattern, and EELS were performed with an image-side aberration-corrected TEM (Titan3 G2 60-300, FEI) which was operated at 80 kV. High-angle annular dark field (HAADF) scanning transmission electron microscopy (STEM) was carried out using a probe-side aberration-corrected TEM (JEOL 2100F, JEOL) operated at 200 kV.

3.2.4 Electrochemical characterization

Electrochemical experiments were carried out in the typical three-electrode-cell setup using a potentiostat/galvanostat (Biologic/VSP) at room temperature. The working-electrode paste was prepared by mixing the corresponding electroactive materials (graphene, V₂O₅, V₁G₃, V₁G₁, and V₃G₁), conducting acetylene black, and a polymeric binder (polyvinylidene difluoride) in the mass ratio of 80:10:10 and ground in a mortar using an N-methyl pyrrolidone (NMP) solvent. The paste was then coated on nickel-foam substrate (mass loading $\sim 3.5 \text{ mg/cm}^2$) using the spatula and then dried at 120 °C for 12 h in a vacuum oven. A large surface area platinum mesh was used as counter electrode, Ag/AgCl (std. KCl) was used as reference electrode, and 1 M Na₂SO₄ solution was used as electrolyte. Cyclic voltammograms (CV) were obtained at various scan rates (5, 10, 25, 50, 75, 100, 125 mV s⁻¹) in the potential window of 0 to 0.8 V (Vs Ag/AgCl [std. KCl]). Electrochemical impedance spectroscopy (EIS) measurements were carried out over the frequency range of 0.1 Hz to 100 kHz with the AC amplitude of 10 mV. Galvanostatic charge/discharge curves were recorded at different current densities (0.25, 0.5, 0.75, 1 A g⁻¹) in the potential window of 0 to 0.8 V (Vs Ag/AgCl [std. KCl]).

3.3 Results and Discussion

3.3.1 Physico-chemical analysis

Fig. 3.1 illustrates the role of different precursors on the synthesis of GVNBS by the low-temperature hydrothermal process. The mixing of VO suspension and rGO precursors did not induce the formation of nanostructure (Scheme a). However, the mixing of GO precursors with the VO dispersion under the same experimental conditions (scheme c) leads to the formation of GVNBS. In order to confirm the role of GO

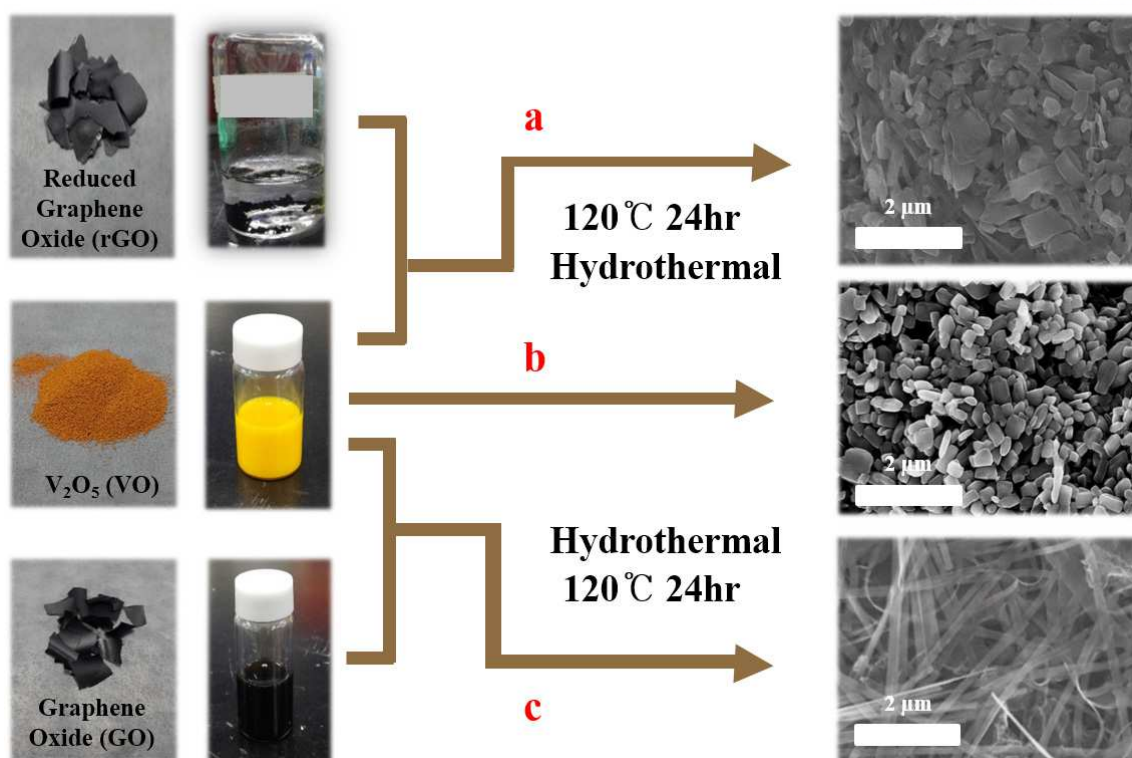


Fig. 3.1 Schemes (a) and (b) represent the absence of nanobelts formation in case of rGO addition and without carbon material, respectively, via low-temperature hydrothermal synthesis. Scheme (c) represents the formation of GNVBs by mixing of GO into VO dispersion under the same hydrothermal conditions.

on the nanostructure formation, only VO dispersion was subjected to the low-temperature hydrothermal process at identical experimental conditions (scheme b), but no noticeable morphological change could be observed.

Fig. 3.2 presents the field-emission scanning electron microscopy (FE-SEM) images of pristine VO, VO after the hydrothermal treatment, the composite of VO with rGO, and GNVBs synthesized via the low-temperature hydrothermal basis of the FE-SEM images, the transformation into nanobelts have been observed only in case GO was added into the VO suspension, whereas the absence of GO or the use of rGO at the same conditions did not induce the formation of GNVBs.

The structure of pristine VO, GNVBs, and rGO have been investigated by X-ray diffraction (XRD), as shown in Fig. 3.3. The peaks of pristine VO well matched the corresponding standard pattern (JCPDS Card No. 89-0612). The XRD patterns of different composites (V_3G_1 , V_1G_1 , and V_1G_3) of GNVBs contain peaks of GO, rGO, and VO nanobelts (VNBs). The peaks at 6.32° , 25.9° , 28.5° , 32.7° , and 41.7° correspond to the (001), (110), (111), (004), and (005) planes of VNBs, respectively [28, 29]. The interlayer distance of GNVBs at the (001) reflection is calculated to be 1.40 nm, which is larger than the interlayer distance of pure V_2O_5 nanowires (1.15 nm) reported previously for the same (001) planes [30, 31]. The peaks at 17.2° , 24.6° are assigned to partially reduced GO and rGO respectively [32]. Usually, GO is reduced to rGO via a high-temperature heat treatment or by strong reducing agents. In this experiment, partially reduced GO (prGO) was synthesized using the hydrothermal method under identical conditions for all samples to enable a quantitative comparison of the performance [27, 33, 34]. GO shows

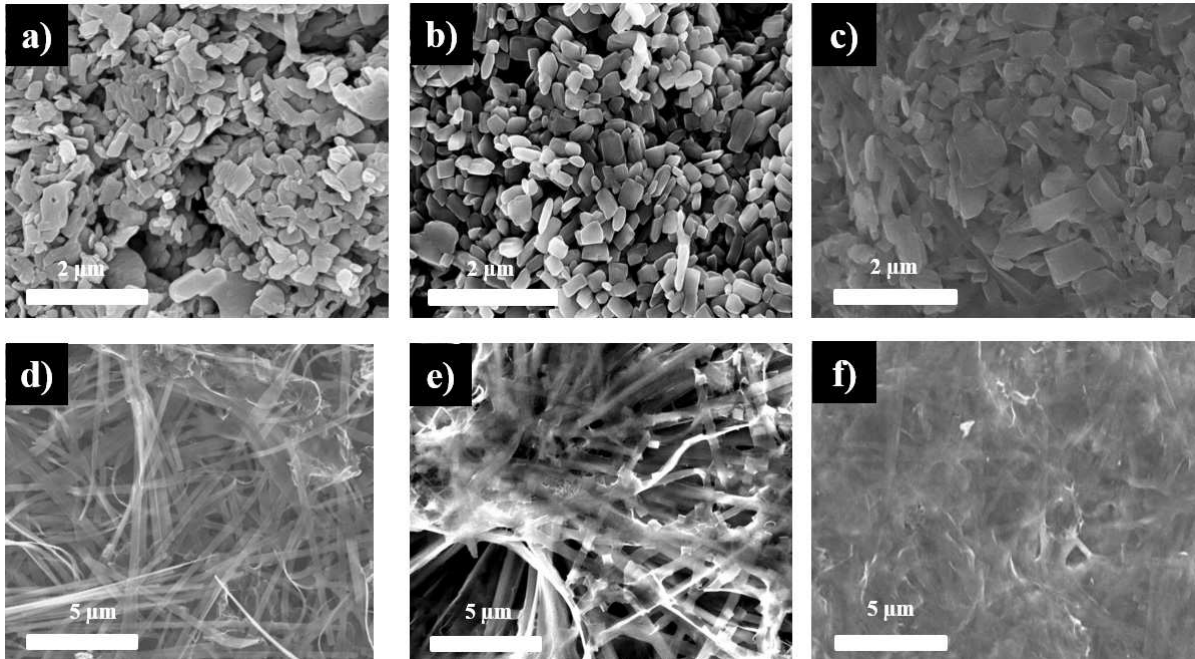


Fig. 3.2 SEM images of (a) pristine VO particles, (b) VO after the hydrothermal treatment, (c) VO with rGO after the hydrothermal treatment, and calcined GNVBs with the following ratios of VO and GO: (d) 3:1, (e) 1:1, and (f) 1:3.

(001) reflection at the peak position of 10.72° (8.25 \AA) [35]. When GO is reduced by external factors like a heat treatment or reducing chemical agents, etc., the peak position of the GO sheet shifts toward higher scattering angles, according to the degree of reduction. prGO synthesized by the hydrothermal method shows the (002) reflection at the peak position of 16° (5.54 \AA). The new peak appeared the (002) plane at 24° (3.71 \AA) is the characteristic of rGO. Most interestingly, the GNVBs show a very sharp characteristic rGO peak of the (002) plane at 24° (3.71 \AA) and, simultaneously, the (002) reflection of prGO at the peak position of 17.5° (5.07 \AA), which confirms that the mixing of V_2O_5 with GO under the identical hydrothermal conditions leads to the pronounced reduction of GO to rGO (shift of the (002) peak from 16 to 17.5°) [32, 36, 37].

Figure 3.4a shows a bright-field transmission electron microscopy (BF-TEM) image of VNB with a width of $\sim 200 \text{ nm}$ and the corresponding selective area electron diffraction (SAED) pattern. Orthorhombic crystal structure with a lattice parameter of $a = 12.30 \text{ \AA}$, $b = 3.81 \text{ \AA}$, $c = 13.98 \text{ \AA}$ is confirmed by the indexing of diffraction spots, which are larger than the pure VNBs lattice parameter values ($a = 11.722 \text{ \AA}$, $b = 3.570 \text{ \AA}$, $c = 11.520 \text{ \AA}$) [38]. The GNVB preferentially grows along the [010] direction. In order to identify the existence of carbon element inside the GNVBs, we employed scanning transmission electron microscopy (STEM, see Fig. 3.4b) and electron energy loss spectroscopy (EELS) technique. As shown in EELS, elemental mapping of Fig. 3.4c and 3.4d, carbon is detected at the whole GNVB region, but the distribution is uneven. Moreover, the point EELS spectrum (see Fig. 3.4e) clearly shows the strong carbon signal at the marked region of Fig. 3.4d. The bright contrast of STEM image, strong carbon signal, and increased lattice parameter may be due to the distribution of nano-sized rGO sheets between the V_2O_5 layers.

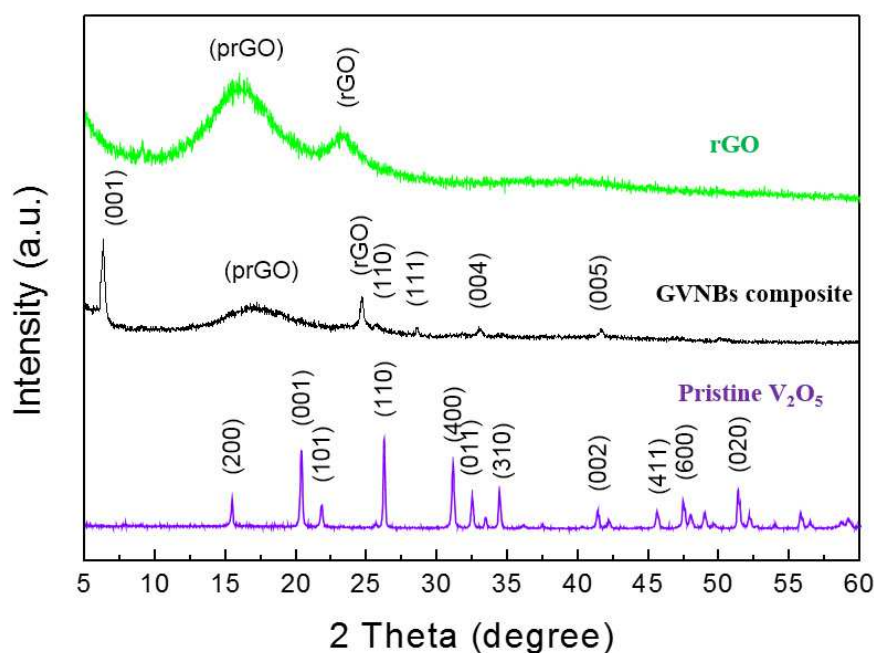


Fig. 3.3 XRD spectra of pristine V_2O_5 , composite GVNBs, and rGO measured in the 2θ range of 5° to 60° .

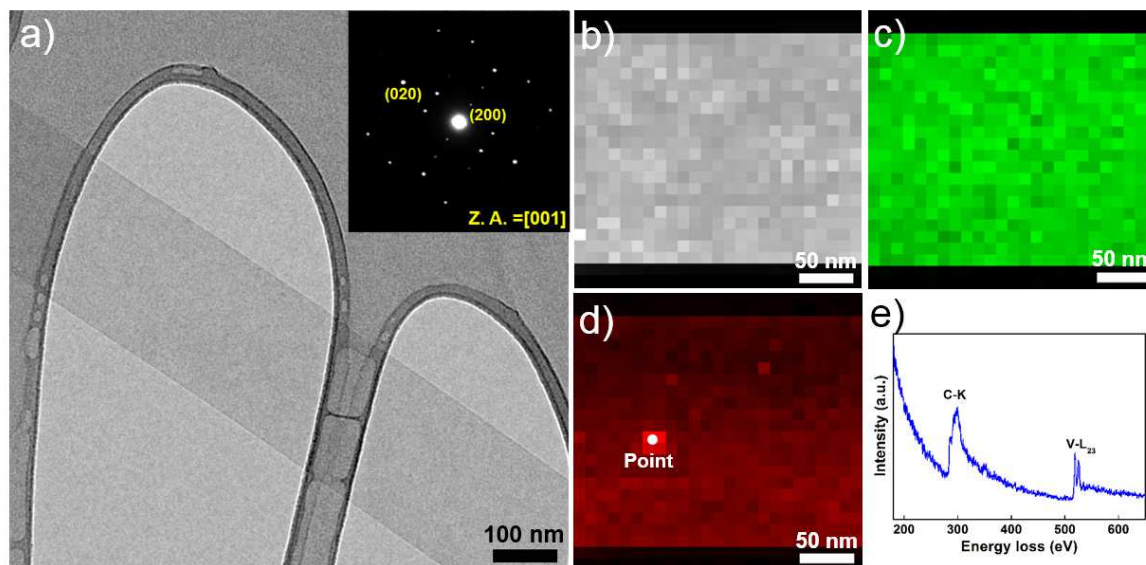


Fig. 3.4 BF-TEM image of VNB and corresponding SAED (inset) (a), HAADF-STEM image of VNB (b), the corresponding EELS elemental mapping of vanadium (c) and carbon (d), and EELS spectrum (e) acquired at the point of Fig. (d).

Figure A.1 (See Appendix A) shows the Raman spectrum of V_3G_1 , which reflects the interaction of VO and GO. The peak at 990 cm^{-1} corresponds to the stretching mode related to the vanadium-oxygen bond $V=O$ [39]. The peaks at 519 cm^{-1} and 688 cm^{-1} are assigned to the bending vibrations of V_3-O (triply coordinated oxygen) and V_2-O (doubly coordinated oxygen) bonds, respectively [40]. The peaks centered at 283 cm^{-1} and 403 cm^{-1} are attributed to the modes originating from y- and x-displacements

of O1 atoms, respectively [41]. High-frequency Raman peaks at 1352 cm^{-1} and 1590 cm^{-1} matched the D and G band of GO, respectively. The G band of GVNBS shows a little shift of up to 10 cm^{-1} compared to that of rGO, which may be due to the interaction between the GO and VO interfaces (Fig. A.1b, See Appendix A) [42, 43].

As evident from the V2p X-ray photoelectron spectroscopy (XPS) spectrum shown in Fig. A.2 (See Appendix A), the peaks located at 515.8 eV and 517.5 eV correspond to the +4 and +5 oxidation states of vanadium ions, respectively. The ratio of the two V2p peaks represents the quantitative information of two different vanadium ions (+4 and +5) in the composites. If VO and GO are mixed in DI water, after 1 day, a significant amount of V^{4+} ions is oxidized and the seeding is initiated in a direction, which is confirmed by the reduction in the ratio of V^{4+}/V^{5+} from 0.096 to 0.055. Following the hydrothermal reaction, the increase in the ratio of V^{4+}/V^{5+} (from 0.055 to 0.2524) was observed, which could be ascribed to the metastable state of vanadium oxide. The higher value of V^{4+}/V^{5+} (0.2524) compared to the previous report (0.153) might be due to the effect of external forces such as high pressure and temperature during the hydrothermal reaction [24]. Therefore, the mechanism of the nanobelts formation can be assumed as follows: The oxygen-containing functional groups present at the GO surface interact with the vanadium pentoxide surface. GO acts like an oxidizing agent, which oxidizes the vanadium ions from the partially existing V^{4+} to the V^{5+} soluble state during the reaction with GO. This intermediate compound is unstable and turns back into the stable +4 oxidation state (formation of VO seeds by trapping electrons from water molecules), and forms nanobelts [24, 44]. As suggested by Li et al., seeded V_2O_5 pieces gather together in the existence of rGO, gradually grows in a direction to form a nanobelt composite [45–49]. Figure A.3 (Appendix A) presents C1s XPS spectra of GO before and after the hydrothermal treatment, and mixture of GO and V_2O_5 (V_3G_1) after the hydrothermal treatment. Compared to pristine GO (GO before the hydrothermal treatment, Fig. A.3a), a lower amount of oxygen-containing functional groups at the surface of GO and a higher portion of C-C bonding is observed in Fig. A.3b and c, which shows that even the low-temperature hydrothermal treatment leads to the partial reduction of GO to rGO. Interestingly, a higher portion of C-C bonding (284.6 eV) is observed in Fig. A.3c, which may originate from the interaction of V_2O_5 with GO, in addition to the hydrothermal treatment [27, 36, 37, 44, 50]. As shown in Fig. A.4 (Appendix A), the width and thickness of a single nanobelt has been measured using atomic force microscopy (AFM) to be $(330 \pm 20)\text{ nm}$ and $(25 \pm 5)\text{ nm}$, respectively.

3.3.2 Electrochemical performance

The electrochemical performance of VO, rGO and GVNBS was measured in 1 M Na_2SO_4 electrolyte and the specific capacitance C_s (in $F\text{ g}^{-1}$) of the electroactive materials was calculated using CV (Eq. (2.1)), as well as galvanostatic charge/discharge curves (Eq. (2.2)). CV of the electroactive materials was carried out at a scan rate of 10 mV s^{-1} in the potential window of 0.0 to 0.8 V (Fig 3.5(a)). All curves retain their quasi-rectangular shape, which confirms ideal EDLC of the materials. The vanadium-rich composite (V_3G_1) shows a broad redox peak with retention of quasi-rectangular shape. The calculated C_s value of the electroactive materials V_3G_1 , V_1G_1 , V_1G_3 , rGO, and VO are 288, 244, 135, 28.8, and 24.8 F g^{-1} respectively. As expected, the three different composites of V_xG_y material (V_3G_1 , V_1G_1 , and V_1G_3) possess higher C_s values than graphene and VO. The enhanced capacitance of the V_xG_y materials is

attributed to the combination of non-faradaic (EDLC) and faradaic (redox) electrochemical processes. The intercalated rGO sheets provide high electrical conductivity and larger surface area, which enhances the EDLC (non-faradaic process) of the V_xG_y materials. Moreover, the V_2O_5 nanobelts have high surface area, layered crystal structure, and multivalent oxidation states of vanadium ions. These properties facilitate the insertion and extraction of alkali-metal ions (Li^+ , Na^+ , K^+ etc.,) near the surface of the electroactive material. The electrochemical sodium-ion insertion process can be expressed as follows [19]:



From Eq. (3.1), the charge/discharge processes involve the reversible intercalation of sodium ions into the layered V_2O_5 crystal structure with simultaneous electron transfer. This redox reaction leads to the partial reduction of V^{5+} to V^{4+} (and vice versa during oxidation) and thus provides the pseudocapacitance to the V_xG_y composites. Among the V_xG_y group of electroactive materials, the vanadium-rich composite V_3G_1 showed the highest C_s value of around 288 F g^{-1} (at the scan rate of 10 mV s^{-1}), which is higher than the previously reported capacitances in the works of Fu et al. [17] (graphene/vanadium-oxide nanotubes, 225 F g^{-1} @ 10 mV s^{-1} in $1 \text{ M Na}_2\text{SO}_4$ solution), and Bonso et al. [51] (composite of exfoliated graphite nanoplatelets and V_2O_5 nanotubes, 35 F g^{-1} @ 10 mV s^{-1} in 2 M KCl , 226 F g^{-1} @ 10 mV s^{-1} in LiTFSI electrolyte). The graphene-dominated composite V_1G_3 has a low content of V_2O_5 nanowires and also the porosity is limited by the existence of excess graphene (see SEM image Fig. 3.2(f)). Noticeably, the presently investigated graphene has a lower capacitance than the values reported in the literature [17, 52, 53]. The lower C_s value of graphene is ascribed to the low conductivity, which arises from the partial reduction of GO to rGO. Since the low-temperature hydrothermal synthesis was adopted and furthermore, no reducing chemical reagents are added in this work, the degree of reduction of GO to rGO is less compared to other methods [17–19, 54]. From the XRD analysis, the intensity of the rGO peak is smaller than that of the GO peak, which confirms the partial reduction of GO to rGO. In general, GO has lower conductivity than rGO due to the presence of oxygen-containing functional groups in the sp^3 -hybridized orbital [32, 33]. The lower C_s value of pristine V_2O_5 particles may arise from the smaller surface area and lower conductivity in comparison to V_2O_5 nanostructures [17, 55]. If the V_xG_y materials are synthesized hydrothermally at low temperature, the interaction between oxygen-containing functional groups (present in GO) and the V_2O_5 crystallites is significant, which leads to the pronounced conversion of GO to rGO (refer also to the XRD section and the mechanism for nanobelt formation). Therefore, all V_xG_y composites possess higher conductivity and capacitance than the individual components. Moreover, the presence of V_2O_5 nanobelts between the graphene sheets prohibits the re-stacking of graphene sheets, which further enhances the conductivity of graphene [53].

To further understand the electrochemical reversibility of the V_3G_1 composite, additional CV studies were performed at different scan rates (5, 10, 25, 50, 75, 100, and 125 mV s^{-1}) in $1 \text{ M Na}_2\text{SO}_4$ electrolyte solution. All CV curves retain their ideal quasi-rectangular shape even at higher scan rates (Fig. 3.5b), which is an indication of ideal capacitive behavior with excellent reversibility of this electrode material [19]. Fig. 3.5c shows the relationship between the specific capacitance of the electrode materials and the scan rate. By increasing the scan rate, the C_s value drops, which is a common phenomenon arising from the mass-transport limitation of sodium ions at high scan rates [56]. In detail, the interior (bulk

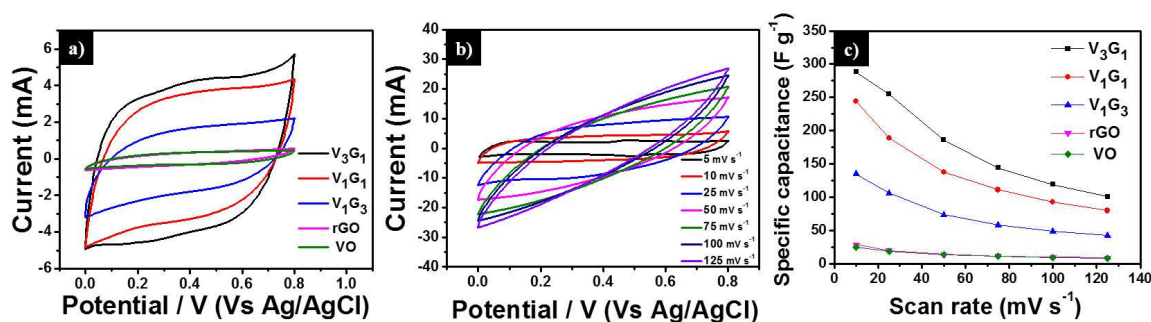


Fig. 3.5 (a) CV curves of rGO, pristine VO particles, V₁G₃, V₁G₁, and V₃G₁ electroactive materials measured at a scan rate of 10 mV s⁻¹ in 1 M Na₂SO₄ solution; (b) CV curves of the V₃G₁ electrode measured at different scan rates ranging from 5 to 125 mV s⁻¹; and (c) Specific capacitance calculated from the CV curves of Fig. (b) of the V₃G₁ electrode at various scan rates.

part) of the electrode cannot sustain the redox transition due to the diffusion limitation of ions within the electrode. Therefore, the part of the electrode surface is inaccessible for electrochemical reaction at higher scan rates, which leads to a lower capacitance.

Figure 3.6a shows the galvanostatic charge-discharge (CD) curves of graphene, pristine VO particles, and the three different V_xG_y composites obtained using 1 M Na₂SO₄ solution at a current density of 0.5 A g⁻¹. The C_s values of the electroactive materials V₃G₁, V₁G₁, V₁G₃, rGO, and VO are 128.8, 111.9, 117.5, 8.2, and 6.3 F g⁻¹ respectively. Consistent with the CV curves, the discharge time and the specific capacitance of the V_xG_y materials are higher than those of pristine V₂O₅ particles and graphene sheets. The CD profiles of the V₃G₁ and V₁G₁ composites are symmetric and resemble an equilateral triangle, which is an indication of a high rate capability during the CD process. The CD curve of the V₁G₃ composite deviates from the ideal linear relationship due to the poor conductivity of this material, which further limits its pseudocapacitance [17]. Fig. 3.6b presents the CD profiles of the V₃G₁ composite at various CD rates. All CD curves exhibit a nearly linear CD rate from low to high current densities, which is an indication of balanced faradaic and non-faradaic processes. At very low discharge current density of 0.25 A g⁻¹, the pseudocapacitance behavior is clearly visible, reflected in the non-linear shape of the CD curve, and the specific capacitance of 134 F g⁻¹ was observed. For higher current densities such as 0.5, 0.75 and 1 A g⁻¹, the respective specific capacitance values are calculated as 128.8, 108 and 103.9 F g⁻¹. Further the calculated specific capacitance values of V₁G₁ at various current densities (0.25, 0.5, 0.75 and 1 A g⁻¹) are as follows: 128, 111.9, 105 and 97.5 F g⁻¹. The graphene rich composition V₁G₃ has specific capacitance values of 121, 117.5, 88.1 and 55 F g⁻¹ at the same descending order of current density values.

Electrochemical impedance spectroscopy (EIS) is an ideal tool to analyze the internal resistance and capacitance of electrode materials. EIS experiments were carried out in the frequency range of 0.01 Hz to 100 kHz in aqueous 1 M Na₂SO₄ solution. Figure 3.6c represents the Nyquist plots of graphene, virgin V₂O₅ particles, and three different composites of V_xG_y electroactive materials. Each Nyquist plot shows a semicircle at high-to-medium frequencies and an inclined line at low frequency, which represent the charge-transfer and diffusion resistance, respectively. In the high-frequency region, the first intersection point with the real axis represents the total impedance of the bulk solution (R_s), electrodes

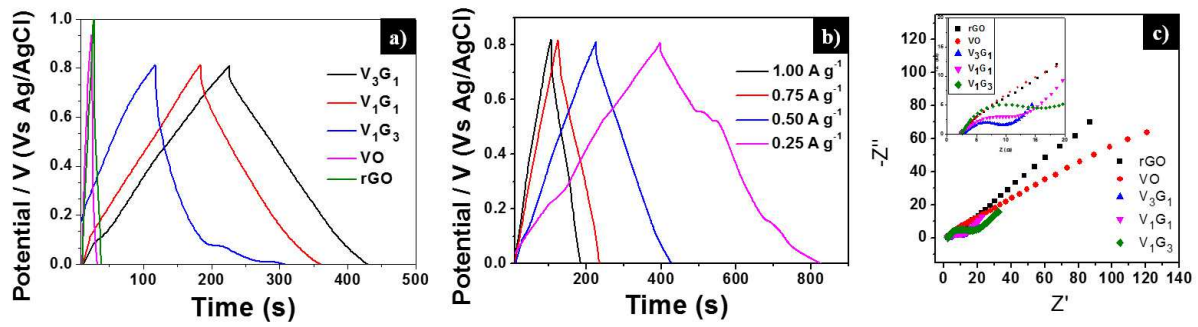


Fig. 3.6 (a) Galvanostatic charge-discharge curves of rGO, pristine VO particles, V_1G_3 , V_1G_1 , and V_3G_1 electroactive materials measured at a constant current density of 0.5 A g^{-1} in $1 \text{ M Na}_2\text{SO}_4$ solution; (b) Galvanostatic charge-discharge curves of V_3G_1 electrode material measured at various current densities; and (c) Electrochemical impedance spectra of rGO pristine V_2O_5 particles, V_1G_3 , V_1G_1 , and V_3G_1 electroactive materials measured in $1 \text{ M Na}_2\text{SO}_4$ solution. The inset shows an enhanced view of the high-to-medium frequency region.

(R_e), and the contact resistance (R_c) between electrode and current collector. At medium frequencies, the second intersection point of the semicircle with the real axis indicates the combination of the double-layer capacitance (C_{dl}) in parallel with the charge-transfer resistance (R_{ct}). The inclined line in the low-frequency region represents the Warburg impedance (W_s) corresponding to the diffusive resistance of the electrolyte in the interior part of the electrode surface. The R_{ct} values of VO, graphene, V_1G_3 , V_1G_1 , and V_3G_1 are 27.5, 20.2, 13.6, 9.2, and 5.7Ω respectively. The charge-transfer resistance of the V_xG_y materials is lower than in case of VO and graphene. The lower R_{ct} value of the V_xG_y materials leads to improved charge transfer and enhanced capacitance due to the following reasons: (i) V_2O_5 nanobelts having high surface area enhances the pseudocapacitance of the electrode material, (ii) V_xG_y materials possess highly conducting graphene sheets with high surface area improved the electronic conductivity of the GVNB composite and also enhance the electrochemical double-layer capacitance of the working electrode and (iii) the incorporation of V_2O_5 nanobelts between the graphene sheets prevents the agglomeration of graphene sheets which also enhances the conductivity.

Electrochemical cycling stability is one of the key factors that determines the applicability of this material to commercial supercapacitors. The cyclic stability of the V_3G_1 composite was measured by CV in the potential window of 0 to 0.8 V at a high scan rate of 200 mV s^{-1} for 5000 cycles. According to previous reports, the capacitance retention of pure vanadium oxide in aqueous electrolyte is very poor due to the structural damage caused by the insertion and desertion of electrolyte ions [17, 57]. In the present case, the V_3G_1 material retains 93 % of its initial capacitance value after 1000 cycles and, further, 82% capacitance retention is observed even after 5000 cycles which demonstrates excellent stability of the material with superior reversibility during the cycling test (Fig. 3.7a). This capacitance retention is much higher than that previously reported by Fu et al. [17] (48% retention after 5000 cycles @ 100 mV s^{-1} scan rate) and the best among vanadium oxide-based composite materials [19, 51]. EIS was measured after 5000 cycles for the post analysis of the electrode material. The shape of the EIS spectrum was similar to the initial spectrum, which comprises a semicircular arc in the high-frequency region and an inclined line in the low-frequency region. The R_{ct} value increased from 2.3 to 6.32Ω after 5000 cycles (see Fig. 3.7b). This might be induced by the adhesion loss between the electroactive material and the

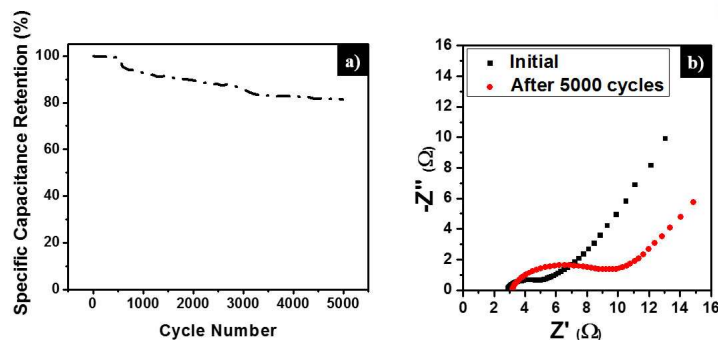


Fig. 3.7 (a) Specific capacitance retention of the V_3G_1 electrode as a function of cycle number, measured by CV at a scan rate of 200 mV s^{-1} in $1 \text{ M Na}_2\text{SO}_4$ solution; and (b) EIS analysis of the V_3G_1 electrode at the initial stage and after 5000 cycles.

current collector or due to the dissolution of a small amount of V_2O_5 in aqueous medium at a high scan rate (the change in color of the solution from white to yellow is an indication) [52, 58, 59]. From the electrochemical performance described above, we conclude that GVNBS could be a potential candidate for practical supercapacitor applications.

3.4 Summary

In summary, we have reported a facile method for the synthesis of GVNBS using a low-temperature hydrothermal process. GO played a vital role as a mild oxidizing agent for the formation of nanowires, as well as enhanced the conductivity of GVNBS. The insertion of rGO into the layered V_2O_5 crystal structure is confirmed by EELS analysis. The high surface area and pseudocapacitive nature of VNBS along with the enhanced conductivity of GVNBS upon addition of graphene resulted in an improved specific capacitance. Among various GVNBS, the V_2O_5 -rich composition, V_3G_1 showed the highest capacitance and long-term cycle life with the capacitance retention of 82% even after 5000 cycles.

References

- [1] Geim, A.K., Graphene: Status and prospects, *Science* 2009, 324 (5934), 1530–1534. doi:[10.1126/science.1158877](https://doi.org/10.1126/science.1158877).
- [2] Geim, A.K., Novoselov, K.S., The rise of graphene, *Nature Materials* 2007, 6 (3), 183–191. doi:[10.1038/nmat1849](https://doi.org/10.1038/nmat1849).
- [3] Yan, J., Wang, Q., Wei, T., Fan, Z., Recent advances in design and fabrication of electrochemical supercapacitors with high energy densities, *Advanced Energy Materials* 2014, 4 (4), n/a–n/a. doi:[10.1002/aenm.201300816](https://doi.org/10.1002/aenm.201300816).
- [4] Wang, Y., Takahashi, K., Lee, K., Cao, G., Nanostructured vanadium oxide electrodes for enhanced lithium-ion intercalation, *Advanced Functional Materials* 2006, 16 (9), 1133–1144. doi:[10.1002/adfm.200500662](https://doi.org/10.1002/adfm.200500662).

- [5] Wang, Y., Cao, G., Developments in nanostructured cathode materials for high-performance lithium-ion batteries, *Advanced Materials* 2008, 20 (12), 2251–2269. doi:[10.1002/adma.200702242](https://doi.org/10.1002/adma.200702242).
- [6] Cao, A.M., Hu, J.S., Liang, H.P., Wan, L.J., Self-assembled vanadium pentoxide (V_2O_5) hollow microspheres from nanorods and their application in lithium-ion batteries, *Angewandte Chemie International Edition* 2005, 44 (28), 4391–4395. doi:[10.1002/anie.200500946](https://doi.org/10.1002/anie.200500946).
- [7] Liu, J., Xia, H., Xue, D., Lu, L., Double-shelled nanocapsules of V_2O_5 -based composites as high-performance anode and cathode materials for li ion batteries, *Journal of the American Chemical Society* 2009, 131 (34), 12086–12087. doi:[10.1021/ja9053256](https://doi.org/10.1021/ja9053256).
- [8] Dexmer, J., Leroy, C.M., Binet, L., Heresanu, V., Launois, P., Steunou, N., Coulon, C., Maquet, J., Brun, N., Livage, J., Backov, R., Vanadium oxide-pani nanocomposite-based macroscopic fibers: 1d alcohol sensors bearing enhanced toughness, *Chemistry of Materials* 2008, 20 (17), 5541–5549. doi:[10.1021/cm800886v](https://doi.org/10.1021/cm800886v).
- [9] Kim, G.T., Muster, J., Krstic, V., Park, J.G., Park, Y.W., Roth, S., Burghard, M., Field-effect transistor made of individual V_2O_5 nanofibers, *Applied Physics Letters* 2000, 76 (14), 1875–1877. doi:[10.1063/1.126197](https://doi.org/10.1063/1.126197).
- [10] Wee, G., Soh, H.Z., Cheah, Y.L., Mhaisalkar, S.G., Srinivasan, M., Synthesis and electrochemical properties of electrospun V_2O_5 nanofibers as supercapacitor electrodes, *J. Mater. Chem.* 2010, 20, 6720–6725. doi:[10.1039/C0JM00059K](https://doi.org/10.1039/C0JM00059K).
- [11] Arico, A.S., Bruce, P., Scrosati, B., Tarascon, J.M., van Schalkwijk, W., Nanostructured materials for advanced energy conversion and storage devices, *Nature Materials* 2005, 4 (5), 366–377.
- [12] Bruce, P., Scrosati, B., Tarascon, J.M., Nanomaterials for rechargeable lithium batteries, *Angewandte Chemie International Edition* 2008, 47 (16), 2930–2946. doi:[10.1002/anie.200702505](https://doi.org/10.1002/anie.200702505).
- [13] Lee, J.W., Lim, S.Y., Jeong, H.M., Hwang, T.H., Kang, J.K., Choi, J.W., Extremely stable cycling of ultra-thin V_2O_5 nanowire-graphene electrodes for lithium rechargeable battery cathodes, *Energy Environ. Sci.* 2012, 5, 9889–9894. doi:[10.1039/C2EE22004K](https://doi.org/10.1039/C2EE22004K).
- [14] Sathiya, M., Prakash, A.S., Ramesha, K., Tarascon, J., Shukla, A.K., V_2O_5 -anchored carbon nanotubes for enhanced electrochemical energy storage, *Journal of the American Chemical Society* 2011, 133 (40), 16291–16299. doi:[10.1021/ja207285b](https://doi.org/10.1021/ja207285b).
- [15] Perera, S.D., Patel, B., Nijem, N., Roodenko, K., Seitz, O., Ferraris, J.P., Chabal, Y.J., Balkus, K.J., Vanadium oxide nanowire-carbon nanotube binder-free flexible electrodes for supercapacitors, *Advanced Energy Materials* 2011, 1 (5), 936–945. doi:[10.1002/aenm.201100221](https://doi.org/10.1002/aenm.201100221).
- [16] Wang, Y., Cao, G., Synthesis and enhanced intercalation properties of nanostructured vanadium oxides, *Chemistry of Materials* 2006, 18 (12), 2787–2804. doi:[10.1021/cm052765h](https://doi.org/10.1021/cm052765h).
- [17] Fu, M., Ge, C., Hou, Z., Cao, J., He, B., Zeng, F., Kuang, Y., Graphene/vanadium oxide nanotubes composite as electrode material for electrochemical capacitors, *Physica B: Condensed Matter* 2013, 421, 77 – 82. doi:[10.1016/j.physb.2013.04.013](https://doi.org/10.1016/j.physb.2013.04.013).

- [18] Zhao, H., Pan, L., Xing, S., Luo, J., Xu, J., Vanadium oxides-reduced graphene oxide composite for lithium-ion batteries and supercapacitors with improved electrochemical performance, *Journal of Power Sources* 2013, 222, 21 – 31. doi:[10.1016/j.jpowsour.2012.08.036](https://doi.org/10.1016/j.jpowsour.2012.08.036).
- [19] Perera, S.D., Liyanage, A.D., Nijem, N., Ferraris, J.P., Chabal, Y.J., Jr., K.J.B., Vanadium oxide nanowire-graphene binder free nanocomposite paper electrodes for supercapacitors: A facile green approach, *Journal of Power Sources* 2013, 230, 130 – 137. doi:[10.1016/j.jpowsour.2012.11.118](https://doi.org/10.1016/j.jpowsour.2012.11.118).
- [20] Stankovich, S., Dikin, D.A., Piner, R.D., Kohlhaas, K.A., Kleinhammes, A., Jia, Y., Wu, Y., Nguyen, S.T., Ruoff, R.S., Synthesis of graphene-based nanosheets via chemical reduction of exfoliated graphite oxide, *Carbon* 2007, 45 (7), 1558 – 1565. doi:[10.1016/j.carbon.2007.02.034](https://doi.org/10.1016/j.carbon.2007.02.034).
- [21] Li, D., Muller, M.B., Gilje, S., Kaner, R.B., Wallace, G.G., Processable aqueous dispersions of graphene nanosheets, *Nature Nanotechnology* 2008, 3 (2), 101–105.
- [22] Shin, H.J., Kim, K.K., Benayad, A., Yoon, S.M., Park, H.K., Jung, I.S., Jin, M.H., Jeong, H.K., Kim, J.M., Choi, J.Y., Lee, Y.H., Efficient reduction of graphite oxide by sodium borohydride and its effect on electrical conductance, *Advanced Functional Materials* 2009, 19 (12), 1987–1992. doi:[10.1002/adfm.200900167](https://doi.org/10.1002/adfm.200900167).
- [23] Becerril, H.A., Mao, J., Liu, Z., Stoltenberg, R.M., Bao, Z., Chen, Y., Evaluation of solution-processed reduced graphene oxide films as transparent conductors, *ACS Nano* 2008, 2 (3), 463–470. doi:[10.1021/nn700375n](https://doi.org/10.1021/nn700375n).
- [24] Lee, M., Hong, W.G., Jeong, H.Y., Balasingam, S.K., Lee, Z., Chang, S.J., Kim, B.H., Jun, Y., Graphene oxide assisted spontaneous growth of V₂O₅ nanowires at room temperature, *Nanoscale* 2014, 6, 11066–11071. doi:[10.1039/C4NR01780C](https://doi.org/10.1039/C4NR01780C).
- [25] Tung, V.C., Allen, M.J., Yang, Y., Kaner, R.B., High-throughput solution processing of large-scale graphene, *Nature Nanotechnology* 2009, 4 (1), 25–29. doi:[10.1038/nnano.2008.329](https://doi.org/10.1038/nnano.2008.329).
- [26] Wang, X., Zhi, L., Müllen, K., Transparent, conductive graphene electrodes for dye-sensitized solar cells, *Nano Letters* 2008, 8 (1), 323–327. doi:[10.1021/nl072838r](https://doi.org/10.1021/nl072838r).
- [27] Zhou, Y., Bao, Q., Tang, L.A.L., Zhong, Y., Loh, K.P., Hydrothermal dehydration for the "green" reduction of exfoliated graphene oxide to graphene and demonstration of tunable optical limiting properties, *Chemistry of Materials* 2009, 21 (13), 2950–2956. doi:[10.1021/cm9006603](https://doi.org/10.1021/cm9006603).
- [28] Yu, J., Yu, J.C., Ho, W., Wu, L., Wang, X., A simple and general method for the synthesis of multicomponent Na₂V₆O₁₆·3H₂O single-crystal nanobelts, *Journal of the American Chemical Society* 2004, 126 (11), 3422–3423. doi:[10.1021/ja031795n](https://doi.org/10.1021/ja031795n).
- [29] Avansi Jr., W., Ribeiro, C., Leite, E.R., Mastelaro, V.R., Vanadium pentoxide nanostructures: An effective control of morphology and crystal structure in hydrothermal conditions, *Crystal Growth & Design* 2009, 9 (8), 3626–3631. doi:[10.1021/cg900373f](https://doi.org/10.1021/cg900373f).
- [30] Xiong, C., Aliev, A.E., Gnade, B., Balkus, K.J., Fabrication of silver vanadium oxide and V₂O₅ nanowires for electrochromics, *ACS Nano* 2008, 2 (2), 293–301. doi:[10.1021/nn700261c](https://doi.org/10.1021/nn700261c).

- [31] Kim, B.H., Yu, H.Y., Hong, W.G., Park, J., Jung, S.C., Nam, Y., Jeong, H.Y., Park, Y.W., Jun, Y., Kim, H.J., Hydrogen spillover in pd-doped V_2O_5 nanowires at room temperature, *Chemistry - An Asian Journal* 2012, 7 (4), 684–687. doi:[10.1002/asia.201100947](https://doi.org/10.1002/asia.201100947).
- [32] Kim, B.H., Hong, W.G., Moon, H.R., Lee, S.M., Kim, J.M., Kang, S., Jun, Y., Kim, H.J., Investigation on the existence of optimum interlayer distance for H_2 uptake using pillared-graphene oxide, *International Journal of Hydrogen Energy* 2012, 37 (19), 14217 – 14222. doi:[10.1016/j.ijhydene.2012.07.029](https://doi.org/10.1016/j.ijhydene.2012.07.029).
- [33] Dreyer, D.R., Park, S., Bielawski, C.W., Ruoff, R.S., The chemistry of graphene oxide, *Chem. Soc. Rev.* 2010, 39, 228–240. doi:[10.1039/B917103G](https://doi.org/10.1039/B917103G).
- [34] Nethravathi, C., Rajamathi, M., Chemically modified graphene sheets produced by the solvothermal reduction of colloidal dispersions of graphite oxide, *Carbon* 2008, 46 (14), 1994 – 1998. doi:[10.1016/j.carbon.2008.08.013](https://doi.org/10.1016/j.carbon.2008.08.013).
- [35] Hong, W.G., Kim, B.H., Lee, S.M., Yu, H.Y., Yun, Y.J., Jun, Y., Lee, J.B., Kim, H.J., Agent-free synthesis of graphene oxide/transition metal oxide composites and its application for hydrogen storage, *International Journal of Hydrogen Energy* 2012, 37 (9), 7594 – 7599. doi:[10.1016/j.ijhydene.2012.02.010](https://doi.org/10.1016/j.ijhydene.2012.02.010).
- [36] Rout, C.S., Kim, B.H., Xu, X., Yang, J., Jeong, H.Y., Odkhuu, D., Park, N., Cho, J., Shin, H.S., Synthesis and characterization of patronite form of vanadium sulfide on graphitic layer, *Journal of the American Chemical Society* 2013, 135 (23), 8720–8725. doi:[10.1021/ja403232d](https://doi.org/10.1021/ja403232d).
- [37] Nam, I., Kim, N.D., Kim, G.P., Park, J., Yi, J., One step preparation of Mn_3O_4 /graphene composites for use as an anode in li ion batteries, *Journal of Power Sources* 2013, 244, 56 – 62. doi:[10.1016/j.jpowsour.2013.04.055](https://doi.org/10.1016/j.jpowsour.2013.04.055).
- [38] Petkov, V., Trikalitis, P.N., Bozin, E.S., Billinge, S.J.L., Vogt, T., Kanatzidis, M.G., Structure of $v_2o_5-nh_2o$ xerogel solved by the atomic pair distribution function technique, *Journal of the American Chemical Society* 2002, 124 (34), 10157–10162. doi:[10.1021/ja026143y](https://doi.org/10.1021/ja026143y).
- [39] Fang, W.C., Synthesis and electrochemical characterization of vanadium oxide/carbon nanotube composites for supercapacitors, *The Journal of Physical Chemistry C* 2008, 112 (30), 11552–11555. doi:[10.1021/jp8011602](https://doi.org/10.1021/jp8011602).
- [40] Yan, B., Liao, L., You, Y., Xu, X., Zheng, Z., Shen, Z., Ma, J., Tong, L., Yu, T., Single-crystalline V_2O_5 ultralong nanoribbon waveguides, *Advanced Materials* 2009, 21 (23), 2436–2440. doi:[10.1002/adma.200803684](https://doi.org/10.1002/adma.200803684).
- [41] Baddour-Hadjean, R., Pereira-Ramos, J.P., Navone, C., Smirnov, M., Raman microspectrometry study of electrochemical lithium intercalation into sputtered crystalline V_2O_5 thin films, *Chemistry of Materials* 2008, 20 (5), 1916–1923. doi:[10.1021/cm702979k](https://doi.org/10.1021/cm702979k).
- [42] Tsukamoto, T., Yamazaki, K., Komurasaki, H., Ogino, T., Effects of surface chemistry of substrates on raman spectra in graphene, *The Journal of Physical Chemistry C* 2012, 116 (7), 4732–4737. doi:[10.1021/jp2113158](https://doi.org/10.1021/jp2113158).

- [43] Das, A., Chakraborty, B., Sood, A., Raman spectroscopy of graphene on different substrates and influence of defects, *Bulletin of Materials Science* 2008, 31 (3), 579–584. doi:[10.1007/s12034-008-0090-5](https://doi.org/10.1007/s12034-008-0090-5).
- [44] Liu, H., Yang, W., Ultralong single crystalline V_2O_5 nanowire/graphene composite fabricated by a facile green approach and its lithium storage behavior, *Energy Environ. Sci.* 2011, 4, 4000–4008. doi:[10.1039/C1EE01353J](https://doi.org/10.1039/C1EE01353J).
- [45] Ren, X., Jiang, Y., Zhang, P., Liu, J., Zhang, Q., Preparation and electrochemical properties of V_2O_5 submicron-belts synthesized by a sol-gel H_2O_2 route, *Journal of Sol-Gel Science and Technology* 2009, 51 (2), 133–138. doi:[10.1007/s10971-009-2002-6](https://doi.org/10.1007/s10971-009-2002-6).
- [46] Zhou, F., Zhao, X., Yuan, C., Li, L., Xu, H., Low-temperature hydrothermal synthesis of orthorhombic vanadium pentoxide nanowires, *Chemistry Letters* 2007, 36 (2), 310–311. doi:[10.1246/cl.2007.310](https://doi.org/10.1246/cl.2007.310).
- [47] Zhou, F., Zhao, X., Liu, Y., Yuan, C., Li, L., Synthesis of millimeter-range orthorhombic V_2O_5 nanowires and impact of thermodynamic and kinetic properties of the oxidant on the synthetic process, *European Journal of Inorganic Chemistry* 2008, 2008 (16), 2506–2509. doi:[10.1002/ejic.200800148](https://doi.org/10.1002/ejic.200800148).
- [48] Livage, J., Vanadium pentoxide gels, *Chemistry of Materials* 1991, 3 (4), 578–593. doi:[10.1021/cm00016a006](https://doi.org/10.1021/cm00016a006).
- [49] Li, M., Kong, F., Wang, H., Li, G., Synthesis of vanadium pentoxide (V_2O_5) ultralong nanobelts via an oriented attachment growth mechanism, *CrystEngComm* 2011, 13, 5317–5320. doi:[10.1039/C1CE05477E](https://doi.org/10.1039/C1CE05477E).
- [50] Xu, L., Zhang, G., Chen, J., Zhou, Y., Yuan, G., Yang, F., Spontaneous redox synthesis of prussian blue/graphene nanocomposite as a non-precious metal catalyst for efficient four-electron oxygen reduction in acidic medium, *Journal of Power Sources* 2013, 240, 101 – 108. doi:[10.1016/j.jpowsour.2013.03.156](https://doi.org/10.1016/j.jpowsour.2013.03.156).
- [51] Bonso, J.S., Rahy, A., Perera, S.D., Nour, N., Seitz, O., Chabal, Y.J., Balkus Jr., K.J., Ferraris, J.P., Yang, D.J., Exfoliated graphite nanoplatelets- V_2O_5 nanotube composite electrodes for supercapacitors, *Journal of Power Sources* 2012, 203, 227–232. doi:[10.1016/j.jpowsour.2011.09.084](https://doi.org/10.1016/j.jpowsour.2011.09.084).
- [52] Ramadoss, A., Kim, S.J., Improved activity of a graphene- TiO_2 hybrid electrode in an electrochemical supercapacitor, *Carbon* 2013, 63, 434 – 445. doi:[10.1016/j.carbon.2013.07.006](https://doi.org/10.1016/j.carbon.2013.07.006).
- [53] Ramadoss, A., Kim, G.S., Kim, S.J., Fabrication of reduced graphene oxide/ TiO_2 nanorod/reduced graphene oxide hybrid nanostructures as electrode materials for supercapacitor applications, *CrystEngComm* 2013, 15, 10222–10229. doi:[10.1039/C3CE41517A](https://doi.org/10.1039/C3CE41517A).
- [54] Yang, S., Gong, Y., Liu, Z., Zhan, L., Hashim, D.P., Ma, L., Vajtai, R., Ajayan, P.M., Bottom-up approach toward single-crystalline VO_2 -graphene ribbons as cathodes for ultrafast lithium storage, *Nano Letters* 2013, 13 (4), 1596–1601. doi:[10.1021/nl400001u](https://doi.org/10.1021/nl400001u).

- [55] Qu, Q., Zhu, Y., Gao, X., Wu, Y., Core-shell structure of polypyrrole grown on V_2O_5 nanoribbon as high performance anode material for supercapacitors, *Advanced Energy Materials* 2012, 2 (8), 950–955. doi:[10.1002/aenm.201200088](https://doi.org/10.1002/aenm.201200088).
- [56] Liu, W.w., Yan, X.b., Xue, Q.j., Multilayer hybrid films consisting of alternating graphene and titanium dioxide for high-performance supercapacitors, *J. Mater. Chem. C* 2013, 1, 1413–1422. doi:[10.1039/C2TC00563H](https://doi.org/10.1039/C2TC00563H).
- [57] Reddy, R.N., Reddy, R.G., Porous structured vanadium oxide electrode material for electrochemical capacitors, *Journal of Power Sources* 2006, 156 (2), 700 – 704. doi:[10.1016/j.jpowsour.2005.05.071](https://doi.org/10.1016/j.jpowsour.2005.05.071).
- [58] Yan, J., Wei, T., Qiao, W., Shao, B., Zhao, Q., Zhang, L., Fan, Z., Rapid microwave-assisted synthesis of graphene nanosheet/ Co_3O_4 composite for supercapacitors, *Electrochimica Acta* 2010, 55 (23), 6973 – 6978. doi:[10.1016/j.electacta.2010.06.081](https://doi.org/10.1016/j.electacta.2010.06.081).
- [59] Yan, J., Fan, Z., Wei, T., Qian, W., Zhang, M., Wei, F., Fast and reversible surface redox reaction of graphene- MnO_2 composites as supercapacitor electrodes, *Carbon* 2010, 48 (13), 3825 – 3833. doi:[10.1016/j.carbon.2010.06.047](https://doi.org/10.1016/j.carbon.2010.06.047).

Part II

Nanostructured Transition Metal Dichalcogenides/rGO Electrodes

Freeze-dried MoS₂ Nanosheets

4.1 Introduction

Recently, researchers have given much attention to the use of transition metal dichalcogenide-based electroactive materials in various electrochemical applications, including sensors, catalysis, batteries, and supercapacitors. This is due to their advantageous properties, which include: (i) high surface area; (ii) 2-dimensional sheet-like morphologies having layered crystal structures; (iii) high electrical conductivity when compared to metal oxides; and (iv) the potential for Faradaic charge transfer processes on the multi-valent transition metal centers [1–3]. The electrochemical double-layer capacitance (EDLC) of MoS₂ nanowall film was first reported by Soon and Loh in 2007, which inspired the researchers to investigate various transition metal dichalcogenides (TMDCs) for supercapacitor applications [4]. Since then, a number of papers have been published on the use of MoS₂, MoS₂/carbon, and MoS₂/conducting polymer-based composite materials for supercapacitor applications [4–17]. Notably, the reported specific capacitance of pristine MoS₂ electrode materials appears to depend mainly on the electrical conductivity and high surface area of the electroactive material [15, 18]. Although MoS₂ possesses a maximum theoretical capacitance of 1000 A g⁻¹ [17], the highest specific capacitance achieved to date is approximately 403 A g⁻¹ (at a scan rate of 1 mV s⁻¹ in KCl electrolyte using a three electrode configuration), reported by Ramadoss et al. for a pristine mesoporous MoS₂ nanostructured material [16, 19, 20]. In a recent report, highly conductive metallic 1T phase MoS₂ nanosheet electrodes were also employed in supercapacitors. Although these electrodes showed high volumetric capacitance, their gravimetric capacitance was quite low [15]. In general, synthesis of MoS₂ by various methods forms a 2-D sheet-like morphology with high surface area. However, the final stage of the filtration and drying process leads to the agglomeration of these 2-D sheets, which can reduce the effective surface area of the nanomaterials, as illustrated in Appendix B. In this work, we have synthesized high surface area sponge-like MoS₂ sheets using a facile hydrothermal method, followed by freeze-drying.

4.2 Experimental

4.2.1 Synthesis of MoS₂ sponge material

A schematic illustration of the synthesis of high surface area MoS₂ sponge material is shown in Fig. 4.1. Molybdic acid, (MAA, H₂MoO₄) and thioacetamide (TAA, CH₃CSNH₂) were purchased from Sigma-Aldrich Corporation. MAA (0.121 g) and TAA (0.225 g) were accurately weighed and then dissolved

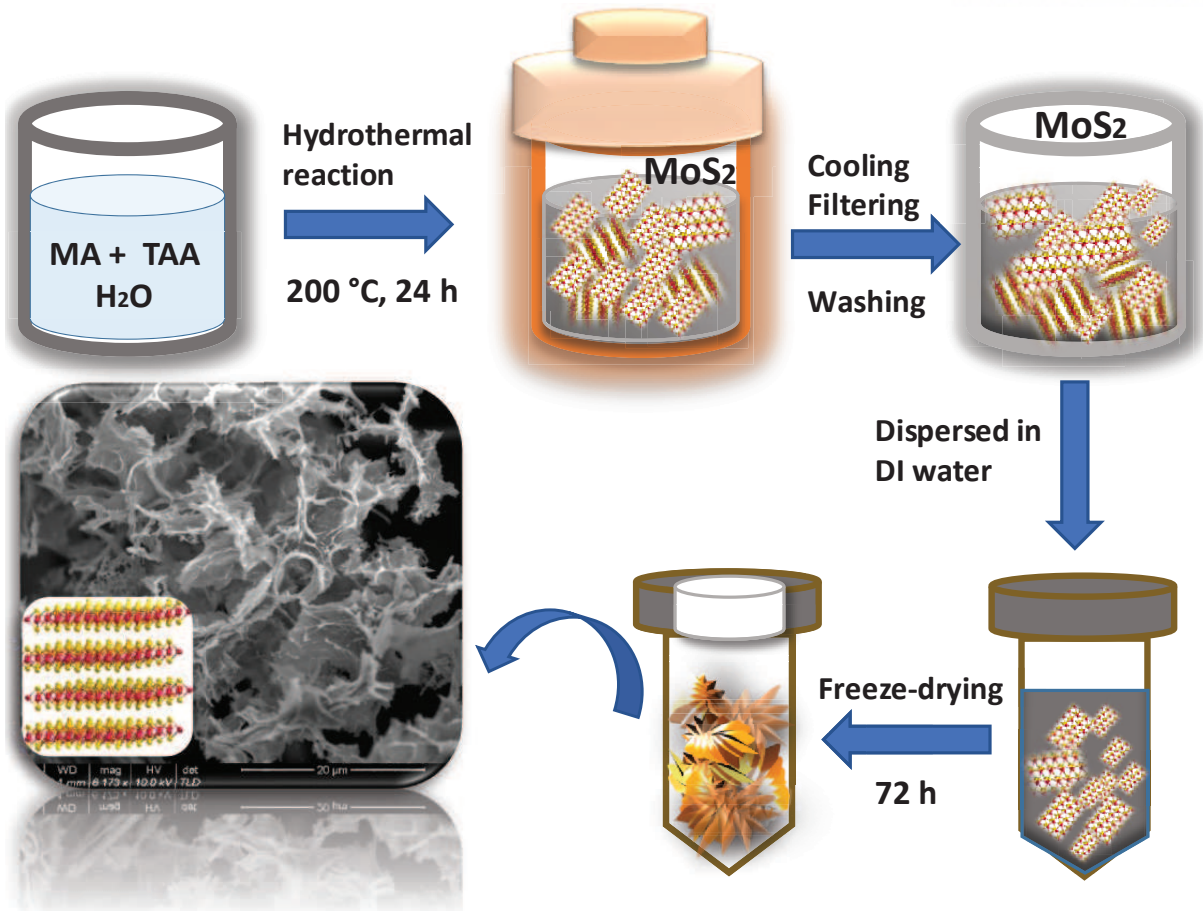


Fig. 4.1 Schematic illustration of the synthesis of MoS₂ sponge material by the hydrothermal method followed by freeze-drying.

into 80 ml of deionized (DI) water, with continuous stirring for 15 min in order to achieve complete dissolution. The resulting solution was transferred into a Teflon-lined autoclave and sealed tightly. The autoclave was then placed inside an electric oven and heated to 200 °C for 24 h. The solution-based chemical reaction under high pressure and temperature followed Eqs. (4.1a) and (4.1b). Hydrogen sulfide formed by hydrolysis of TAA, then acted as a reducing agent to convert molybdc acid into MoS₂ [21, 22]. Once the hydrothermal reaction was completed, the autoclave was kept inside the electric oven until it cooled down naturally to room temperature. The resulting black precipitate was washed thoroughly with DI water and filtered through Whatman filter paper. After filtration, the precipitate was dispersed in DI water and sonicated for an hour to prevent agglomeration of the MoS₂ sheets. The resulting material was freeze-dried for 72 h to yield the high surface area sponge-like MoS₂ structure. For comparison purposes, some of the filtered precipitate was dried in an electric oven at 50 °C for 12 h. The resultant product was ground using a pestle and mortar, then examined in the morphological studies.



4.2.2 Materials characterization

Surface morphology of the freeze-dried material was examined using scanning electron microscopy (NanoSEM, S-3400N) and high-resolution transmission electron microscopy (HR-TEM, JEOL-2100F). The crystal structure and elemental composition of the MoS₂ sponge were confirmed by X-ray diffraction (XRD, Bruker-D8 ADVANCE) using Cu K α emission ($\lambda = 1.5406 \text{ \AA}$) with a step-size of 0.02° , X-ray photoelectron spectroscopy (XPS, Thermo Fisher, UK), and Raman spectroscopy (WITech, alpha300R) using 532 nm laser excitation, after calibrating the Raman shift with a silicon reference at 521 cm^{-1} .

4.2.3 Cell fabrication and electrochemical measurement of supercapacitors

The high surface area freeze-dried electroactive MoS₂ material, carbon black, and poly(vinylidene fluoride) were mixed in a mass ratio of 8:1:1 to obtain a slurry and then coated on a 1 cm^2 stainless steel (SS) substrate using brush. The mass loading of each electrode was approximately 5 mg/cm^2 . Each 1 cm^2 area of MoS₂ sponge material coated SS substrate was used as a single electrode. To fabricate a symmetrical capacitor, one electrode was placed inside the test cell rig, a Whatman filter paper separator was placed on it followed by addition of a few drops of $0.5 \text{ M H}_2\text{SO}_4$ onto the separator, and then finally another electrode was placed over the separator. The test cell was sealed with an O-ring and then left for a few hours to ensure uniform soaking of the electrodes with the electrolyte solution. All electrochemical experiments were conducted at room temperature using a multi-channel potentiostat/galvanostat (Biologic/VSP). Cyclic voltammetry (CV) curves were obtained at various scan rates (2, 5, 10, 25, 50, 75, 100, and 125 mV s^{-1}) in a potential window of -0.4 to 0.6 V . Galvanostatic charge-discharge (CD) measurements were performed at various current densities ($0.10, 0.25, 0.50, 0.75, 1, 2, \text{ and } 3 \text{ A g}^{-1}$) using the same potential window used in CV. Electrochemical impedance spectroscopy (EIS) measurements were performed over a frequency range of 0.01 Hz to 100 kHz with an AC amplitude of 10 mV and a 0 V DC bias. The cycle lifetime of the symmetric device was tested using charge-discharge measurements at a current density of 2 A g^{-1} for 4000 cycles.

4.3 Results and Discussion

4.3.1 Physico-chemical analysis

The structural conformation of the as-synthesized sponge-like MoS₂ was characterized using X-ray diffraction (XRD). As shown in Fig. 4.2, the peaks corresponding to the (002), (100), (104), and (110) planes confirmed the formation of a hexagonal crystal structure (JCPDS 65-0160) belonging to the space group P6₃/mmc. To further confirm the structure, the Raman spectrum was also measured and the corresponding in-plane (E_{2g}^1) and out-of-plane (A_{1g}) Raman active modes of MoS₂ were observed at 380.5 and 403.3 cm^{-1} , respectively (see Fig. 4.3).

The surface morphology of the MoS₂ sponge material was studied using electron microscopy. Figure 4.4 (top row) show the field emission scanning electron microscopic (FE-SEM) images of the MoS₂ sponge-like material at low and high magnification. The high magnification image clearly shows that the freeze-dried MoS₂ sponge had high surface area and that the individual flakes were very thin. The

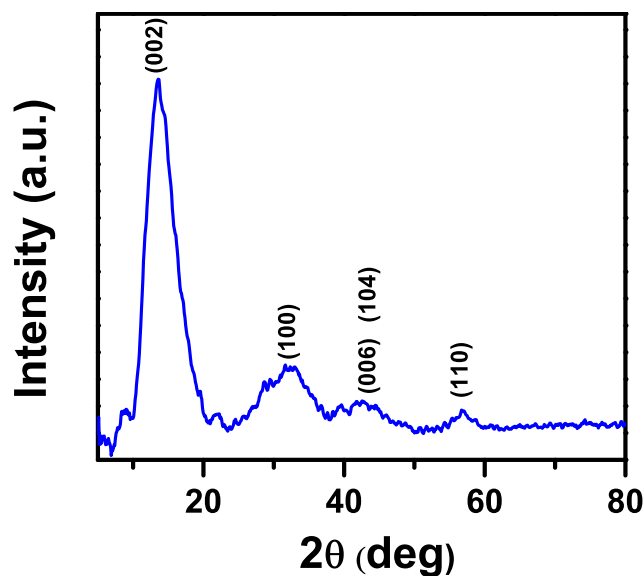


Fig. 4.2 XRD spectrum of as-synthesized MoS₂ sponge materials.

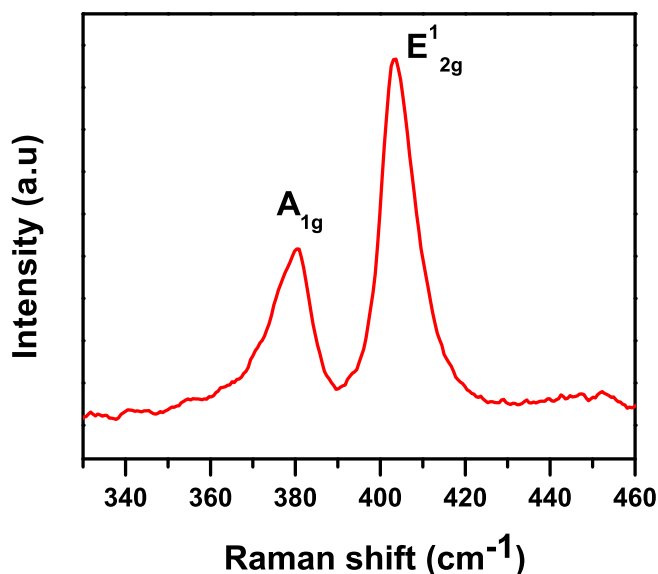


Fig. 4.3 Raman spectrum of the MoS₂ sponges showing A_{1g} and E_{2g}¹ Raman modes.

high-resolution transmission electron microscopic (HR-TEM) images at low and high magnification are shown in Fig. 4.4 (bottom row). These indicate that each MoS₂ flake consisted of less than 10 layers of MoS₂ sheets, with interlayer thicknesses of approximately 0.65 nm. The inset displayed in Figure 2f is the corresponding Fast Fourier Transform (FFT) pattern of the high magnification TEM image, which further confirms the crystalline nature of the MoS₂ sponge.

4.3.2 Electrochemical performance of symmetrical cells

The electrochemical performance of the as-synthesized MoS₂ sponge electrode was tested for supercapacitor applications under a symmetric two-electrode cell configuration. Figure. 4.5 depicts the cyclic voltammogram (CV) curves measured at different scan rates using an aqueous 0.5 M H₂SO₄ electrolyte.

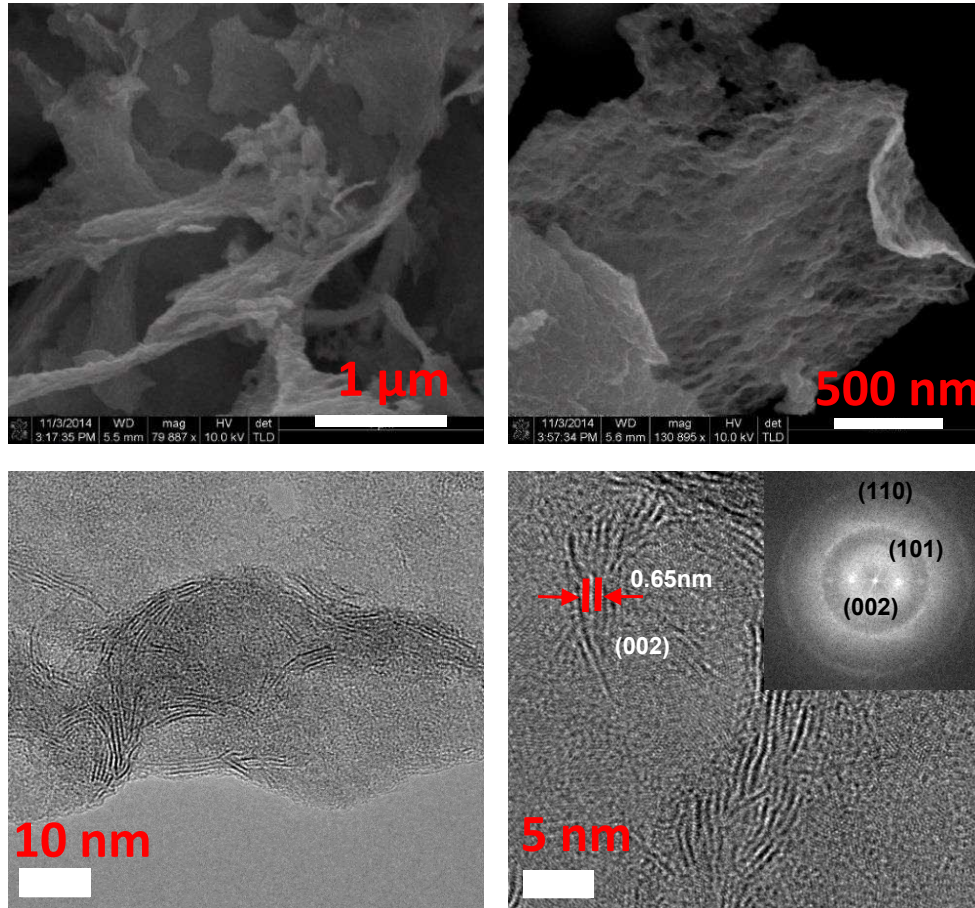


Fig. 4.4 FE-SEM images of MoS₂ sponges at low (top left) and higher magnification (top right). TEM images of MoS₂ sponges at low (bottom left) and high magnification (bottom right) with inset indicating the FFT pattern.

The rectangular shape of the CV curves indicates the capacitive behavior of the MoS₂ electrodes. The CV curves retained their quasi-rectangular shape when the scan rate was increased, which confirmed the excellent reversibility of this electrode material [23, 24]. [29-30] From the CV curves, the specific capacitance of a device (C_m) and a single electrode (C_s) can be calculated using Eqs. (2.3) and (2.5), respectively. The symmetric capacitor showed a device capacitance of 128 A g⁻¹ at a scan rate of 2 mV s⁻¹. For comparison, the single electrode capacitance (C_s) was also calculated using the Eq. (2.5). The highest C_s value obtained for a single MoS₂ sponge electrode was 510 A g⁻¹ at a scan rate of 2 mV s⁻¹ using a two electrode configuration. This value is superior to that previously reported by Ramadoss et al. (403 A g⁻¹ at 1 mV s⁻¹ using a three-electrode configuration) [16]. When the scan rate was increased to 5 mV s⁻¹, the single electrode C_s dropped to 411 A g⁻¹, although this is still much higher than that reported by Acerce et al. (250 A g⁻¹ at 5 mV s⁻¹ using a three-electrode configuration) [15]. In general, supercapacitor measurement using three-electrode systems shows exaggerated capacitances of the electrode material (more than twice the actual values), and additionally it does not accurately mimic the performance of a practical device [6]. In our case, we have calculated the C_s by constructing a symmetric two-electrode cell; therefore, the values are more realistic and closer to those likely to be seen in real world applications.

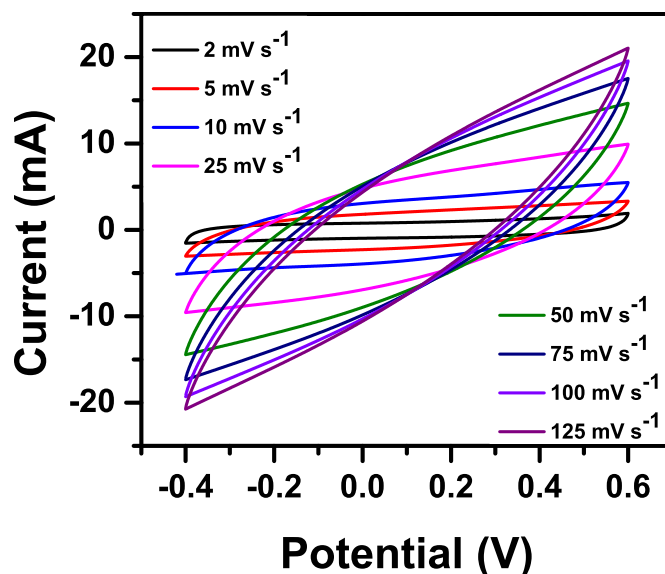


Fig. 4.5 Cyclic voltammograms of MoS₂ sponge electrode-based symmetric cells measured at various scan rates from 2 mV s⁻¹ to 125 mV s⁻¹.

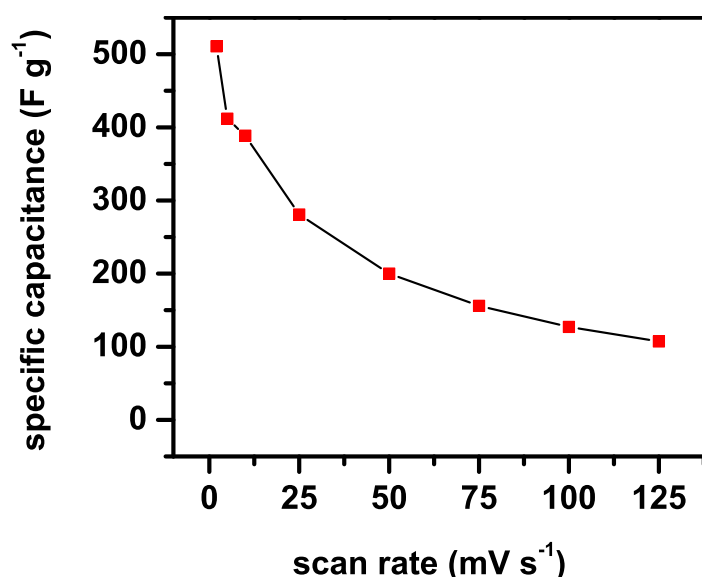


Fig. 4.6 Specific gravimetric capacitance of a single electrode versus scan rate.

The high specific capacitance of the as-synthesized material could be due to the following: (i) the graphene-like 2-D structure exhibited by MoS₂ allowing more effective intercalation of cations between the layers, (ii) better electrical conductivity of MoS₂ when compared to its corresponding oxides leading to lower charge-transfer resistance and thereby improved charge storage behavior, and/or (iii) the high surface area originating from the freeze-drying process also enhanced the double layer capacitance of the electrode material. Figure 4.6 shows the effect of scan rate on C_s, and it clearly shows that increasing the scan rate led to a gradual decrease in C_s, possibly due to restricted mass transport of protons from the electrolyte to the electrode surface causing limited ion adsorption-desorption processes at the interface of the electrode and electrolyte [25–27]. However, even at a high scan rate of 125 mV s⁻¹, a C_s of approximately 107 A g⁻¹ was observed. Such a high capacitance may be ascribed to the higher ionic

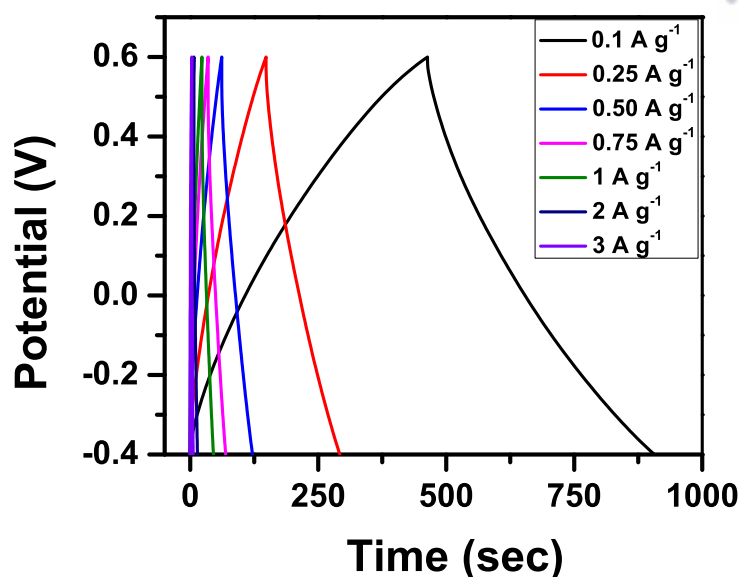


Fig. 4.7 Charge-discharge curves of MoS₂ sponge electrode-based symmetric cells measured at different current densities.

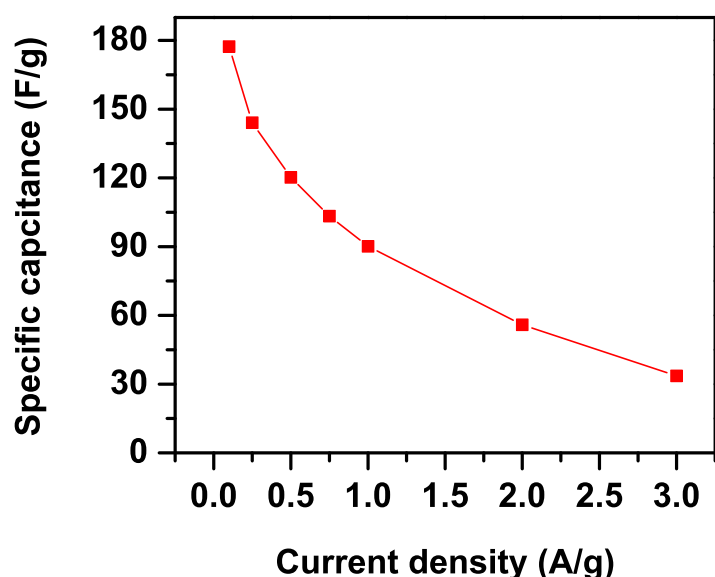


Fig. 4.8 Specific gravimetric capacitance of a single electrode at various current densities (0.01 A g⁻¹ to 3 A g⁻¹), derived from charge-discharge measurements.

diffusivity of MoS₂ sheets, which have large S²⁻ ions that induce large anionic polarizability [15, 28].

The galvanostatic charge-discharge (CD) curves of MoS₂ sponge electrodes measured at various current densities (0.1–3 A g⁻¹) are shown in Fig. 4.7. The CD curves show nearly triangular shapes that indicate almost ideal capacitive behavior [15]. At a low current density of 0.1 A g⁻¹, a single electrode C_s of approximately 177.3 A g⁻¹ was calculated using Eqs. (2.4) and (2.5), while on increasing the current density to the industrial standard of 1 A g⁻¹, a C_s of 90 A g⁻¹ was retained. The relationship between the calculated specific capacitance (C_s) and current density is plotted in Fig. 4.8.

Fig. 4.9 displays the Ragone plot of the symmetric supercapacitor device, whereas the energy density and power density can be calculated using Eqs. (2.11) and (2.12), respectively. The symmetric device

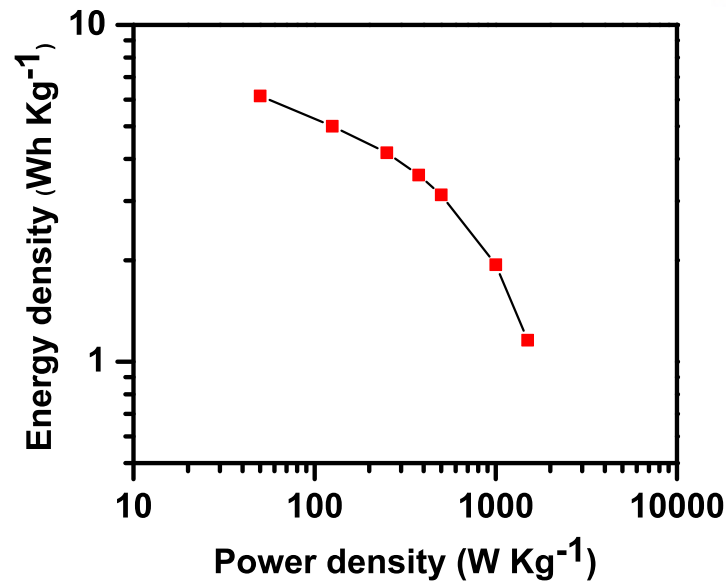


Fig. 4.9 Ragone plot of a symmetric device showing the gravimetric energy and power densities.

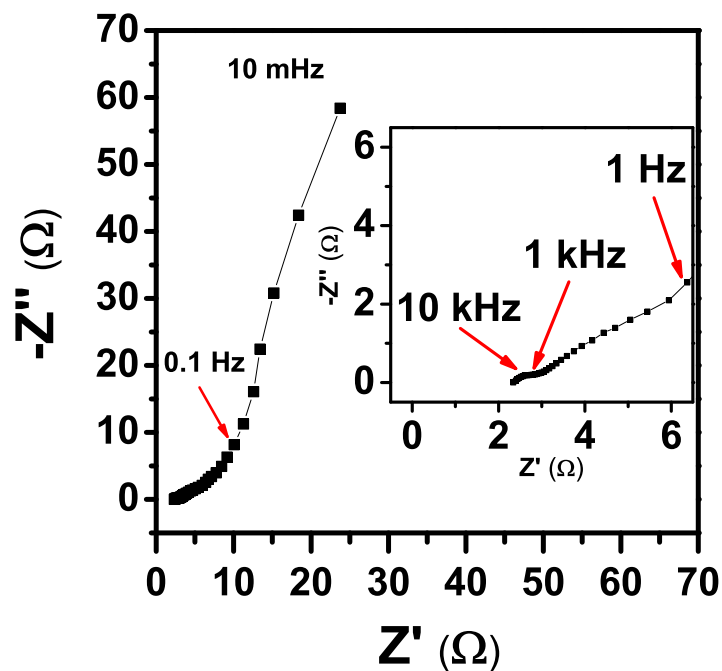


Fig. 4.10 Nyquist plot from the EIS measurements (the inset shows the high frequency region).

delivered an energy density of 6.15 Wh kg^{-1} (equivalent to 44.3 A g^{-1} for the SC) at a power density of 50 W kg^{-1} , and it retained half of its energy density (3.12 Wh kg^{-1}) at a power density of 500 W kg^{-1} . At a very high power density of 1.5 kW kg^{-1} , the energy density dropped to 1.15 Wh kg^{-1} , which could be due to the fast reversible redox reaction of protons occurring only at the surface of the MoS_2 film, while the interior of the MoS_2 film being inaccessible at a higher current densities.

Fig. 4.10 shows the electrochemical impedance analysis of the symmetric device. The x-intercept of the Nyquist plot shows the device had a low series resistance ($R_s = 2.33 \text{ } \Omega$), while the small semicircle-arc observed in the high frequency region ($R_{ct} = 0.7 \text{ } \Omega$) corresponds to the parallel combination of charge-

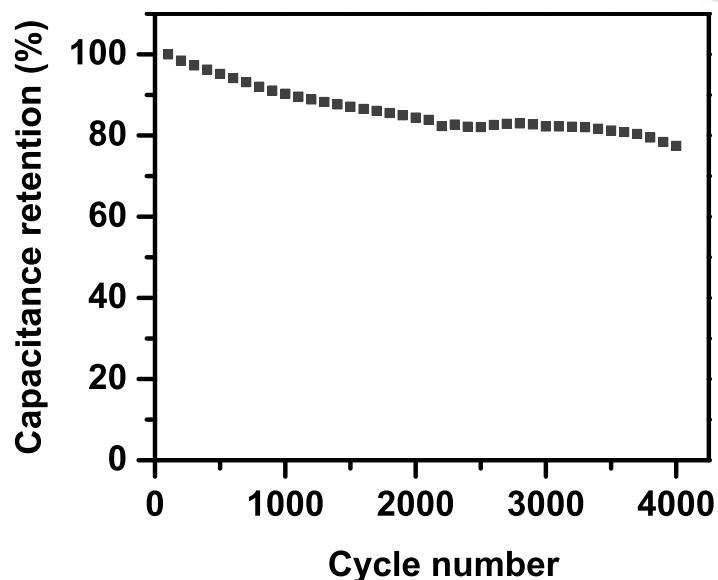


Fig. 4.11 Long term cycling stability of the device at a current density of 2 A g^{-1} .

transfer resistance with EDLC. In the mid-frequency range, an almost 45° slope indicating Warburg-type resistance can be observed for a short region, which infers a short proton diffusion path from the electrolyte to the electrode surface. In the low-frequency region, an almost perpendicular straight line is observed that indicates ideal capacitive behavior of the device [29]. Long-term stability is one of the important criteria in devices for practical applications. Fig. 4.11 shows the capacitance retention against cycle number of the device derived from long-term charge-discharge measurements at a current density of 2 A g^{-1} . The capacitance decreased gradually up to 2000 cycles, leveling out between 2000 to 4000 cycles, with approximately 80% of the initial capacitance retained.

4.4 Summary

In summary, we have demonstrated that a freeze-dried MoS_2 sponge electrode showed high specific capacitance due to the high surface area, which led to better charge storage behavior via electrochemical double layer capacitance. The as-fabricated symmetric device showed a high energy density of approximately 6.15 Wh kg^{-1} , as well as long-term stability over 4000 cycles, indicating that freeze-dried MoS_2 sponge electrodes could be a promising candidate for next-generation energy storage devices.

References

- [1] Das, S., Robinson, J.A., Dubey, M., Terrones, H., Terrones, M., Beyond graphene: Progress in novel two-dimensional materials and van der waals solids, *Annual Review of Materials Research* 2015, 45 (1), 1–27. doi:[10.1146/annurev-matsci-070214-021034](https://doi.org/10.1146/annurev-matsci-070214-021034).
- [2] Rao, C.N.R., Maitra, U., Inorganic graphene analogs, *Annual Review of Materials Research* 2015, 45 (1), 29–62. doi:[10.1146/annurev-matsci-070214-021141](https://doi.org/10.1146/annurev-matsci-070214-021141).

- [3] Bose, R., Balasingam, S.K., Shin, S., Jin, Z., Kwon, D.H., Jun, Y., Min, Y.S., Importance of hydrophilic pretreatment in the hydrothermal growth of amorphous molybdenum sulfide for hydrogen evolution catalysis, *Langmuir* 2015, 31 (18), 5220–5227. doi:[10.1021/acs.langmuir.5b00205](https://doi.org/10.1021/acs.langmuir.5b00205).
- [4] Soon, J.M., Loh, K.P., Electrochemical double-layer capacitance of MoS₂ nanowall films, *Electrochemical and Solid-State Letters* 2007, 10 (11), 250–254. doi:[10.1149/1.2778851](https://doi.org/10.1149/1.2778851).
- [5] Sun, G., Zhang, X., Lin, R., Yang, J., Zhang, H., Chen, P., Hybrid fibers made of molybdenum disulfide, reduced graphene oxide, and multi-walled carbon nanotubes for solid-state, flexible, asymmetric supercapacitors, *Angewandte Chemie International Edition* 2015, 54 (15), 4651–4656. doi:[10.1002/anie.201411533](https://doi.org/10.1002/anie.201411533).
- [6] Bissett, M.A., Kinloch, I.A., Dryfe, R.A.W., Characterization of MoS₂-graphene composites for high-performance coin cell supercapacitors, *ACS Applied Materials & Interfaces* 2015, 7 (31), 17388–17398. doi:[10.1021/acsami.5b04672](https://doi.org/10.1021/acsami.5b04672).
- [7] Winchester, A., Ghosh, S., Feng, S., Elias, A.L., Mallouk, T., Terrones, M., Talapatra, S., Electrochemical characterization of liquid phase exfoliated two-dimensional layers of molybdenum disulfide, *ACS Applied Materials & Interfaces* 2014, 6 (3), 2125–2130. doi:[10.1021/am4051316](https://doi.org/10.1021/am4051316).
- [8] Da Silveira Firmiano, E.G., Rabelo, A.C., Dalmaschio, C.J., Pinheiro, A.N., Pereira, E.C., Schreiner, W.H., Leite, E.R., Supercapacitor electrodes obtained by directly bonding 2d MoS₂ on reduced graphene oxide, *Advanced Energy Materials* 2014, 4 (6). doi:[10.1002/aenm.201301380](https://doi.org/10.1002/aenm.201301380).
- [9] Tang, H., Wang, J., Yin, H., Zhao, H., Wang, D., Tang, Z., Growth of polypyrrole ultrathin films on mos2 monolayers as high-performance supercapacitor electrodes, *Advanced Materials* 2015, 27 (6), 1117–1123. doi:[10.1002/adma.201404622](https://doi.org/10.1002/adma.201404622).
- [10] Hu, B., Qin, X., Asiri, A.M., Alamry, K.A., Al-Youbi, A.O., Sun, X., Synthesis of porous tubular c/MoS₂ nanocomposites and their application as a novel electrode material for supercapacitors with excellent cycling stability, *Electrochimica Acta* 2013, 100, 24–28. doi:[10.1016/j.electacta.2013.03.133](https://doi.org/10.1016/j.electacta.2013.03.133).
- [11] Huang, K.J., Zhang, J.Z., Shi, G.W., Liu, Y.M., Hydrothermal synthesis of molybdenum disulfide nanosheets as supercapacitors electrode material, *Electrochimica Acta* 2014, 132, 397–403. doi:[10.1016/j.electacta.2014.04.007](https://doi.org/10.1016/j.electacta.2014.04.007).
- [12] Huang, K.J., Wang, L., Liu, Y.J., Wang, H.B., Liu, Y.M., Wang, L.L., Synthesis of polyaniline/2-dimensional graphene analog MoS₂ composites for high-performance supercapacitor, *Electrochimica Acta* 2013, 109, 587–594. doi:[10.1016/j.electacta.2013.07.168](https://doi.org/10.1016/j.electacta.2013.07.168).
- [13] Huang, K.J., Wang, L., Liu, Y.J., Liu, Y.M., Wang, H.B., Gan, T., Wang, L.L., Layered MoS₂-graphene composites for supercapacitor applications with enhanced capacitive performance, *International Journal of Hydrogen Energy* 2013, 38 (32), 14027–14034. doi:[10.1016/j.ijhydene.2013.08.112](https://doi.org/10.1016/j.ijhydene.2013.08.112).

- [14] Zhou, X., Xu, B., Lin, Z., Shu, D., Ma, L., Hydrothermal synthesis of flower-like MoS₂ nanospheres for electrochemical supercapacitors, *Journal of Nanoscience and Nanotechnology* 2014, 14 (9), 7250–7254. doi:[10.1166/jnn.2014.8929](https://doi.org/10.1166/jnn.2014.8929).
- [15] Acerce, M., Voiry, D., Chhowalla, M., Metallic 1t phase MoS₂ nanosheets as supercapacitor electrode materials, *Nature Nanotechnology* 2015, 10 (4), 313–318. doi:[10.1038/nnano.2015.40](https://doi.org/10.1038/nnano.2015.40).
- [16] Ramadoss, A., Kim, T., Kim, G.S., Kim, S.J., Enhanced activity of a hydrothermally synthesized mesoporous MoS₂ nanostructure for high performance supercapacitor applications, *New Journal of Chemistry* 2014, 38 (6), 2379–2385. doi:[10.1039/C3NJ01558K](https://doi.org/10.1039/C3NJ01558K).
- [17] Cao, L., Yang, S., Gao, W., Liu, Z., Gong, Y., Ma, L., Shi, G., Lei, S., Zhang, Y., Zhang, S., Vajtai, R., Ajayan, P.M., Direct laser-patterned micro-supercapacitors from paintable MoS₂ films, *Small* 2013, 9 (17), 2905–2910. doi:[10.1002/sml.201203164](https://doi.org/10.1002/sml.201203164).
- [18] Du, G., Guo, Z., Wang, S., Zeng, R., Chen, Z., Liu, H., Superior stability and high capacity of restacked molybdenum disulfide as anode material for lithium ion batteries, *Chemical Communications* 2010, 46 (7), 1106–1108. doi:[10.1039/B920277C](https://doi.org/10.1039/B920277C).
- [19] Rao, C.N.R., Gopalakrishnan, K., Maitra, U., Comparative study of potential applications of graphene, MoS₂, and other two-dimensional materials in energy devices, sensors, and related areas, *ACS Applied Materials & Interfaces* 2015, 7 (15), 7809–7832. doi:[10.1021/am509096x](https://doi.org/10.1021/am509096x).
- [20] Chia, X., Eng, A.Y.S., Ambrosi, A., Tan, S.M., Pumera, M., Electrochemistry of nanostructured layered transition-metal dichalcogenides, *Chemical Reviews* 2015, 115 (21), 11941–11966. doi:[10.1021/acs.chemrev.5b00287](https://doi.org/10.1021/acs.chemrev.5b00287).
- [21] Li, X.L., Ge, J.P., Li, Y.D., Atmospheric pressure chemical vapor deposition: An alternative route to large-scale MoS₂ and WS₂ inorganic fullerene-like nanostructures and nanoflowers, *Chemistry - A European Journal* 2004, 10 (23), 6163–6171. doi:[10.1002/chem.200400451](https://doi.org/10.1002/chem.200400451).
- [22] Yang, J., Voiry, D., Ahn, S.J., Kang, D., Kim, A.Y., Chhowalla, M., Shin, H.S., Two-dimensional hybrid nanosheets of tungsten disulfide and reduced graphene oxide as catalysts for enhanced hydrogen evolution, *Angewandte Chemie International Edition* 2013, 52 (51), 13751–13754. doi:[10.1002/anie.201307475](https://doi.org/10.1002/anie.201307475).
- [23] Ramadoss, A., Kim, S.J., Improved activity of a graphene - TiO₂ hybrid electrode in an electrochemical supercapacitor, *Carbon* 2013, 63, 434–445. doi:[10.1016/j.carbon.2013.07.006](https://doi.org/10.1016/j.carbon.2013.07.006).
- [24] Xu, J., Gao, Q., Zhang, Y., Tan, Y., Tian, W., Zhu, L., Jiang, L., Preparing two-dimensional microporous carbon from pistachio nutshell with high areal capacitance as supercapacitor materials, *Scientific Reports* 2014, 4, 5545. doi:[10.1038/srep05545](https://doi.org/10.1038/srep05545).
- [25] Chen, W., Rakhi, R.B., Alshareef, H.N., High energy density supercapacitors using macroporous kitchen sponges, *Journal of Materials Chemistry* 2012, 22 (29), 14394–14402. doi:[10.1039/C2JM32030D](https://doi.org/10.1039/C2JM32030D).

- [26] Li, H.B., Yu, M.H., Wang, F.X., Liu, P., Liang, Y., Xiao, J., Wang, C.X., Tong, Y.X., Yang, G.W., Amorphous nickel hydroxide nanospheres with ultrahigh capacitance and energy density as electrochemical pseudocapacitor materials, *Nature Communications* 2013, 4, 1894. doi:[10.1038/ncomms2932](https://doi.org/10.1038/ncomms2932).
- [27] Mai, L., Li, H., Zhao, Y., Xu, L., Xu, X., Luo, Y., Zhang, Z., Ke, W., Niu, C., Zhang, Q., Fast ionic diffusion-enabled nanoflake electrode by spontaneous electrochemical pre-intercalation for high-performance supercapacitor, *Scientific Reports* 2013, 3. doi:[10.1038/srep01718](https://doi.org/10.1038/srep01718).
- [28] Zheng, N., Bu, X., Feng, P., Synthetic design of crystalline inorganic chalcogenides exhibiting fast-ion conductivity, *Nature* 2003, 426 (6965), 428–432. doi:[10.1038/nature02159](https://doi.org/10.1038/nature02159). 10.1038/nature02159.
- [29] Balasingam, S.K., Lee, J.S., Jun, Y., Few-layered MoSe₂ nanosheets as an advanced electrode material for supercapacitors, *Dalton Transactions* 2015, 44 (35), 15491–15498. doi:[10.1039/C5DT01985K](https://doi.org/10.1039/C5DT01985K).

Amorphous MoS_x Thin-layer Coated Carbon Fiber Paper

5.1 Introduction

Molybdenum disulfide (MoS_2), a class of TMDCs, are one of the most studied materials because of the following advantages: excellent electrocatalytic activity (next to noble metals, as evidenced by the volcano curve), 2D layered crystal structure that facilitates ion intercalation (Li^+ or other alkali metal ion), high surface area, and higher electronic conductivity than that of transition metal oxides (TMOs) [1]. Because of these advantages, MoS_2 has been utilized for various electrochemical applications such as sensors, hydrogen evolution catalysts, solar cells, and lithium/sodium ion batteries [2, 3]. Until 2007 when the capacitive behavior of MoS_2 nanowall films was first reported by Loh's group, researchers did not think about using TMDCs for application in supercapacitors [4]. However, from 2007 onward, a considerable number of articles have been published on MoS_2 and its composite (MoS_2 /conducting polymer and MoS_2 /carbon)-based electrodes for supercapacitor applications [5]. Most of the MoS_2 synthesis methods are high-temperature solution-based chemical methods or involve top-down exfoliation of bulk MoS_2 crystals, forming highly crystalline MoS_2 materials [5, 6]. In general, amorphous phase of pseudocapacitive materials with low crystallinity show higher specific capacitance (C_s) than their highly crystalline counterparts [7]. This phenomenon has been proved by a systematic study on amorphous and crystalline NiO column structure and its surface and bulk contribution to the C_s value [8]. Furthermore, Lu et al. experimentally verified that the bulk contribution of amorphous NiO electrode was three times higher than that of its crystalline phase. Very recently, Zhang and co-workers synthesized an amorphous MoS_2 shell over the crystalline Ni_3S_4 core ($\text{Ni}_3\text{S}_4@ \text{MoS}_2$ core-shell structure), which showed better capacitive performance than pure Ni_3S_4 [9]. In the present communication, we synthesized amorphous MoS_x on a highly conductive 3-D carbon fiber paper network (CFP/a- MoS_x). To the best of our knowledge, this is the first report on using CFP/a- MoS_x binder-free electrode material for supercapacitor applications.

Here in this chapter, the facile hydrothermal method was adopted to deposit amorphous MoS_x thin layer on the carbon fiber paper. The carbon fiber paper is hydrophobic. Hence, prior to conduct the hydrothermal growth of MoS_x , carbon fiber paper is pretreated with oxygen plasma to induce the hydrophilicity [2].

5.2 Experimental

5.2.1 Synthesis of amorphous-MoS_x on carbon fiber paper

Molybdic acid, (MAA, H₂MoO₄) and thioacetamide (TAA, CH₃CSNH₂) were purchased from Sigma-Aldrich Corporation. An exactly 0.225 gram of TAA and 0.121 g of MAA were accurately weighed and then dissolved into 80 ml of deionized (DI) water, with constant stirring for 15 min in order to achieve complete dissolution. The carbon fiber paper (CFP, Toray, TGP-H-120) substrate is basically hydrophobic in nature due to its sp² hybridization of carbon atoms present in the graphitic structure. In a typical hydrothermal synthesis, wettability of CFP is an important criterion in order to achieve the uniform deposition (with good adhesion) of MoS_x onto the substrate. To induce the hydrophilicity in CFP, a small piece of CFP is placed inside the plasma chamber followed by activation using oxygen plasma with a power of 18 W for 15 min. After plasma cleaning, the CFP is immediately transferred into a Teflon-lined autoclave followed by the transfer of TAA and MAA mixed precursor solution into the same autoclave and then sealed tightly. The autoclave was then placed inside an electric oven and maintained the reaction temperature at 200 °C for 24 h. Once the hydrothermal reaction was completed, the autoclave was retained inside the electric oven until it cooled down naturally to room temperature. The resulting amorphous MoS_x coated CFP was taken out and washed with DI water for several times to remove the loose MoS_x deposits adsorbed on the substrate. After rinsing, a-MoS_x deposited CFP (CFP/a-MoS_x) was dried in an electric oven at 40 °C for 12 hrs.

5.2.2 Material characterization

Surface morphology of the bare CFP and amorphous MoS_x coated CFP (CFP/a-MoS_x) was examined using scanning electron microscopy (NanoSEM, S-3400N). High-resolution transmission electron microscopy (HR-TEM, FEI, Talos F200X) was used to examine the cross-sectional image, microstructure, thickness and amorphous nature of MoS_x. A thin slice of TEM sample was prepared using Scanning electron microscopy equipped with focused ion beam (FEI, Quanta 3D), after deposition of thin layer of epoxy/Pt on the surface of MoS_x. The chemical composition and oxidation state of elements were analyzed using X-ray photoelectron spectroscopy (XPS, Thermo Fisher, UK). The amorphous nature of MoS_x was examined using X-ray diffraction (XRD, Bruker-D8 ADVANCE) using Cu Kα emission ($\lambda = 1.5406 \text{ \AA}$) with a step-size of 0.02° and the Raman spectroscopy (WITech, alpha300R) using 532 nm laser excitation, after calibrating the Raman shift with a silicon reference at 521 cm⁻¹.

5.3 Results and Discussion

5.3.1 Physico-chemical analysis

The as-synthesized CFP/a-MoS_x electrode was subjected to X-ray diffraction (XRD) and Raman spectroscopic analysis. The results show the absence of any characteristic peaks of MoS₂; hence, it can be inferred that the as-deposited material is amorphous (see the Fig. C.1 and Fig. C.2 in Appendix C). Figure. 5.1 shows the scanning electron microscopic (SEM) images of bare CFP (Fig. 5.1a and 5.1b)

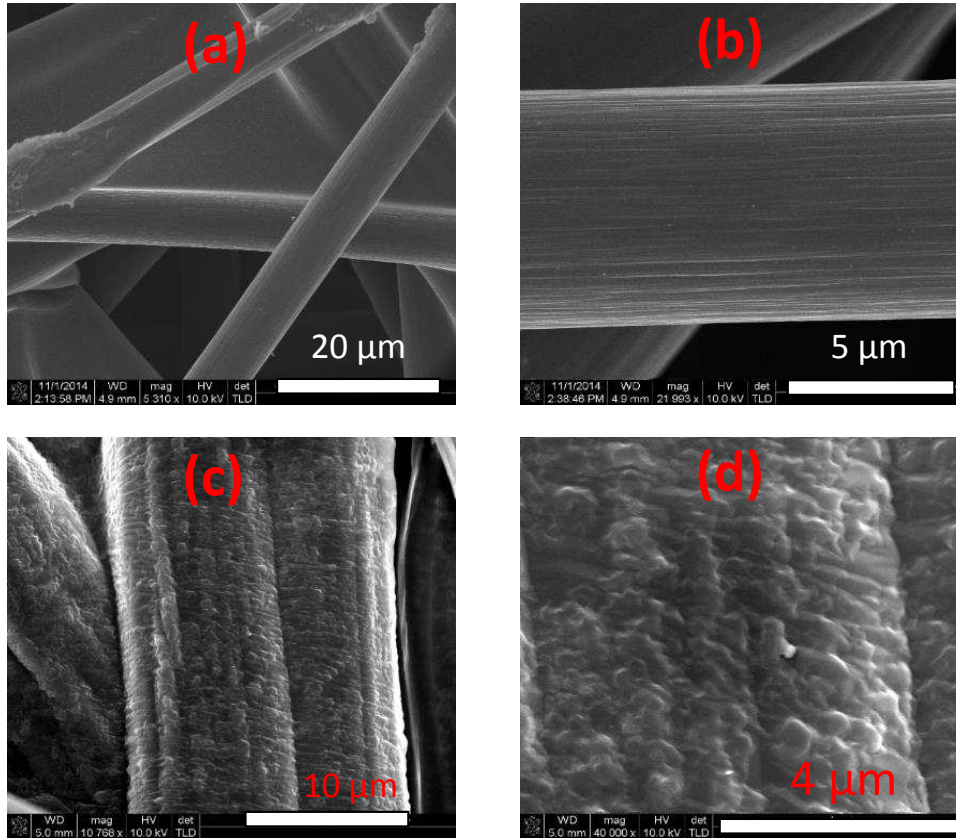


Fig. 5.1 SEM images of bare CFP at (a) low magnification and (b) high magnification, and SEM images of CFP/a-MoS_x at (c) low magnification and (d) high magnification.

and those of MoS_x coated-CFP (Fig. 5.1c and 5.1d), both at low and high magnifications. It is clearly evident that the high-magnification SEM image (Fig. 5.1d) shows uniformly coated MoS_x nanosheets on the 3D-CFP network. To examine the thickness of the MoS_x coating, a small portion of the sample was sliced using a focused ion beam equipped with an SEM instrument (FIB-SEM).

To further confirm the structural information and thickness, the as-prepared thin slice of CFP/a-MoS_x was examined using high-resolution transmission electron microscopy (HR-TEM). Figure 5.2a shows the high-magnification TEM image of CFP/a-MoS_x, which shows that the average thickness of the MoS_x thin film was around (20±2) nm. The absence of clear lattice fringes and the corresponding FFT pattern (inset of Fig. 5.2a) confirms the amorphous nature of MoS_x, which is in agreement with the XRD and Raman measurements. Figure 5.2b shows the STEM image of the CFP/a-MoS_x and the Fig. 5.2c shows the corresponding energy dispersive spectrum (EDS) of a-MoS_x as marked in the small (red square) region of Fig. 5.2b. From the EDS spectrum, the presence of molybdenum and sulfur has been confirmed. The detection of copper may be due to TEM grid and gallium impurity originates from the FIB-slicing of TEM sample preparation. Figure 5.3 shows the low magnification STEM image of elemental mapping of CFP/a-MoS_x and the large area elemental mapping of corresponding elements.

The chemical composition and oxidation state of the elements were analyzed using X-ray photoelectron spectroscopy (XPS). Fig. 5.4a shows the Mo 3d spectra of amorphous MoS_x. The doublets of 3d orbital clearly resolved into two different peaks at 3d_{5/2} and 3d_{3/2} centered at 228.99 and 232.41 eV, respectively,

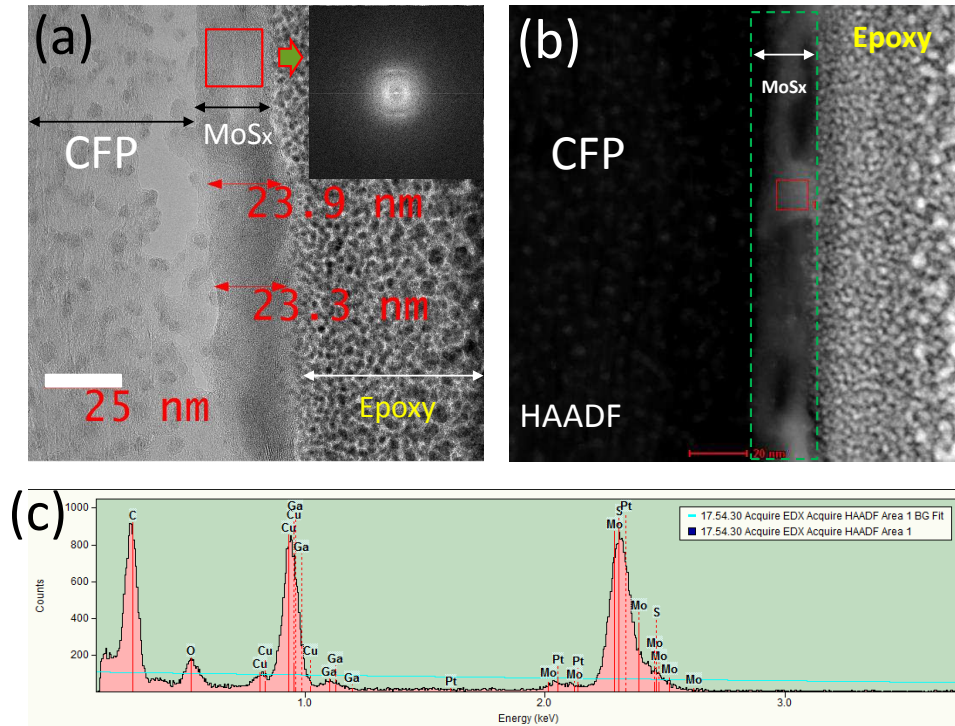


Fig. 5.2 (a) HR-TEM cross-sectional image of CFP/a-MoS_x with inset displaying the FFT pattern; (b) HAADF-STEM cross-sectional image of CFP/a-MoS_x where the area within green dotted rectangle indicates the thin layer of MoS_x; and (c) a small area EDS spectrum of MoS_x taken at the red highlighted square in Fig. (b).

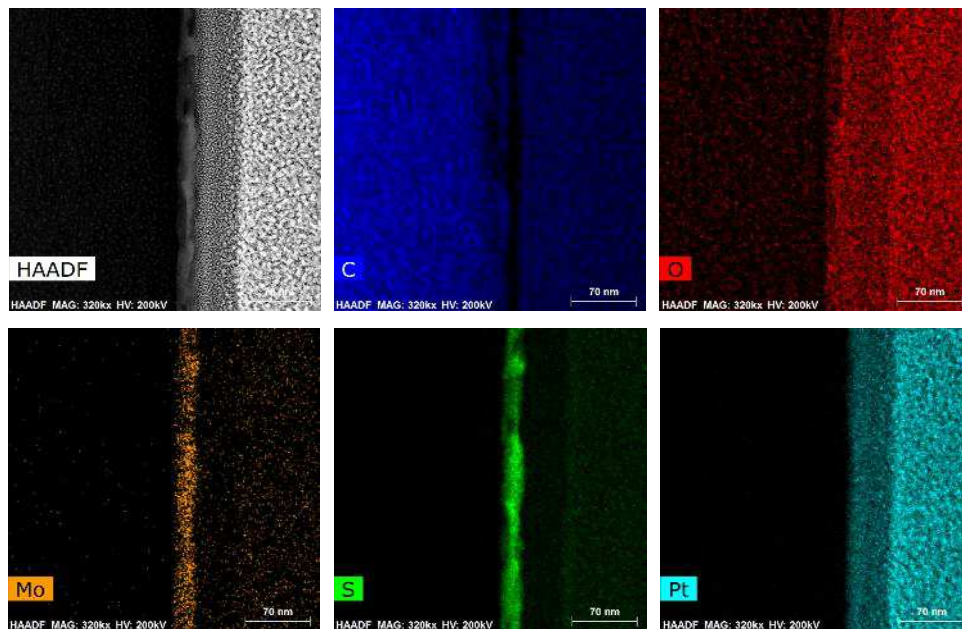


Fig. 5.3 STEM image and elemental maps of CFP/a-MoS_x. Reprinted with permission from [2]. Copyright 2015 American Chemical Society.

which confirms the +4 oxidation state of Mo (i.e., Mo(IV)). The sulfur 2s orbital appears at the binding energy of 226.43 eV and a small hump of a Mo⁶⁺ peak appears at a higher binding energy of 235.8 eV;

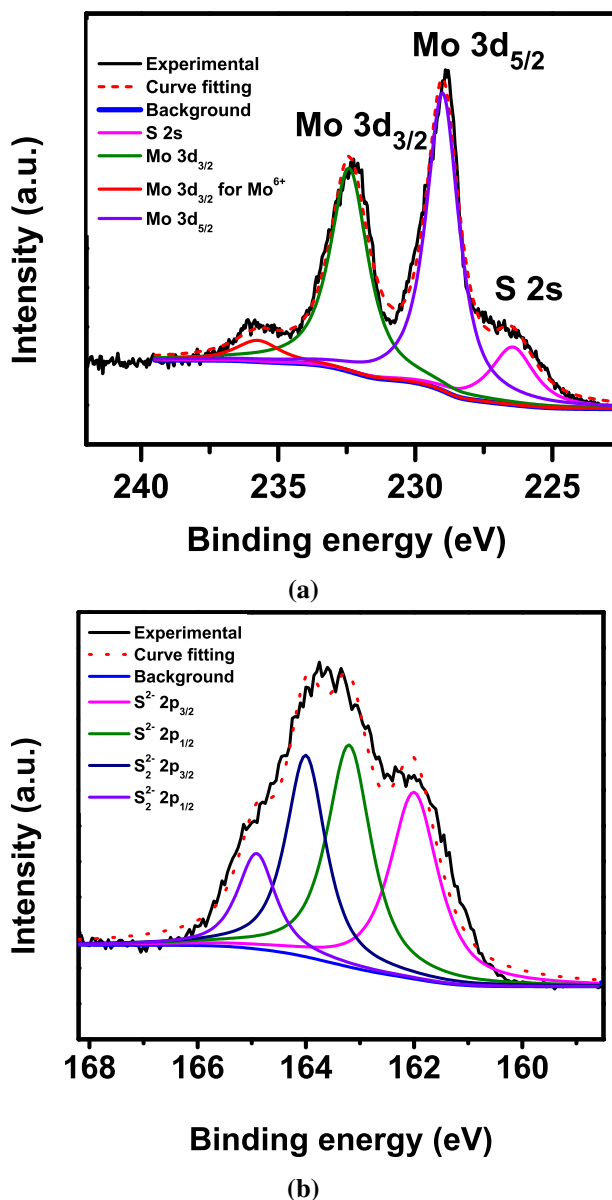


Fig. 5.4 High resolution XPS spectra of (a) Mo 3d, and (b) S 2p regions of a-MoS_x.

the latter may have formed because of the formation of oxides during the sample-preparation process [10]. Because of the amorphous nature of MoS_x, an unresolved broad hump of a sulfur 2p peak is also observed (Fig. 5.4b). From the atomic concentration table, the sulfur to molybdenum stoichiometric ratio was estimated at around 2.17. The excess sulfur present in the compound may be owing to the formation of MoS₃(Mo⁴⁺[S²⁻][S₂²⁻]), rather than MoS₂. Upon deconvolution, the doublet of S²⁻ appears at lower binding energies and that of S₂²⁻ at higher binding energies.

5.3.2 Electrochemical performance of symmetric cells

The electrochemical properties of the CFP/a-MoS_x binder-free electrode material were investigated for supercapacitor applications by using a symmetric two-electrode cell with aqueous 0.5 M sulfuric acid electrolyte. Fig. 5.5 represents the cyclic voltammetry (CV) curves of the CFP/a-MoS_x symmetric cell

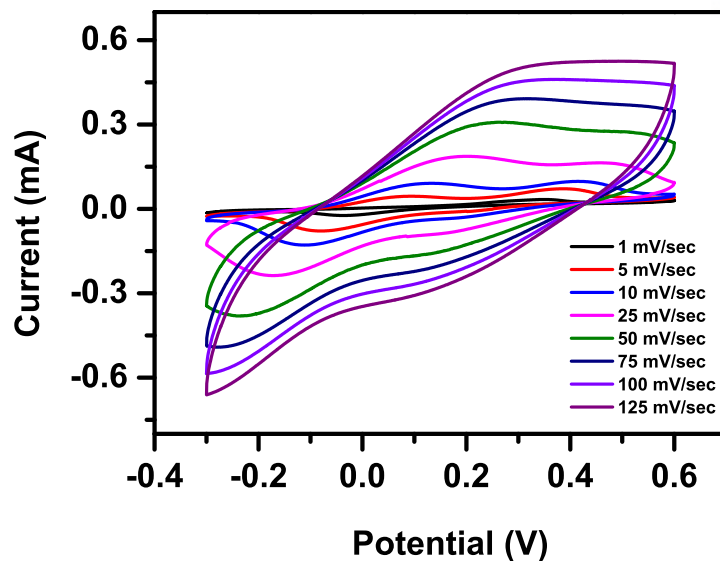


Fig. 5.5 CV curves of CFP/a-MoS_x at various scan rates ranging from 1 mV s⁻¹ to 125 mV s⁻¹.

at various scan rates in the potential range varying from -0.3 to 0.6 V. At low scan rates, two pairs of prominent redox peaks can be clearly seen, which are attributed to the redox reaction of Mo atoms: Mo \longleftrightarrow Mo(IV) \longleftrightarrow Mo(VI) [9]. When the scan rate is increased, an obvious shift was seen in the redox peaks. Broad redox peaks are observed even at a higher scan rate, which confirmed that a predominant charge-storage reaction occurs via a redox reaction (pseudocapacitance). Apart from pseudocapacitance, non-Faradaic processes owing to the adsorption and desorption of protons (or in some cases, alkali metal ions) on the surface of MoS₂, which involves the double layer (capacitance) charge-storage mechanism, has also been reported [4, 11–15]. In some cases, the Faradaic process is only observable at a very lower scan rate; when the scan rate is increased due to the kinetic limitation of cation diffusion, the non-Faradaic process (EDLC behavior) becomes dominant [4, 12]. In our study, however, even at a higher scan rate of 125 mV s⁻¹, broad redox peaks were observed with distorted rectangular CV curves, which confirmed that both pseudocapacitance and EDLC-type charge-storage mechanism were involved.

Equations (2.6) and (2.7) were used to measure the cell capacitance using CV and CD curves, respectively. The corresponding areal specific capacitance of a cell (C_m), and a single electrode (C_s), were calculated using Eqs. (2.8) and (2.10), respectively. The relationship between the scan rates and C_s is correlated (Fig. 5.6). When the scan rate is increased gradually from 1 to 125 mV s⁻¹, the C_s value decreases, probably owing to the insufficient time available for the insertion/extraction of protons into the interior (bulk) of the electrode [16]. Based on this observation, it can be inferred that the electrochemical reaction kinetics is controlled by the protonic diffusion process at higher scan rates. When the scan rate was 1 mV s⁻¹, a single electrode showed a C_s value of 83.9 mF cm⁻² and the device showed a C_m value of 41.96 mF cm⁻². The C_s value obtained in our study using two-electrode configuration is still higher than that reported by Soon et al. (70 mF cm⁻² @ 1 mV s⁻¹, obtained using three-electrode configuration) [4]. When the scan rate is increased to 5 mV s⁻¹, C_m decreased to 20.4 mF cm⁻²; however, the C_m value obtained using our cell is much higher than that reported by a recent work on exfoliated MoS₂ (1.83 mF cm⁻²) and graphene-exfoliated MoS₂ composite (4.29 mF cm⁻²) based symmetric devices at the same scan rate [15]. On further increasing the scan rate to 10 mV s⁻¹, the corresponding

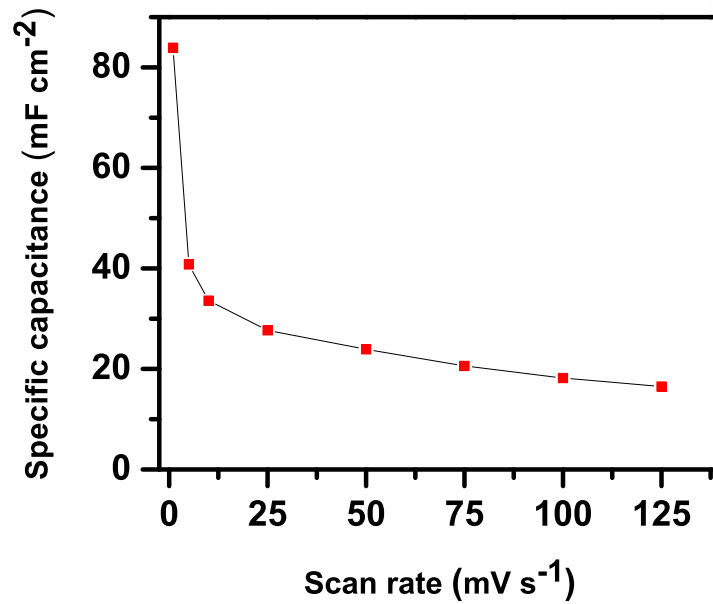


Fig. 5.6 Relationship between specific capacitance of electrode and scan rate.

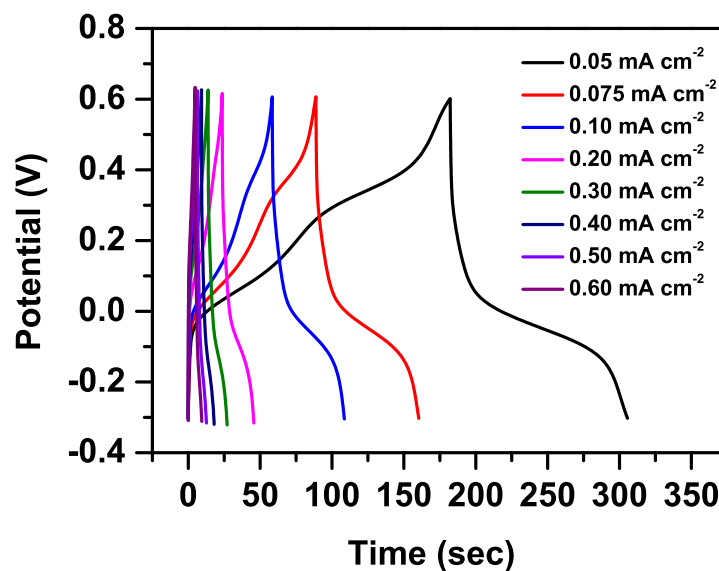


Fig. 5.7 Charge-discharge curves of CFP/a-MoS_x at current densities.

C_s value dropped to 33.6 mF cm^{-2} and the C_m value decreased to 16.8 mF cm^{-2} . However, the C_m value obtained in the present work is eight times higher than that in a previous report on exfoliated-MoS₂ (2 mF cm^{-2} @ 10 mV s^{-1}) and 33 times higher (0.5 mF cm^{-2} @ 10 mV s^{-1}) than that obtained with bulk MoS₂-based symmetric devices [14].

To further evaluate the electrochemical performance of the CFP/a-MoS_x electrode material, galvanostatic charge-discharge measurements were carried out for the symmetric device at current densities of $0.05 - 0.6 \text{ mA cm}^{-2}$ (Fig. 5.7). The nonlinear shape of the discharge curves further confirmed the pseudocapacitive charge-storage behavior. The relationship between C_s and the various current densities is shown in Fig. 5.8. When the discharge rate was 0.3 mA cm^{-2} , the corresponding C_s was 8.76 mA cm^{-2} , which is more than five times that of exfoliated MoS₂ (1.65 mF cm^{-2} @ 0.25 mA cm^{-2}) [15]. The

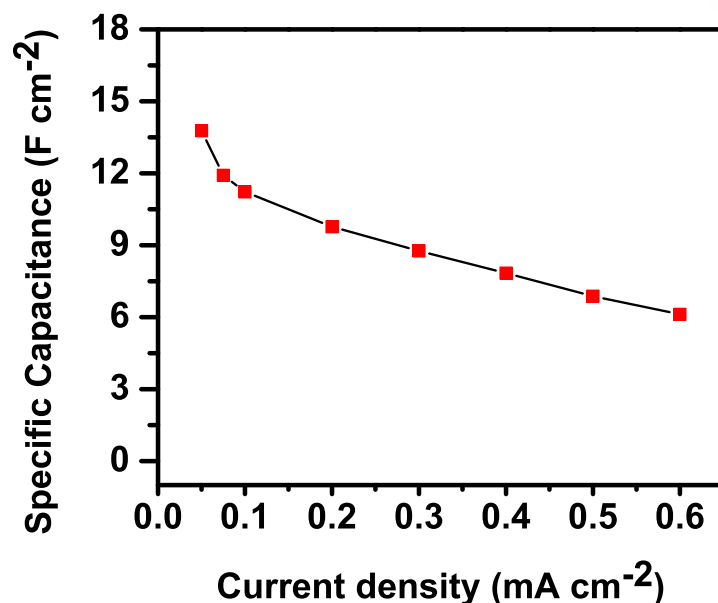


Fig. 5.8 Relationship between specific capacitance of electrode and current densities.

high specific capacitance of the CFP/a-MoS_x material may be due to the following reasons: (i) High surface area of the 3D porous carbon fiber network with good electrical conductivity that increases the electron-transfer reaction rate, even though as-synthesized MoS_x is poorly crystalline. (ii) A thin amorphous MoS_x film (thickness is found to be approximately (22±3) nm as determined from the TEM measurements) made of high-density grain boundaries with fine grains that act as diffusion channels for a more efficient intercalation of protons, which leads to an effective utilization of bulk electrode materials when compared to their crystalline counterparts [7].

The electrochemical impedance spectroscopy is one of the ideal tools to investigate the charge transfer mechanism at the electrode-electrolyte interface. In the impedance spectrum (Fig. 5.9), a high-frequency intercept on the x-axis represents electrochemical series resistance (ESR) of the symmetric device. The semicircle arc at the high- to medium-frequency range represents the charge transfer resistance (R_{ct}), which is determined to be 0.5 Ω. An almost 90° straight line (perpendicular to x-axis) is observed at the medium-to-low frequency region, which represents the capacitive behavior of the device.

The long-term cyclability is one of the key criteria for the real-time application of the device for commercial use. The symmetric capacitor has been tested to investigate the continuous long-term charge-discharge process at a current of 0.3 mA cm⁻². The C_s value in the first cycle was around 8.46 mF cm⁻², which increased to 50.4 mF cm⁻² at the 4750th cycle. Most of the previous reports on long-term stability of pseudocapacitive materials, including MoS₂ electrode materials, showed generally either decrease in capacitance retention or a stable value over many cycles [9, 11–14, 17, 18]. In contrast, the capacitance retention of CFP/a-MoS_x synthesized in our study continuously increased up to 600% for 4750 cycles (Fig. 5.10). This type of increase in capacitance is rarely observed in binder-free graphene-based supercapacitors (using KCl electrolyte) because of the “electroactivation” of electrode materials via continuous (K⁺) ion intercalation/deintercalation, which leads to partial re-exfoliation process [19–21]. Very recently, Bissett et al. also observed the same trend on exfoliated MoS₂

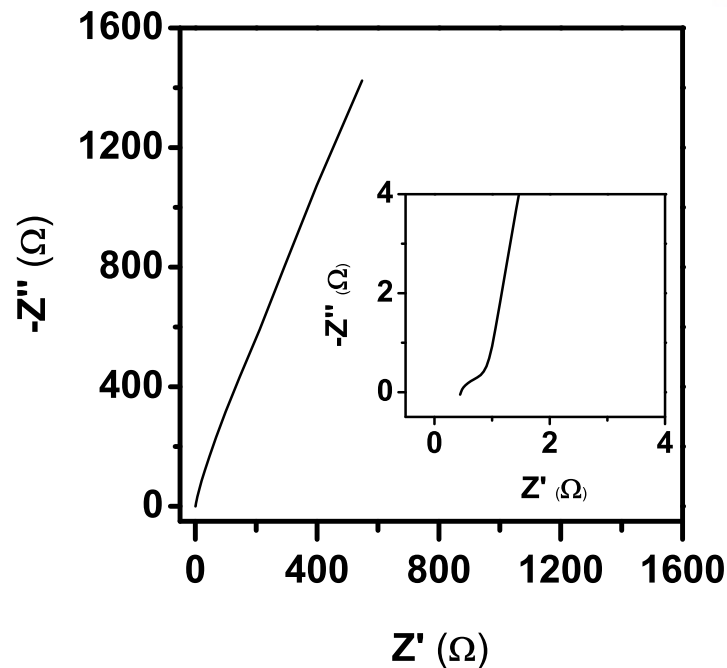


Fig. 5.9 EIS spectrum of the symmetric supercapacitor with inset showing the high-frequency region.

thin-film-based symmetric capacitors (using Na_2SO_4 electrolyte), wherein the capacitance retention increased up to 800% over the first 3000 cycles [15]. The authors investigated the charge storage mechanism by CV analysis before and after long-term cycling. Before cycling, the CV curves show the EDLC-type charge-storage behavior; however, after long-term cycling for over 10,000 cycles, the shape of the post-CV curve distorted with enhanced current density. Hence, the authors concluded that the electrochemical charge-storage mechanism changes from EDLC to pseudocapacitive nature because of the continuous ion intercalation/deintercalation process. Also, they proposed a mechanism involving continuous intercalation/deintercalation of relatively large Na^+ ions over a long cycling process that further increased the active surface area by partial re-exfoliation of MoS_2 layers, and hence, led to enhanced current density value in post-CV curves. In our case, energy storage occurs predominantly by pseudocapacitance (from the first cycle to 4750th cycle and even for a high scan rate CV curves); hence, clear redox peaks are observed from the CV curves. After long-term cycling, post-CV analysis was done at the same scan rate, which shows characteristic redox peaks with an enhanced current density value (Fig. 5.11). Moreover, Bissett et al. investigated liquid-phase exfoliation of crystalline MoS_2 powder, and the resultant exfoliated MoS_2 - flakes are also crystalline. However, in our case, the as-synthesized MoS_x is amorphous and has many defect sites. Also, the electrolyte used in our study is 0.5 M sulfuric acid; H^+ cations act as shuttle ions, which are much smaller than Na^+ ions. The observed increase in the current density value, as evident from the pre- and post-CV analyses, may be due to the “electroactivation” process. However the re-exfoliation of amorphous MoS_x by H^+ ions is not yet understood. In general, Li^+ ion intercalation into bulk MoS_2 facilitates the formation of highly conducting 1T phase MoS_2 [22]; however, a recent report on MoS_2 and rGO hybrid showed that a heterostructure comprising 1T MoS_2 formed at the MoS_2/rGO interface and 2H MoS_2 at the bulk [18]. In our case, the as-synthesized material is amorphous. Hence, the in-depth structural analysis of electrodes, both before and after long-term measurement, does not give any detail information. The trend of increasing capacitance retention is

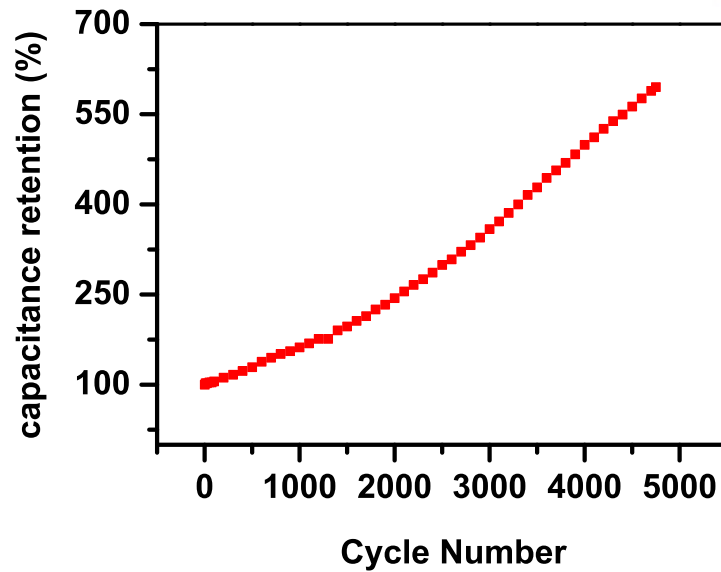


Fig. 5.10 Long term stability of device measured as a function of capacitance retention vs. cycle number.

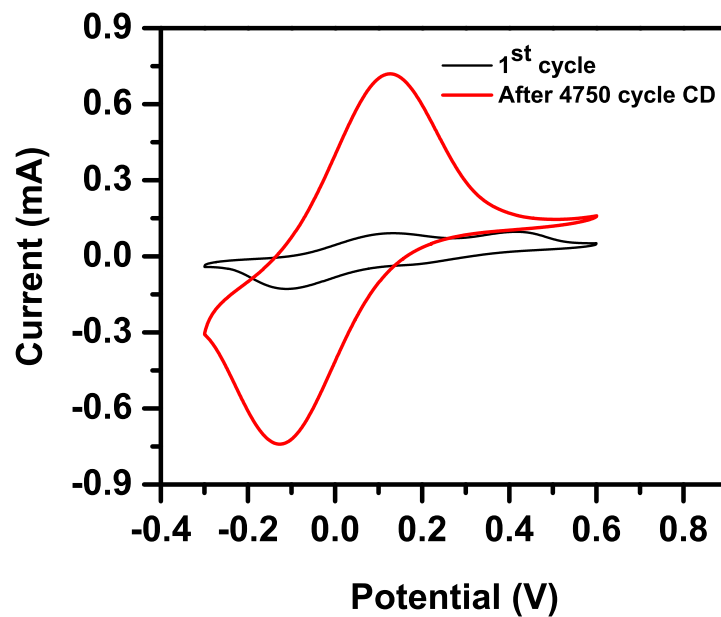


Fig. 5.11 CV curves of 1st cycle and after 4750 cycles of long term stability test.

interesting to researchers working on electrochemical energy storage devices. However, the increasing trend reaction mechanism is still unclear and under investigation.

5.4 Summary

In summary, a thin layer of amorphous MoS_x on a highly conducting 3-D network carbon fiber paper was synthesized by the facile hydrothermal method. The as-synthesized binder-free electrode material with excellent electrochemical energy-storage capability and a symmetric device showed a high specific device capacitance value of 41.96 mF cm⁻². More interestingly, because of “electroactivation”, the capacitance

retention increases up to 600% for amorphous MoS_x in the presence of a sulfuric acid medium. Although the exact mechanism of the increasing trend in capacitance retention is still under investigation, we believe that our primary observation and the obtained results may be interesting to the energy storage research community and may open up futuristic outcomes in this field.

References

- [1] Balasingam, S.K., Lee, J.S., Jun, Y., Few-layered MoSe_2 nanosheets as an advanced electrode material for supercapacitors, *Dalton Transactions* 2015, 44 (35), 15491–15498. doi:[10.1039/C5DT01985K](https://doi.org/10.1039/C5DT01985K).
- [2] Bose, R., Balasingam, S.K., Shin, S., Jin, Z., Kwon, D.H., Jun, Y., Min, Y.S., Importance of hydrophilic pretreatment in the hydrothermal growth of amorphous molybdenum sulfide for hydrogen evolution catalysis, *Langmuir* 2015, 31 (18), 5220–5227. doi:[10.1021/acs.langmuir.5b00205](https://doi.org/10.1021/acs.langmuir.5b00205).
- [3] Tan, C., Zhang, H., Two-dimensional transition metal dichalcogenide nanosheet-based composites, *Chemical Society Reviews* 2015, 44 (9), 2713–2731. doi:[10.1039/C4CS00182F](https://doi.org/10.1039/C4CS00182F).
- [4] Soon, J.M., Loh, K.P., Electrochemical double-layer capacitance of MoS_2 nanowall films, *Electrochemical and Solid-State Letters* 2007, 10 (11), 250–254. doi:[10.1149/1.2778851](https://doi.org/10.1149/1.2778851).
- [5] Chia, X., Eng, A.Y.S., Ambrosi, A., Tan, S.M., Pumera, M., Electrochemistry of nanostructured layered transition-metal dichalcogenides, *Chemical Reviews* 2015, 115 (21), 11941–11966. doi:[10.1021/acs.chemrev.5b00287](https://doi.org/10.1021/acs.chemrev.5b00287).
- [6] Rao, C.N.R., Gopalakrishnan, K., Maitra, U., Comparative study of potential applications of graphene, MoS_2 , and other two-dimensional materials in energy devices, sensors, and related areas, *ACS Applied Materials & Interfaces* 2015, 7 (15), 7809–7832. doi:[10.1021/am509096x](https://doi.org/10.1021/am509096x).
- [7] Lu, Q., Chen, J.G., Xiao, J.Q., Nanostructured electrodes for high-performance pseudocapacitors, *Angewandte Chemie International Edition* 2013, 52 (7), 1882–1889. doi:[10.1002/anie.201203201](https://doi.org/10.1002/anie.201203201).
- [8] Lu, Q., Mellinger, Z.J., Wang, W., Li, W., Chen, Y., Chen, J.G., Xiao, J.Q., Differentiation of bulk and surface contribution to supercapacitance in amorphous and crystalline nio, *ChemSusChem* 2010, 3 (12), 1367–1370. doi:[10.1002/cssc.201000270](https://doi.org/10.1002/cssc.201000270).
- [9] Zhang, Y., Sun, W., Rui, X., Li, B., Tan, H.T., Guo, G., Madhavi, S., Zong, Y., Yan, Q., One-pot synthesis of tunable crystalline Ni_3S_4 @amorphous MoS_2 core/shell nanospheres for high-performance supercapacitors, *Small* 2015, 11 (30), 3694–3702. doi:[10.1002/sml.201403772](https://doi.org/10.1002/sml.201403772).
- [10] Xiong, X., Luo, W., Hu, X., Chen, C., Qie, L., Hou, D., Huang, Y., Flexible membranes of MoS_2/c nanofibers by electrospinning as binder-free anodes for high-performance sodium-ion batteries, *Scientific Reports* 2015, 5, 9254. doi:[10.1038/srep09254](https://doi.org/10.1038/srep09254).
- [11] Acerce, M., Voiry, D., Chhowalla, M., Metallic 1t phase MoS_2 nanosheets as supercapacitor electrode materials, *Nature Nanotechnology* 2015, 10 (4), 313–318. doi:[10.1038/nnano.2015.40](https://doi.org/10.1038/nnano.2015.40).

- [12] Ramadoss, A., Kim, T., Kim, G.S., Kim, S.J., Enhanced activity of a hydrothermally synthesized mesoporous MoS₂ nanostructure for high performance supercapacitor applications, *New Journal of Chemistry* 2014, 38 (6), 2379–2385. doi:[10.1039/C3NJ01558K](https://doi.org/10.1039/C3NJ01558K).
- [13] Sun, G., Liu, J., Zhang, X., Wang, X., Li, H., Yu, Y., Huang, W., Zhang, H., Chen, P., Fabrication of ultralong hybrid microfibers from nanosheets of reduced graphene oxide and transition-metal dichalcogenides and their application as supercapacitors, *Angewandte Chemie International Edition* 2014, 53 (46), 12576–12580. doi:[10.1002/anie.201405325](https://doi.org/10.1002/anie.201405325).
- [14] Winchester, A., Ghosh, S., Feng, S., Elias, A.L., Mallouk, T., Terrones, M., Talapatra, S., Electrochemical characterization of liquid phase exfoliated two-dimensional layers of molybdenum disulfide, *ACS Applied Materials & Interfaces* 2014, 6 (3), 2125–2130. doi:[10.1021/am4051316](https://doi.org/10.1021/am4051316).
- [15] Bissett, M.A., Kinloch, I.A., Dryfe, R.A.W., Characterization of MoS₂ graphene composites for high-performance coin cell supercapacitors, *ACS Applied Materials & Interfaces* 2015, 7 (31), 17388–17398. doi:[10.1021/acsami.5b04672](https://doi.org/10.1021/acsami.5b04672).
- [16] Lee, M., Balasingam, S.K., Jeong, H.Y., Hong, W.G., Lee, H.B.R., Kim, B.H., Jun, Y., One-step hydrothermal synthesis of graphene decorated v2o5 nanobelts for enhanced electrochemical energy storage, *Sci. Rep.* 2015, 5, 8151. doi:[10.1038/srep08151](https://doi.org/10.1038/srep08151).
- [17] Ma, G., Peng, H., Mu, J., Huang, H., Zhou, X., Lei, Z., In situ intercalative polymerization of pyrrole in graphene analogue of MoS₂ as advanced electrode material in supercapacitor, *Journal of Power Sources* 2013, 229, 72 – 78. doi:[10.1016/j.jpowsour.2012.11.088](https://doi.org/10.1016/j.jpowsour.2012.11.088).
- [18] Mahmood, Q., Park, S.K., Kwon, K.D., Chang, S.J., Hong, J.Y., Shen, G., Jung, Y.M., Park, T.J., Khang, S.W., Kim, W.S., Kong, J., Park, H.S., Transition from diffusion-controlled intercalation into extrinsically pseudocapacitive charge storage of MoS₂ by nanoscale heterostructuring, *Advanced Energy Materials* 2015, n/a–n/a. doi:[10.1002/aenm.201501115](https://doi.org/10.1002/aenm.201501115).
- [19] Beidaghi, M., Wang, C., Micro-supercapacitors based on interdigital electrodes of reduced graphene oxide and carbon nanotube composites with ultrahigh power handling performance, *Advanced Functional Materials* 2012, 22 (21), 4501–4510. doi:[10.1002/adfm.201201292](https://doi.org/10.1002/adfm.201201292).
- [20] Cheng, Q., Tang, J., Ma, J., Zhang, H., Shinya, N., Qin, L.C., Graphene and carbon nanotube composite electrodes for supercapacitors with ultra-high energy density, *Physical Chemistry Chemical Physics* 2011, 13 (39), 17615–17624. doi:[10.1039/C1CP21910C](https://doi.org/10.1039/C1CP21910C).
- [21] Cheng, Q., Tang, J., Ma, J., Zhang, H., Shinya, N., Qin, L.C., Graphene and nanostructured MnO₂ composite electrodes for supercapacitors, *Carbon* 2011, 49 (9), 2917–2925. doi:[10.1016/j.carbon.2011.02.068](https://doi.org/10.1016/j.carbon.2011.02.068).
- [22] Voiry, D., Mohite, A., Chhowalla, M., Phase engineering of transition metal dichalcogenides, *Chemical Society Reviews* 2015, 44 (9), 2702–2712. doi:[10.1039/C5CS00151J](https://doi.org/10.1039/C5CS00151J).

CHAPTER 6

A Few-layered MoSe₂ Nanosheets*

**Reproduced in part from S. K. Balasingam et al., Dalton Transactions 2015, 44 (35), 15491.*

Copyright 2015 The Royal Society of Chemistry (RSC).

6.1 Introduction

Recently, TMDCs have received much attention from researchers because of their 2D sheet-like morphology, higher electrical conductivity (than the oxides), high surface area and the multivalent oxidation states of transition metal ions [1–3]. Analogous to graphite, TMDCs consists of graphene like layers of MX₂ sheets (where M can be any metal ions of IV, V and VI group transition elements and X is a chalcogen, X may be S, Se and Te) which are stacked together by weak van der Waals force. As like graphene, a monolayer or few layers of MX₂ can be exfoliated from their bulk counter part, which has a very distinct physical and chemical properties and also has a diverse application in electronic devices, photo transistors, sensors, catalysis, and electrochemical energy storage systems [4–6].

In 2007, a first report on the electrochemical double-layer capacitance measurement of MoS₂ nanowall films was published by Soon & Loh [7], which opened up the field of TMDC-based electrode materials for supercapacitor applications. Later, different morphologies of MoS₂ -, WS₂ -, and their composite-based materials were investigated as supercapacitor electrodes [8–21]. Other sulfide materials such as, VS₂ nanosheets were employed as an electrode material for in-plane supercapacitors, CoS₂ and NiS sheets were also demonstrated as an active material for supercapacitor electrodes due to their large surface area and enhanced structural stability. When compared to the sulfides, selenides are rarely studied for capacitive properties [22–27]. Moreover, recent reports on MoSe₂ based anode materials for lithium ion and sodium ion batteries, which showed them as a promising electrodes for energy storage applications. Shi et al. [28] reported mesoporous crystalline MoSe₂ using silica SBA-15 as a hard template which showed a high reversible lithium storage capacity of 630 mAh g⁻¹, Ko et al. [29] synthesized a yolk-shell structured MoSe₂ microspheres via selenization of MoO₃ microspheres, which demonstrated a high sodium ion storage capacity of 433 mAh g⁻¹. Wang et al. [30] also synthesized MoSe₂ nanoplates using thermal-decomposition process, which could deliver high sodium ion storage capacity of 513 mAh g⁻¹. The enhanced energy storage capacity of the two dimensional MoSe₂ electrode materials render our attention to investigate this material for supercapacitor applications. When compare to the bulk MoSe₂, a few-layered sheets show high surface area and unique electronic (quasiparticle bandgap) properties due to interlayer coupling and screening effects [31]. Generally few-layered MoSe₂ nanosheets are synthesized

via CVD or rapid thermal processing method which are very expensive and user-hostile techniques for the synthesis of large quantity of electrode materials [32–35]. In this work, we have synthesized a large quantity of few-layered MoSe₂ nanosheets using a facile hydrothermal method, and their electrochemical capacitance was measured in aqueous electrolyte (H₂SO₄) under a two-electrode configuration. We obtained a maximal specific capacitance of 199 F g⁻¹ at a scan rate of 2 mV s⁻¹ and also the capacitance retention of approximately 75% was observed over 10,000 cycles long-term stability test showed them as a suitable material for electrochemical capacitors.

6.2 Experimental

6.2.1 Material synthesis

The precursors, sodium molybdate (Na₂MoO₄ · 2 H₂O), selenium powder (Se), and sodium borohydride (NaBH₄), were purchased from Sigma Aldrich (ACS grade) and used without further purification. In a typical hydrothermal synthesis, precisely 1.32 g of (Na₂MoO₄ · 2 H₂O), 1.24 g of Se, and 0.2 g of NaBH₄ were weighed and dissolved in 80 ml of DI water. The mixture was continuously stirred until a red-colored solution was obtained, which is an indication of uniform distribution of the selenium metal powder. The as-prepared precursor solution was transferred into the autoclave, sealed, and then heated at 200 °C for 12 h in an electric oven. The autoclave was then naturally cooled down to room temperature. After that, the MoSe₂ nanosheets were filtered off and washed with DI water for several times to remove the residuals and then dried at 40 °C for a few hours.

6.2.2 Materials characterization

The morphology of the as-prepared sample was examined using high-resolution transmission electron microscopy (HR-TEM) (JEOL). The crystal structure and elemental composition of MoSe₂ was confirmed by X-ray diffraction (XRD, Bruker) measurements using Cu Kα emission (λ=1.5406 Å) from 10 - 90° range with a step size of 0.02°, Raman spectroscopy (WITec) using 532 nm laser excitation, after calibrating the Raman shift with a silicon reference at 521 cm⁻¹, and X-ray photoelectron spectroscopy (XPS) (Thermo Fisher, UK).

6.2.3 Cell fabrication and electrochemical measurements

The as-synthesized electroactive material (MoSe₂), carbon black and poly(vinylidene fluoride) were mixed in a mass ratio of 80:10:10 to obtain a slurry and then coated on the stainless steel (SS) substrate using the brush. An exactly 1 cm² (1 cm × 1 cm) area of MoSe₂ nanosheets-coated SS substrate was used as a single electrode. A mass loading of each electrode is around 4 mg cm⁻². Two electrodes were sandwiched together with Whatman filter paper as a separator. The assembled electrodes were placed in a test cell rig, and a few drops of 0.5 M sulfuric acid were added as the electrolyte. The test cell was sealed with an O-ring and then left for a few minutes to ensure the uniform soaking of the electrodes into the electrolyte solution before the electrochemical measurements. Electrochemical experiments were performed using a potentiostat/galvanostat (Biologic/VSP) at room temperature. Cyclic voltammetry

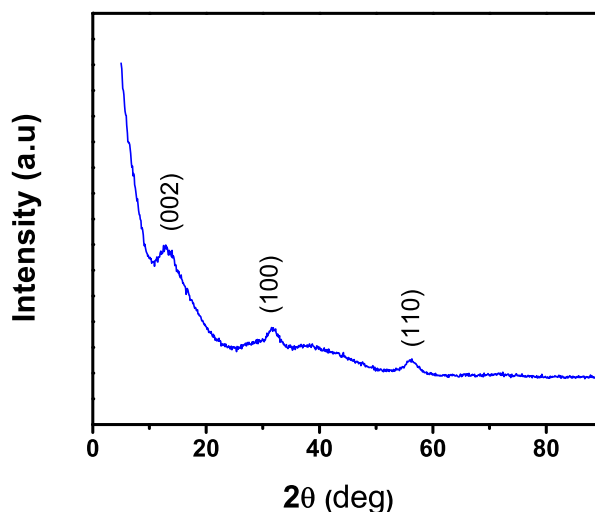


Fig. 6.1 XRD spectrum of MoSe₂ nanosheets.

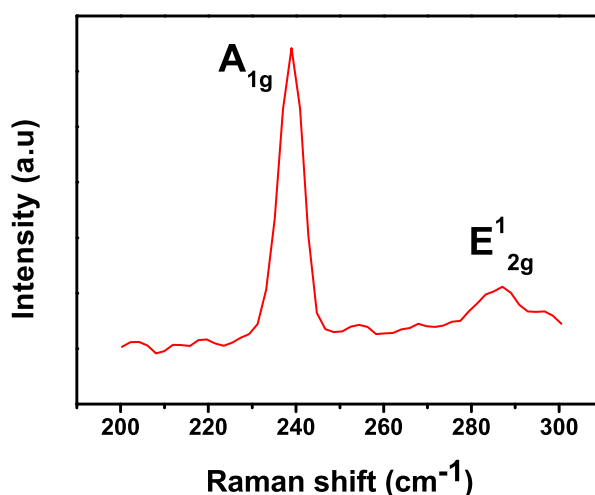


Fig. 6.2 Raman spectrum of MoSe₂ nanosheets showing two distinct A_{1g} and E_{2g}¹ Raman modes.

(CV) curves were obtained at various scan rates (2, 5, 10, 25, 50, 75, 100, and 125 mV s⁻¹) in the potential window of 0 to 0.8 V. Electrochemical impedance spectroscopy (EIS) measurements were performed over the frequency range of 0.1 Hz to 100 kHz with an AC amplitude of 10 mV. Galvanostatic charge-discharge (CD) curves were recorded at various current densities (0.10, 0.25, 0.50, 0.75, 1, 2, 3, 4, and 5 A g⁻¹) in the potential window of 0 to 0.8 V.

6.3 Results and Discussion

6.3.1 Physico-chemical analysis

The crystal structure and phase purity of the as-prepared MoSe₂ nanosheets were characterized using X-ray diffraction. Fig. 6.1 presents the XRD pattern of the MoSe₂ nanosheets. Diffraction peaks of the as-synthesized MoSe₂ nanosheets appear at 2θ = 13.3°, 31.6°, and 56°, which can be assigned to the (002), (100), and (110) planes of hexagonal phase of MoSe₂ (JCPDS No. 29-0914), respectively. The

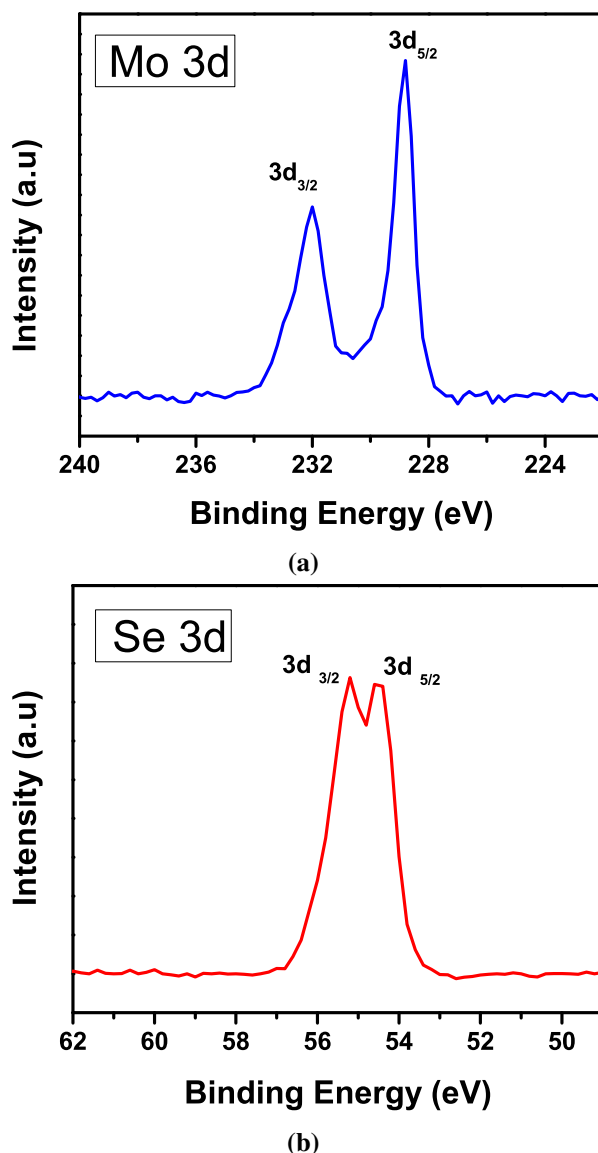


Fig. 6.3 (a) High resolution XPS spectra of Mo 3d, and (b) Se 3d regions of MoSe₂ nanosheets.

broadness of the (002) peak indicates the formation of few-layered MoSe₂ nanosheets. [8, 36]

Raman spectroscopy was employed to further study the structure of the as-synthesized MoSe₂ nanosheets. The typical peaks of MoSe₂ nanosheets at 239 cm⁻¹ and 287.11 cm⁻¹ are observed in the spectra (Fig. 6.2), which corresponds to the out-of-plane A_{1g} mode and in-plane E_{2g}¹ mode of MoSe₂, respectively [37]. For bulk MoSe₂, the A_{1g} mode appears at 242 cm⁻¹. The downward red shift of approximately 3 cm⁻¹ (A_{1g} mode @ 239 cm⁻¹) indicates the formation of few-layered MoSe₂. The E_{2g}¹ mode of bulk MoSe₂ appears at 286 cm⁻¹; however, the blue shift of this in-plane mode observed in our study also confirms the few-layered nanosheet formation [33, 38].

The chemical composition and oxidation state of the elements were investigated using X-ray photoelectron spectroscopy. Mo 3d_{3/2} and Mo 3d_{5/2} peaks (Fig 6.3a) appeared at binding energies of 232 and 228.8 eV, respectively, which confirms the +4 oxidation state of molybdenum [39]. In addition, the 3d peaks of selenium split into two well-defined peaks (Fig 6.3b) such as 3d_{3/2} and 3d_{5/2}, which appeared at binding

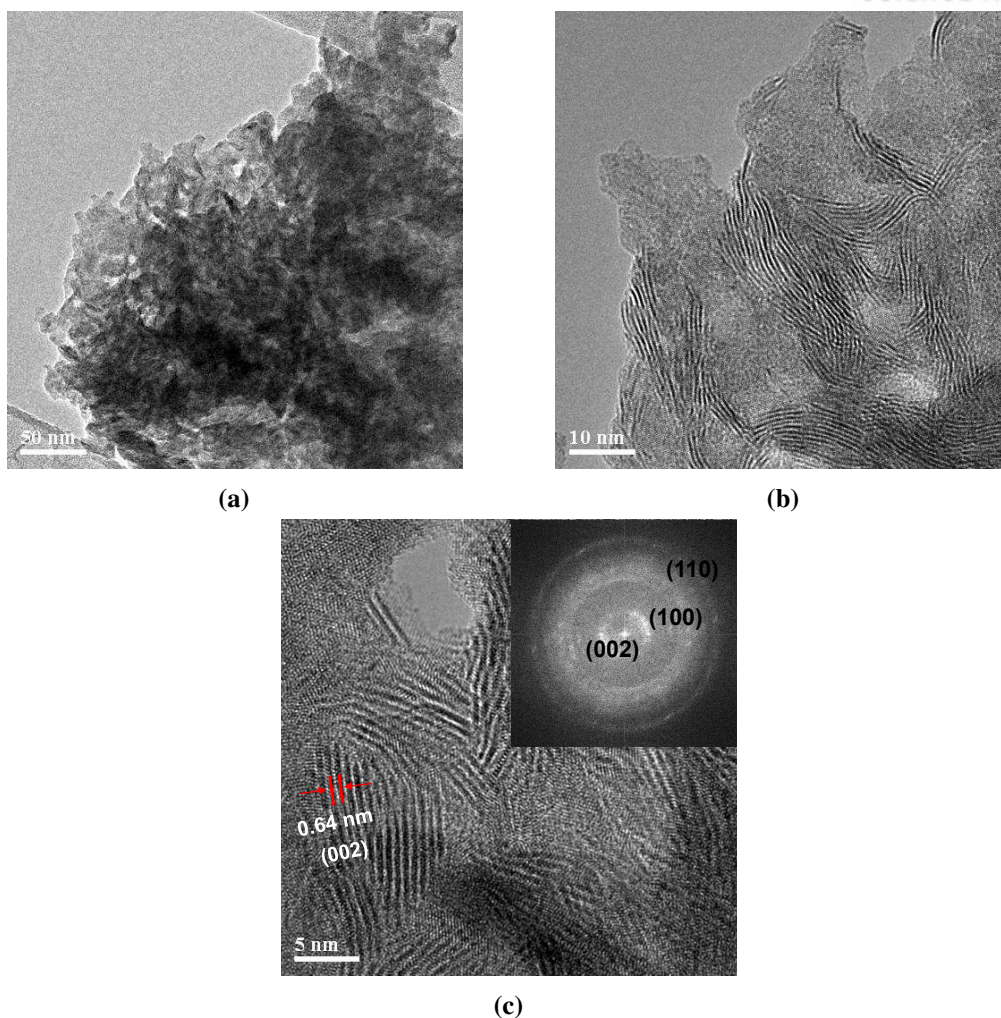


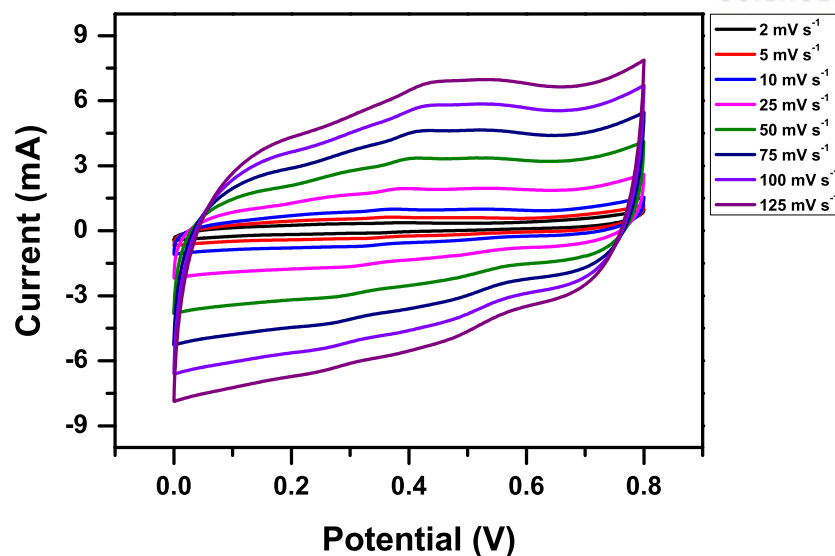
Fig. 6.4 TEM images of MoSe₂ nanosheets. (a) and (b) show low magnification, (c) high magnification; and inset of (c) shows the FFT pattern.

energies of 55.2 and 54.5 eV, confirming the -2 oxidation state of selenium in MoSe₂ nanosheets [40]. From the atomic concentration table, the mole ratio of Mo:Se was calculated to be 1:2.

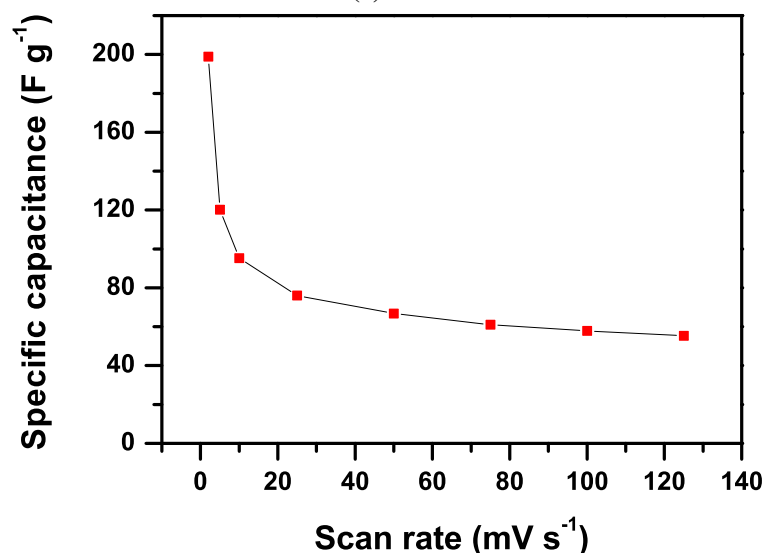
The surface morphology of the as-synthesized MoSe₂ was investigated using HR-TEM. Figure 6.4 presents HR-TEM images of the as-synthesized MoSe₂ nanostructure. The low-magnification TEM images (Fig 6.4a and 6.4b), showed MoSe₂ nanosheets. Figure 6.4c provide clear evidence of the formation of few-layered nanosheets at higher magnification. In addition, the HR-TEM images of the MoSe₂ nanosheets reveal a layered crystal structure with clear crystal lattice fringes of approximately (0.62 ± 0.03) nm, corresponding to the standard d-spacing for the (002) basal plane of the hexagonal crystal structure. Notably, the porous nature of the MoSe₂ nanosheets morphology provides a high surface area for the electrochemical reaction.

6.3.2 Electrochemical performance of symmetrical cells

The MoSe₂-nanosheets-coated stainless steel substrates were assembled in a two-electrode configuration (a symmetric cell in a parallel-plate geometry, which is typically used in supercapacitor measurements),



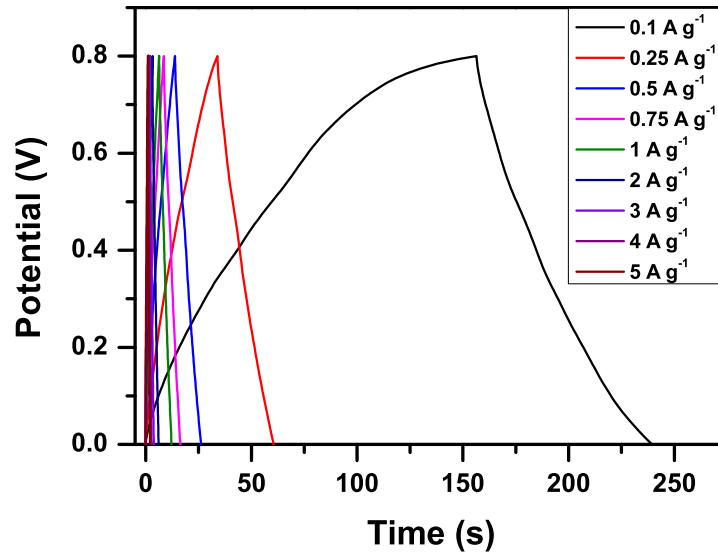
(a)



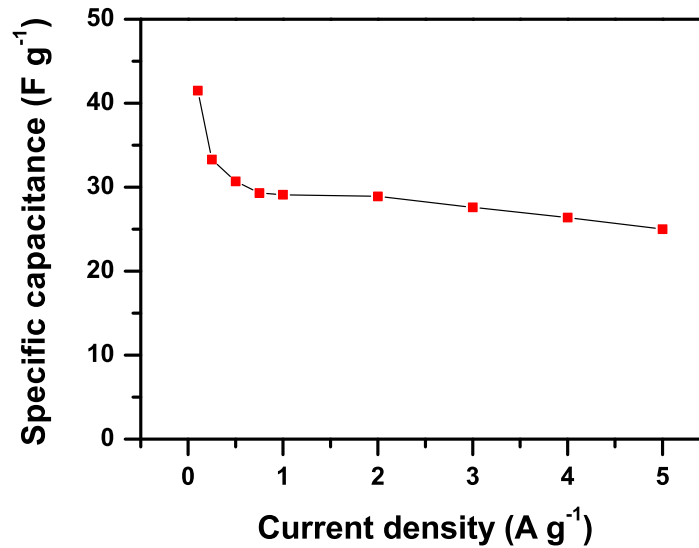
(b)

Fig. 6.5 (a) Cyclic voltammograms of MoSe₂ nanosheets in 0.5 M H₂SO₄ electrolyte measured at different scan rates ranging from 2 mV s⁻¹ to 125 mV s⁻¹, and (b) Specific capacitance value calculated from the CV curves of Fig (a) at different scan rates.

with Whatman filter paper as the separator and 0.5 M sulfuric acid as the electrolyte. The electrochemical behavior of the MoSe₂ electrodes was characterized using CV, EIS, and CD cycling measurements. Figure 6.5a shows the typical CV curves of a symmetric device (MoSe₂-nanosheets coated on a stainless steel substrate as working and counter electrodes) at various scan rates (2 mV s⁻¹ to 125 mV s⁻¹). All the CV curves retain their nearly rectangular shape at the various scan rates, which confirms the ideal EDLC behavior (non-faradaic process, as indicated in Eq. (6.1b)) of this material with excellent reversibility. Moreover, the broad peak appearing in both the anodic and cathodic scan indicates the redox behavior of the MoSe₂ nanosheets resulting from the faradaic electrochemical process, as shown in Eq. (6.1a). Notably, the redox peaks appeared even at higher scan rates with the usual peak shift. The symmetric device exhibited a measured device capacitance (C_m) of approximately 49.7 F g⁻¹ at a scan rate of 2



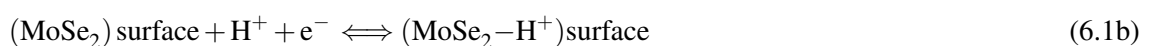
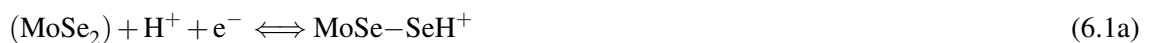
(a)



(b)

Fig. 6.6 (a) Galvanostatic charge-discharge curves of MoSe₂ nanosheets in 0.5 M H₂SO₄ electrolyte measured at different current densities ranging from 0.1 A g⁻¹ to 5 A g⁻¹, and (b) Specific capacitance value calculated from the CD curves of Fig. (a) at different current densities.

mV s⁻¹. For the single electrode, a high specific capacitance of (C_s) 198.9 F g⁻¹ was calculated at the same scan rate. The high C_s value may be attributed to the combination of both faradaic and non-faradaic processes of the 2D MoSe₂ nanosheets [7].

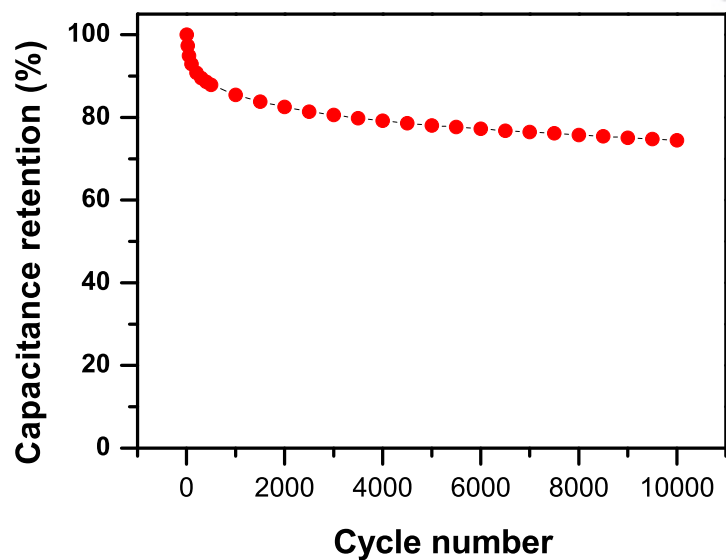


The detailed derivation of the specific capacitance for a single electrode and device is given in Eqs. (2.3), (2.4), and (2.5) (in Chapter 2). Figure 6.5b shows the relationship between the specific capacitance of the MoSe₂ nanosheets (a single electrode) at various scan rates. By increasing the scan

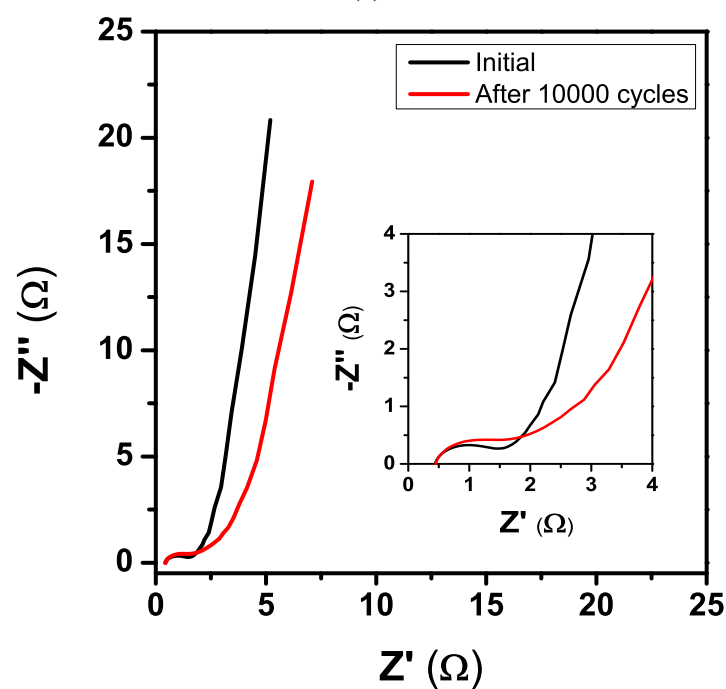
rate up to 20 mV s^{-1} , a sudden drop of the C_s value is observed, and upon further increasing the scan rate up to 125 mV s^{-1} , a gradual decrease of C_s value is recorded. This observation is a common phenomenon in supercapacitors because at higher scan rates, the mass-transport limitation of H^+ ions (from the electrolyte) to the interior (bulk) part of the electrode limits the electrochemical performance, which leads to a lower capacitance.[41–44] The specific capacitance value observed for few-layered MoSe_2 electrodes were compared with the previously reported state of the art MoS_2 and WS_2 based supercapacitors. Under similar two-electrode configuration, Winchester et al. [45] reported a specific capacitance of 2 mF cm^{-2} @ 10 mV s^{-1} scan rate in 6 M KOH electrolyte for liquid phase exfoliated MoS_2 layers. The material showed a poor capacitance retention of 68% within 200 cycles in same electrolyte. Cao et al. [21] synthesized MoS_2 nanosheets for micro-supercapacitors, a high specific capacitance of 8 mF cm^{-2} @ 10 mV s^{-1} scan rate was observed in 1 M NaOH , however the authors did not show the long-term cycle stability of this material. Ratha & Rout [8] synthesized WS_2 nanosheets by a facile hydrothermal method and the specific capacitance of 70 F g^{-1} @ 2 mV s^{-1} scan rate was reported. Under same scan rate, our material (few-layered MoSe_2 nanosheets) showed a specific capacitance of 198.9 F g^{-1} , which is almost 2.8 times higher than the WS_2 based materials. Although a recent report on metallic 1T phase MoS_2 electrode for supercapacitors measured under three-electrode configuration showed high volumetric capacitance of around 650 F cm^{-3} @ 20 mV s^{-1} , their gravimetric capacitance is approximately 190 F g^{-1} @ 5 mV s^{-1} . Where as the gravimetric capacitance value of our MoSe_2 nanosheet electrodes measured under two electrode configuration (120 F g^{-1} @ 5 mV s^{-1}) is comparable to the previous report [46].

Figure 6.6a presents the galvanostatic CD curves of a symmetric device (MoSe_2 nanosheets as the positive and negative electrodes) at various current density values. The CD curves are almost symmetric, which indicates the electrochemical capacitive behavior with remarkable reversible redox reaction. At the very low discharge current density of 0.1 A g^{-1} , a non-linear shape of the CD curve is observed with the pseudocapacitive behavior of the electrode material. The symmetric supercapacitor device exhibited a measured device capacitance of 10.4 F g^{-1} , and the single electrode exhibited a specific capacitance of approximately 41.5 F g^{-1} at a discharge current density of 0.1 A g^{-1} . The rate capability of a single MoSe_2 nanosheet electrode was investigated under various current densities, as shown in Fig 6.6b. Consistent with the CV analysis, the C_s value of the electrode material decreases at higher current density. As explained in CV, the diffusion rate of the electrolyte ions is limited at higher current density. Therefore, only the surface area of the MoSe_2 nanosheets is accessible at higher current density. For a lower-current-density CD process, the electrolyte ions could penetrate into the interior part of the electrode surface, thereby resulting in a higher C_s value.

Long cycling life is another important criteria for the application of this material in commercial supercapacitors. The cyclic stability of MoSe_2 nanosheet electrodes was measured at a high current density of 5 A g^{-1} , as observed in Fig. 6.7a. The capacitance retention is dramatically decreased for the first few hundred cycles, which may be due to the active site saturation of the surface of MoSe_2 nanosheets during the charge-discharge process [21]. Thereafter, a gradual decrease is observed until 10,000 cycles. Notably, a cycling performance of approximately 75% capacitance retention is observed even after 10,000 cycles, which indicates that MoSe_2 nanosheets are promising electrode materials for high-performance supercapacitors. The remaining 25% capacitance loss may be due to the chemical instability of MoSe_2



(a)



(b)

Fig. 6.7 (a) Specific capacitance retention of the MoSe₂ nanosheets as a function of cycle number, measured by charge-discharge at a high current density of 5 A g⁻¹ in 0.5 M H₂SO₄ electrolyte, and (b) Electrochemical impedance spectra of a symmetric device measured at the initial stage and after 10000 cycles (The inset shows an enhanced view of the high-to-medium frequency region).

in aqueous electrolyte, which can be improved by the usage of organic/ionic liquid based non-aqueous electrolytes.

EIS was performed to analyze the internal resistance and capacitance of the device. Figure 6.7b presents a Nyquist plot of the symmetric device at the initial stage and after 10,000 cycles. In the high-frequency region, the x-axis intercept of the semicircle on the z-real axis represents the electrochemical series

resistance (ESR) of the device, which was determined to be 0.43Ω . The depressed semi-circle in the high-to-medium frequency range is modeled by the parallel combination of an interfacial charge transfer resistance and double-layer capacitance. In the mid-frequency region, a typical 45° slope is observed for a short region, which is known as the Warburg impedance due to the frequency dependence of ion diffusion/transport in the electrolyte. A short Warburg region on the plot indicates a short ion diffusion path and, in turn, effective diffusion of electrolyte ions into the electrode surface [47]. In the low-frequency region, an almost 90° straight line is observed, which indicates the excellent capacitive behavior of the device [48]. EIS was performed after 10,000 cycles for the post-analysis of the device. The shape of the spectrum after 10,000 cycles is similar to the initial shape, except for the diameter of the semi-circle arc in the high-to-medium frequency range. The semi-circle arc of the device increased from 1 to 1.5Ω after 10,000 cycles, which might be due to the adhesion loss of some electroactive materials from the stainless steel current collector or dissolution of some electroactive materials during the repeated charge/discharge process [49–51]. The superior electrochemical performance of the few-layered MoSe_2 nanosheets may be attributed to the following reasons: (1) the 2D sheet-like structure provides a high surface area and more active sites for the fast reversible redox reaction on the surface of the electrode and (2) the few-layered MoSe_2 nanosheets stacked together with van der Waals force allow the effective intercalation of H^+ ions from the electrolyte.

6.4 Summary

In summary, this work reports the facile synthesis of few-layered MoSe_2 nanosheets and their capacitive properties in the two-electrode configuration using aqueous electrolyte. The symmetric device exhibited a measured capacitance of approximately 49.7 F g^{-1} , and the single electrode exhibited a specific capacitance of approximately 199 F g^{-1} at a scan rate of 2 mV s^{-1} . The excellent capacitive performance of the device is mainly attributed to the graphene-like 2D layered crystal structure, which provides a high surface area and allows effective diffusion of H^+ ions for the fast reversible redox process. The good cyclic stability and capacitance retention of approximately 75% are observed even after 10,000 cycles, which indicates that MoSe_2 nanosheets could be a potential candidate for electrochemical capacitors.

References

- [1] Buscema, M., Island, J.O., Groenendijk, D.J., Blanter, S.I., Steele, G.A., van der Zant, H.S.J., Castellanos-Gomez, A., Photocurrent generation with two-dimensional van der waals semiconductors, *Chemical Society Reviews* 2015, 44 (11), 3691–3718. doi:[10.1039/C5CS00106D](https://doi.org/10.1039/C5CS00106D).
- [2] Park, S.K., Yu, S.H., Woo, S., Quan, B., Lee, D.C., Kim, M.K., Sung, Y.E., Piao, Y., A simple l-cysteine-assisted method for the growth of MoS_2 nanosheets on carbon nanotubes for high-performance lithium ion batteries, *Dalton Transactions* 2013, 42 (7), 2399–2405. doi:[10.1039/C2DT32137H](https://doi.org/10.1039/C2DT32137H).
- [3] Wang, H., Feng, H., Li, J., Graphene and graphene-like layered transition metal dichalcogenides in energy conversion and storage, *Small* 2014, 10 (11), 2165–2181. doi:[10.1002/smll.201303711](https://doi.org/10.1002/smll.201303711).

- [4] Rao, C.N.R., Maitra, U., Waghmare, U.V., Extraordinary attributes of 2-dimensional MoS₂ nanosheets, *Chemical Physics Letters* 2014, 609, 172–183. doi:[10.1016/j.cplett.2014.06.003](https://doi.org/10.1016/j.cplett.2014.06.003).
- [5] Li, H., Yu, K., Lei, X., Guo, B., Li, C., Fu, H., Zhu, Z., Synthesis of the MoS₂ @ CuO heterogeneous structure with improved photocatalysis performance and H₂O adsorption analysis, *Dalton Transactions* 2015, 44 (22), 10438–10447. doi:[10.1039/C5DT01125F](https://doi.org/10.1039/C5DT01125F).
- [6] Pumera, M., Sofer, Z., Ambrosi, A., Layered transition metal dichalcogenides for electrochemical energy generation and storage, *Journal of Materials Chemistry A* 2014, 2 (24), 8981–8987. doi:[10.1039/c4ta00652f](https://doi.org/10.1039/c4ta00652f).
- [7] Soon, J.M., Loh, K.P., Electrochemical double-layer capacitance of MoS₂ nanowall films, *Electrochemical and Solid-State Letters* 2007, 10 (11), 250–254. doi:[10.1149/1.2778851](https://doi.org/10.1149/1.2778851).
- [8] Ratha, S., Rout, C.S., Supercapacitor electrodes based on layered tungsten disulfide-reduced graphene oxide hybrids synthesized by a facile hydrothermal method, *ACS Applied Materials and Interfaces* 2013, 5 (21), 11427–11433. doi:[10.1021/am403663f](https://doi.org/10.1021/am403663f).
- [9] Da Silveira Firmiano, E.G., Rabelo, A.C., Dalmaschio, C.J., Pinheiro, A.N., Pereira, E.C., Schreiner, W.H., Leite, E.R., Supercapacitor electrodes obtained by directly bonding 2d MoS₂ on reduced graphene oxide, *Advanced Energy Materials* 2014, 4 (6), 1301380. doi:[10.1002/aenm.201301380](https://doi.org/10.1002/aenm.201301380).
- [10] Hao, C., Wen, F., Xiang, J., Wang, L., Hou, H., Su, Z., Hu, W., Liu, Z., Controlled incorporation of Ni(OH)₂ nanoplates into flower-like MoS₂ nanosheets for flexible all-solid-state supercapacitors, *Advanced Functional Materials* 2014, 24 (42), 6700–6707. doi:[10.1002/adfm.201401268](https://doi.org/10.1002/adfm.201401268).
- [11] Tang, H., Wang, J., Yin, H., Zhao, H., Wang, D., Tang, Z., Growth of polypyrrole ultrathin films on MoS₂ monolayers as high-performance supercapacitor electrodes, *Advanced Materials* 2015, 27 (6), 1117–1123. doi:[10.1002/adma.201404622](https://doi.org/10.1002/adma.201404622).
- [12] Sun, G., Zhang, X., Lin, R., Yang, J., Zhang, H., Chen, P., Hybrid fibers made of molybdenum disulfide, reduced graphene oxide, and multi-walled carbon nanotubes for solid-state, flexible, asymmetric supercapacitors, *Angewandte Chemie International Edition* 2015, 54 (15), 4651–4656. doi:[10.1002/anie.201411533](https://doi.org/10.1002/anie.201411533).
- [13] Liu, M., Li, G., Chen, X., One-pot controlled synthesis of spongelike CuInS₂ microspheres for efficient counter electrode with graphene assistance in dye-sensitized solar cells, *ACS Applied Materials & Interfaces* 2014, 6 (4), 2604–2610.
- [14] Hu, B., Qin, X., Asiri, A.M., Alamry, K.A., Al-Youbi, A.O., Sun, X., WS₂ nanoparticles-encapsulated amorphous carbon tubes: A novel electrode material for supercapacitors with a high rate capability, *Electrochemistry Communications* 2013, 28, 75–78. doi:[10.1016/j.elecom.2012.11.035](https://doi.org/10.1016/j.elecom.2012.11.035).
- [15] Hu, B., Qin, X., Asiri, A.M., Alamry, K.A., Al-Youbi, A.O., Sun, X., Synthesis of porous tubular c/MoS₂ nanocomposites and their application as a novel electrode material for supercapacitors with excellent cycling stability, *Electrochimica Acta* 2013, 100, 24–28. doi:[10.1016/j.electacta.2013.03.133](https://doi.org/10.1016/j.electacta.2013.03.133).

- [16] Huang, K.J., Zhang, J.Z., Shi, G.W., Liu, Y.M., Hydrothermal synthesis of molybdenum disulfide nanosheets as supercapacitors electrode material, *Electrochimica Acta* 2014, 132, 397–403. doi:[10.1016/j.electacta.2014.04.007](https://doi.org/10.1016/j.electacta.2014.04.007).
- [17] Huang, K.J., Wang, L., Liu, Y.J., Liu, Y.M., Wang, H.B., Gan, T., Wang, L.L., Layered MoS₂-graphene composites for supercapacitor applications with enhanced capacitive performance, *International Journal of Hydrogen Energy* 2013, 38 (32), 14027–14034. doi:[10.1016/j.ijhydene.2013.08.112](https://doi.org/10.1016/j.ijhydene.2013.08.112).
- [18] Zhou, X., Xu, B., Lin, Z., Shu, D., Ma, L., Hydrothermal synthesis of flower-like MoS₂ nanospheres for electrochemical supercapacitors, *Journal of Nanoscience and Nanotechnology* 2014, 14 (9), 7250–7254. doi:[10.1166/jnn.2014.8929](https://doi.org/10.1166/jnn.2014.8929).
- [19] Gopalakrishnan, K., Sultan, S., Govindaraj, A., Rao, C.N.R., Supercapacitors based on composites of pani with nanosheets of nitrogen-doped rgo, BC_{1.5}N, MoS₂ and WS₂, *Nano Energy* 2015, 12, 52–58. doi:[10.1016/j.nanoen.2014.12.005](https://doi.org/10.1016/j.nanoen.2014.12.005).
- [20] Ramadoss, A., Kim, T., Kim, G.S., Kim, S.J., Enhanced activity of a hydrothermally synthesized mesoporous MoS₂ nanostructure for high performance supercapacitor applications, *New Journal of Chemistry* 2014, 38 (6), 2379–2385. doi:[10.1039/C3NJ01558K](https://doi.org/10.1039/C3NJ01558K).
- [21] Cao, L., Yang, S., Gao, W., Liu, Z., Gong, Y., Ma, L., Shi, G., Lei, S., Zhang, Y., Zhang, S., Vajtai, R., Ajayan, P.M., Direct laser-patterned micro-supercapacitors from paintable MoS₂ films, *Small* 2013, 9 (17), 2905–2910. doi:[10.1002/sml.201203164](https://doi.org/10.1002/sml.201203164).
- [22] Feng, J., Sun, X., Wu, C., Peng, L., Lin, C., Hu, S., Yang, J., Xie, Y., Metallic few-layered VS₂ ultrathin nanosheets: High two-dimensional conductivity for in-plane supercapacitors, *Journal of the American Chemical Society* 2011, 133 (44), 17832–17838. doi:[10.1021/ja207176c](https://doi.org/10.1021/ja207176c).
- [23] Wang, Q., Jiao, L., Du, H., Yang, J., Huan, Q., Peng, W., Si, Y., Wang, Y., Yuan, H., Facile synthesis and superior supercapacitor performances of three-dimensional cobalt sulfide hierarchitectures, *CrystEngComm* 2011, 13 (23), 6960–6963. doi:[10.1039/C1CE06082A](https://doi.org/10.1039/C1CE06082A).
- [24] Yang, J., Duan, X., Qin, Q., Zheng, W., Solvothermal synthesis of hierarchical flower-like [small beta]-nis with excellent electrochemical performance for supercapacitors, *Journal of Materials Chemistry A* 2013, 1 (27), 7880–7884. doi:[10.1039/C3TA11167A](https://doi.org/10.1039/C3TA11167A).
- [25] Zhang, L., Wu, H.B., Lou, X.W., Unusual CoS₂ ellipsoids with anisotropic tube-like cavities and their application in supercapacitors, *Chemical Communications* 2012, 48 (55), 6912–6914. doi:[10.1039/C2CC32750C](https://doi.org/10.1039/C2CC32750C).
- [26] Zhu, B.T., Wang, Z., Ding, S., Chen, J.S., Lou, X.W., Hierarchical nickel sulfide hollow spheres for high performance supercapacitors, *RSC Advances* 2011, 1 (3), 397–400. doi:[10.1039/C1RA00240F](https://doi.org/10.1039/C1RA00240F).
- [27] Huang, K.J., Zhang, J.Z., Fan, Y., Preparation of layered MoSe₂ nanosheets on Ni-foam substrate with enhanced supercapacitor performance, *Materials Letters* 2015, 152 (0), 244–247. doi:[10.1016/j.matlet.2015.03.130](https://doi.org/10.1016/j.matlet.2015.03.130).

- [28] Shi, Y., Hua, C., Li, B., Fang, X., Yao, C., Zhang, Y., Hu, Y.S., Wang, Z., Chen, L., Zhao, D., Stucky, G.D., Highly ordered mesoporous crystalline MoSe₂ material with efficient visible-light-driven photocatalytic activity and enhanced lithium storage performance, *Advanced Functional Materials* 2013, 23 (14), 1832–1838. doi:[10.1002/adfm.201202144](https://doi.org/10.1002/adfm.201202144).
- [29] Ko, Y.N., Choi, S.H., Park, S.B., Kang, Y.C., Hierarchical MoSe₂ yolk-shell microspheres with superior na-ion storage properties, *Nanoscale* 2014, 6 (18), 10511–10515. doi:[10.1039/C4NR02538E](https://doi.org/10.1039/C4NR02538E).
- [30] Wang, H., Lan, X., Jiang, D., Zhang, Y., Zhong, H., Zhang, Z., Jiang, Y., Sodium storage and transport properties in pyrolysis synthesized MoSe₂ nanoplates for high performance sodium-ion batteries, *Journal of Power Sources* 2015, 283 (0), 187–194. doi:[10.1016/j.jpowsour.2015.02.096](https://doi.org/10.1016/j.jpowsour.2015.02.096).
- [31] Bradley, A.J., M. Ugeda, M., da Jornada, F.H., Qiu, D.Y., Ruan, W., Zhang, Y., Wickenburg, S., Riss, A., Lu, J., Mo, S.K., Hussain, Z., Shen, Z.X., Louie, S.G., Crommie, M.F., Probing the role of interlayer coupling and coulomb interactions on electronic structure in few-layer MoSe₂ nanostructures, *Nano Letters* 2015, 15 (4), 2594–2599. doi:[10.1021/acs.nanolett.5b00160](https://doi.org/10.1021/acs.nanolett.5b00160).
- [32] Bachmatiuk, A., Abelin, R.F., Quang, H.T., Trzebicka, B., Eckert, J., Rummeli, M.H., Chemical vapor deposition of twisted bilayer and few-layer MoSe₂ over SiO_x substrates, *Nanotechnology* 2014, 25 (36), 365603. doi:[10.1088/0957-4484/25/36/365603](https://doi.org/10.1088/0957-4484/25/36/365603).
- [33] Lee, L.T.L., He, J., Wang, B., Ma, Y., Wong, K.Y., Li, Q., Xiao, X., Chen, T., Few-layer MoSe₂ possessing high catalytic activity towards iodide/tri-iodide redox shuttles, *Scientific Reports* 2014, 4, 4063. doi:[10.1038/srep04063](https://doi.org/10.1038/srep04063).
- [34] Mutlu, Z., Wickramaratne, D., Bay, H.H., Favors, Z.J., Ozkan, M., Lake, R., Ozkan, C.S., Synthesis, characterization, and electronic structure of few-layer MoSe₂ granular films, *Physica status solidi (a)* 2014, 211 (12), 2671–2676. doi:[10.1002/pssa.201431131](https://doi.org/10.1002/pssa.201431131).
- [35] Xia, J., Huang, X., Liu, L.Z., Wang, M., Wang, L., Huang, B., Zhu, D.D., Li, J.J., Gu, C.Z., Meng, X.M., Cvd synthesis of large-area, highly crystalline MoSe₂ atomic layers on diverse substrates and application to photodetectors, *Nanoscale* 2014, 6 (15), 8949–8955. doi:[10.1039/C4NR02311K](https://doi.org/10.1039/C4NR02311K).
- [36] Miremedi, B.K., Morrison, S.R., The intercalation and exfoliation of tungsten disulfide, *Journal of Applied Physics* 1988, 63 (10), 4970–4974. doi:[10.1063/1.340441](https://doi.org/10.1063/1.340441).
- [37] Sekine, T., Izumi, M., Nakashizu, T., Uchinokura, K., Matsuura, E., Raman scattering and infrared reflectance in 2h-MoSe₂, *Journal of the Physical Society of Japan* 1980, 49 (3), 1069–1077. doi:[10.1143/JPSJ.49.1069](https://doi.org/10.1143/JPSJ.49.1069).
- [38] Tonndorf, P., Schmidt, R., Böttger, P., Zhang, X., Börner, J., Liebig, A., Albrecht, M., Kloc, C., Gordan, O., Zahn, D.R.T., Michaelis de Vasconcellos, S., Bratschitsch, R., Photoluminescence emission and raman response of monolayer MoS₂, MoSe₂, and WSe₂, *Optics Express* 2013, 21 (4), 4908–4916. doi:[10.1364/OE.21.004908](https://doi.org/10.1364/OE.21.004908).
- [39] Tang, H., Dou, K., Kaun, C.C., Kuang, Q., Yang, S., MoSe₂ nanosheets and their graphene hybrids: synthesis, characterization and hydrogen evolution reaction studies, *Journal of Materials Chemistry A* 2014, 2 (2), 360–364. doi:[10.1039/C3TA13584E](https://doi.org/10.1039/C3TA13584E).

- [40] Wang, H., Kong, D., Johanes, P., Cha, J.J., Zheng, G., Yan, K., Liu, N., Cui, Y., MoSe₂ and WSe₂ nanofilms with vertically aligned molecular layers on curved and rough surfaces, *Nano Letters* 2013, 13 (7), 3426–3433. doi:[10.1021/nl401944f](https://doi.org/10.1021/nl401944f).
- [41] Gao, Y., Pandey, G., Turner, J., Westgate, C., Sammakia, B., Chemical vapor-deposited carbon nanofibers on carbon fabric for supercapacitor electrode applications, *Nanoscale Research Letters* 2012, 7 (1), 651. doi:[10.1186/1556-276X-7-651](https://doi.org/10.1186/1556-276X-7-651).
- [42] Chen, W., Rakhi, R.B., Alshareef, H.N., High energy density supercapacitors using macroporous kitchen sponges, *Journal of Materials Chemistry* 2012, 22 (29), 14394–14402. doi:[10.1039/C2JM32030D](https://doi.org/10.1039/C2JM32030D).
- [43] Li, H.B., Yu, M.H., Wang, F.X., Liu, P., Liang, Y., Xiao, J., Wang, C.X., Tong, Y.X., Yang, G.W., Amorphous nickel hydroxide nanospheres with ultrahigh capacitance and energy density as electrochemical pseudocapacitor materials, *Nature Communications* 2013, 4, 1894. doi:[10.1038/ncomms2932](https://doi.org/10.1038/ncomms2932).
- [44] Mai, L., Li, H., Zhao, Y., Xu, L., Xu, X., Luo, Y., Zhang, Z., Ke, W., Niu, C., Zhang, Q., Fast ionic diffusion-enabled nanoflake electrode by spontaneous electrochemical pre-intercalation for high-performance supercapacitor, *Scientific Reports* 2013, 3, 1718. doi:[10.1038/srep01718](https://doi.org/10.1038/srep01718).
- [45] Winchester, A., Ghosh, S., Feng, S., Elias, A.L., Mallouk, T., Terrones, M., Talapatra, S., Electrochemical characterization of liquid phase exfoliated two-dimensional layers of molybdenum disulfide, *ACS Applied Materials & Interfaces* 2014, 6 (3), 2125–2130. doi:[10.1021/am4051316](https://doi.org/10.1021/am4051316).
- [46] Acerce, M., Voiry, D., Chhowalla, M., Metallic 1t phase MoS₂ nanosheets as supercapacitor electrode materials, *Nature Nanotechnology* 2015, 10 (4), 313–318. doi:[10.1038/nnano.2015.40](https://doi.org/10.1038/nnano.2015.40).
- [47] Foo, C.Y., Sumboja, A., Tan, D.J.H., Wang, J., Lee, P.S., Flexible and highly scalable V₂O₅-rgo electrodes in an organic electrolyte for supercapacitor devices, *Advanced Energy Materials* 2014, 4 (12), 1400236. doi:[10.1002/aem.201400236](https://doi.org/10.1002/aem.201400236).
- [48] Kim, T.Y., Lee, H.W., Stoller, M., Dreyer, D.R., Bielawski, C.W., Ruoff, R.S., Suh, K.S., High-performance supercapacitors based on poly(ionic liquid)-modified graphene electrodes, *ACS Nano* 2011, 5 (1), 436–442. doi:[10.1021/mn101968p](https://doi.org/10.1021/mn101968p).
- [49] Wang, H.Q., Li, Z.S., Huang, Y.G., Li, Q.Y., Wang, X.Y., A novel hybrid supercapacitor based on spherical activated carbon and spherical MnO₂ in a non-aqueous electrolyte, *Journal of Materials Chemistry* 2010, 20 (19), 3883–3889. doi:[10.1039/C000339E](https://doi.org/10.1039/C000339E).
- [50] Yan, J., Wei, T., Qiao, W., Shao, B., Zhao, Q., Zhang, L., Fan, Z., Rapid microwave-assisted synthesis of graphene nanosheet/Co₃O₄ composite for supercapacitors, *Electrochimica Acta* 2010, 55 (23), 6973–6978. doi:[10.1016/j.electacta.2010.06.081](https://doi.org/10.1016/j.electacta.2010.06.081).
- [51] Yan, J., Fan, Z., Wei, T., Qian, W., Zhang, M., Wei, F., Fast and reversible surface redox reaction of graphene–MnO₂ composites as supercapacitor electrodes, *Carbon* 2010, 48 (13), 3825–3833. doi:[10.1016/j.carbon.2010.06.047](https://doi.org/10.1016/j.carbon.2010.06.047).

MoSe₂/rGO Hybrid Nanosheets Electrode

7.1 Introduction

Electrode materials for EDLCs are usually carbon-based materials such as activated carbon, carbon nanotubes, carbon nanofibers, and graphene [1–4]. However, the specific capacitance of carbon-based materials is generally low due to the limited specific surface area and non-uniform pore size distribution of these materials, which in turn limits the effective utilization of these electroactive materials in supercapacitors [5, 6]. On the other hand, transition metal oxides [7, 8], metal hydroxides [9–11], conducting polymers [12], and transition metal dichalcogenides [13, 14] have been widely used as electrode materials for pseudocapacitors due to their much higher specific capacitance. Although, pseudocapacitors generally have high specific capacitance, the poor cycling stability and low conductivity of the pseudocapacitive materials limit their practical application in the energy storage field [15, 16]. In order to overcome these issues as well as to achieve enhanced electrochemical performance, novel hierarchical hybrid nanostructures combining EDLCs and pseudocapacitors have emerged, where these systems have a large surface area, good electrical conductivity, and a short path for ion diffusion.

Recently, transition metal dichalcogenides (TMDCs), MX₂ (M = Mo, W; X = S, Se), with a layered structure (analogous to graphene) have emerged as one of the most prominent candidates for energy storage, catalysis, photo-transistors, and sensor systems due to their unique crystal structures and diverse material properties [13, 14, 17–19]. In these materials, metals and chalcogens interact via strong chemical bonds in the molecular layers, whereas the individual layers interact via weak Van der Waals forces, forming a graphene-like layered structure. This structure is beneficial for the insertion and extraction of a variety of electrolyte ions and can be exploited in the field of energy storage [14, 20, 21]. Among the TMDC materials, molybdenum diselenide (MoSe₂), which is an important narrow-band-gap semiconductor that has a layered structure (Se-Mo-Se), similar to MoS₂, might be a good choice for energy storage devices [22, 23]. Furthermore, the interlayer spacing of MoSe₂ (0.646 nm) is larger than that of graphite (0.335 nm) and MoS₂ (0.615 nm) [21]. Therefore, MoSe₂ is considered as one of the most promising electrode materials for lithium-ion batteries, sodium-ion batteries, and supercapacitors. Nevertheless, very little research has been carried out on the electrochemical performance of lithium-ion batteries, sodium ion batteries, and supercapacitors employing MoSe₂ [20, 21, 24–27]. Although, MoSe₂ has been applied in energy storage, the poor electrical conductivity of MoSe₂, similar to that of other metal oxides, hinders its electrochemical performance and practical implementation.

A commonly employed strategy to further enhance the electrochemical performance of MoSe₂ involves the

design of a hybrid nanostructure with a carbon matrix. Compared with other carbon materials, graphene is considered as the most auspicious matrix to support host materials because of its intriguing advantages, including large specific surface area, superior electrical conductivity, good chemical stability, and excellent mechanical flexibility [28–31]. Due to its outstanding properties, graphene shows excellent potential as an electrode material for high-performance supercapacitors. Moreover, the graphene nanosheets in the hybrid nanostructure serve as a powerful support, which could provide better electrical conductivity, curtail aggregation of the target nanomaterials, and shorten the transport paths for effective mass and charge transport. Furthermore, grafting with MoSe₂ can also effectively reduce restacking of the graphene nanosheets, thereby facilitating complete utilization of the surface active sites and further accelerating ion diffusion. Hence, it is expected that the hybrid nanostructure of MoSe₂/graphene, in which MoSe₂ nanosheets are uniformly distributed in the graphene matrix, should be an effective and competitive platform to achieve outstanding electrochemical performance by combining the advantages of the individual components while exploiting their synergistic effects in the electrode matrix [21].

To the best of our knowledge, only a few studies have explored the use of MoSe₂ and graphene/MoSe₂ composites for energy storage applications. For instance, Huang et al. utilized the direct growth of pristine MoSe₂ and graphene/MoSe₂ composites on a Ni-foam current collector via a hydrothermal method. Although the binder-free electrodes showed very high specific capacitance values of 1114.3 F g⁻¹ (MoSe₂/Ni) [26] and 1422 F g⁻¹ (MoSe₂-graphene/Ni) [25] at 1 A g⁻¹ using a three electrode system with 6 M KOH electrolyte, the structural conformation of the as-synthesized product was unclear from comparison of the XRD data with the standard JCPDS card. Moreover, the stability of molybdenum sulfide and selenides in high pH alkaline medium is very poor according to the pour-biax diagram [13]. Furthermore, not much improvement in the specific capacitance of graphene-MoSe₂/Ni composites was observed relative to the MoSe₂/Ni counterparts, highlighting the need to study the electrochemical performance of pristine MoSe₂ in more stable electrolyte media. Recently, we demonstrated the synthesis of few-layered MoSe₂ nanosheets for use in symmetric supercapacitors, achieving a specific device capacitance of 30 F g⁻¹ (corresponding to a single electrode specific capacitance of 120 F g⁻¹) at a scan rate of 5 mV s⁻¹ [24]. The long-term stability of pure MoSe₂ was approximately 75% at a high charge-discharge current density of 5 A g⁻¹. Hence, enhancement of the electrode performance of MoSe₂-based supercapacitors remains a pertinent undertaking to meet the demands of commercial applications.

Herein, a facile, low cost, and scalable approach for synthesis of MoSe₂/rGO nanosheet electrode materials via a hydrothermal method is introduced. The MoSe₂/rGO nanosheet hybrid nanostructure results in intimate hybridization of the conductive reduced graphene network with the evenly distributed MoSe₂ nanosheets. The hybridized nanostructure improves the electrical conductivity; in turn, the electrochemical redox reaction of MoSe₂ and the presence of the rGO nanosheets enhance the electrical double layer capacitance of the supercapacitor electrodes through effective electron transport and fast ion diffusion. The structure, morphology, and chemical composition of the as-synthesized MoSe₂/rGO nanosheets are characterized herein. The as-prepared hybrid nanostructure exhibits a maximum specific capacitance of 211 F g⁻¹ at a scan rate of 5 mV s⁻¹ and a good capacitance retention ratio of 180% even after 10,000 cycles at a current density of 5 A g⁻¹.

7.2 Experimental

7.2.1 Synthesis of MoSe₂/reduced graphene oxide nanosheets

All of the chemicals and reagents used in the experiments were of analytical grade and were used without any further purification. Graphene oxide (GO) was synthesized from natural graphite powder by a modified Hummer's method [32, 33]. Approximately 0.46 g of GO was dispersed in water and sonicated for 30 min in 30 ml of deionized (DI) water. Exactly 15.7 mmol selenium metal powder (Se) and 0.2 g of sodium borohydride (NaBH₄) were mixed in 50 ml of deionized (DI) water under vigorous stirring for 15 min. Precisely 5.455 mmol sodium molybdate (Na₂MoO₄ · 2 H₂O) was weighed and added to the NaBH₄ and Se mixture, followed by continuous stirring until a red solution was obtained. The GO dispersion was added dropwise to this solution with continuous stirring for 30 min in order to ensure uniform dispersion of GO in the precursor solution. The as-prepared precursor solution was poured into a Teflon-lined stainless steel autoclave that was then tightly sealed. The autoclave was immediately transferred into an electric oven and the reaction temperature was maintained at 200 °C for 12 h. After completion of the hydrothermal reaction, the autoclave was kept inside the oven and the temperature was allowed to gradually decrease to room temperature. The resultant MoSe₂/rGO nanosheets were filtered off using Whatman filter paper and washed several times with DI water to remove residual materials and then dried in an electric oven at 40 °C overnight. For comparative purposes, pristine MoSe₂ nanosheets were also synthesized via a similar method without addition of GO.

7.2.2 Materials characterization

The crystal structure of the as-prepared sample was analyzed using an X-ray diffractometer (XRD, Bruker) with Cu K α radiation ($\lambda = 0.15141$ nm) and Raman spectroscopy (WITec) using 532 nm laser excitation, after calibrating the Raman shift with a silicon reference at 521 cm⁻¹. The surface morphology of the hybrid nanostructure was examined by field emission scanning electron microscopy (FE-SEM, Nano230, FEI Co.). The chemical composition of the sample was examined using X-ray photoelectron spectroscopy with Al K α radiation (XPS, Thermo Fisher, UK).

7.2.3 Electrochemical characterization

All electrochemical measurements were performed in a conventional three-electrode system using an electrochemical workstation (Biologic/VSP); 0.5 M H₂SO₄ solution was used as the electrolyte. The working electrodes were prepared by mixing the as-synthesized electroactive material, carbon black, and poly(vinylidene fluoride) in a mass ratio of 80:10:10 in N-methyl-2-pyrrolidone solvent. The obtained slurry was then coated onto a stainless-steel current collector and dried at 90 °C for 24 h. A large surface area platinum mesh and Ag/AgCl were used as the counter and reference electrodes, respectively. The electrochemical performance of the fabricated electrodes was characterized by cyclic voltammetry (CV), galvanostatic charge/discharge (GCD), and electrochemical impedance spectroscopy (EIS) measurements. The EIS measurements were carried out in the frequency range of 0.1 Hz to 100 kHz with an AC amplitude of 10 mV.

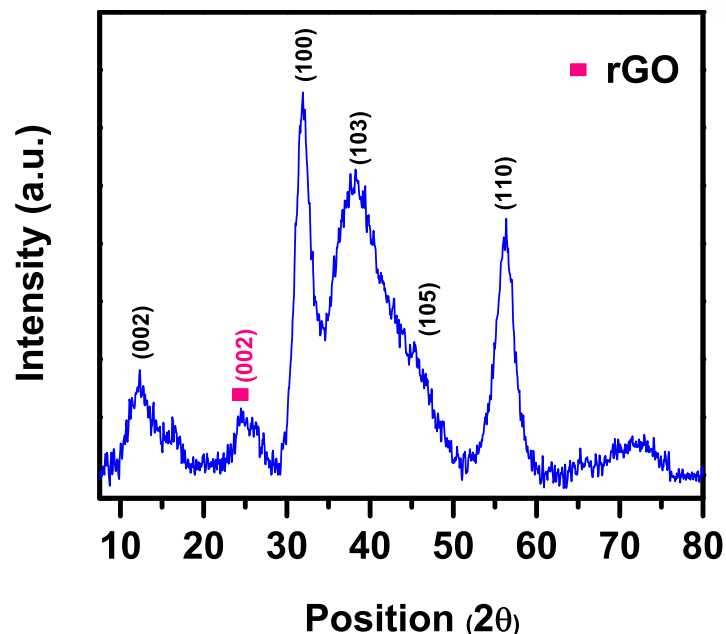


Fig. 7.1 XRD spectrum of MoSe₂/reduced graphene oxide nanosheets.

7.3 Results and Discussion

7.3.1 Physico-chemical analysis

Structural analysis of the as-prepared MoSe₂/reduced graphene oxide nanosheets was performed via X-ray diffraction (XRD). Figure 7.1 shows the XRD pattern of the MoSe₂/rGO nanosheets. The diffraction peaks appearing at $2\theta = 12.3^\circ$, 31.9° , 38.2° , 45.3° , and 56.3° correspond to the (002), (100), (103), (105), and (110) planes of hexagonal MoSe₂ (JCPDS card No: 29-0914), respectively [34]. Moreover, when the diffraction peaks of MoSe₂ are excluded, the small peak located at $2\theta = 24.6^\circ$ could be ascribed to the (002) plane of rGO [33].

The structural information was further confirmed by Raman analysis. Figure 7.2 shows the Raman spectrum of the MoSe₂/rGO nanosheets. The characteristic Raman peaks centered at 238 and 286 cm⁻¹ are related to the out-of-plane A_{1g} and in-plane E_{2g}¹ Raman modes of MoSe₂ [23, 35]. In addition to these peaks, two other high intensity bands appeared at 1349 and 1593 cm⁻¹, which are assigned to the characteristic D and G bands of rGO, respectively. The G band corresponds to vibration of the sp² carbon atom in the two-dimensional hexagonal lattice, while the D band is related to the structural defects and disorder of the graphene nanosheets[33]. The D-band to G-band intensity ratio (I_D/I_G) of the MoSe₂/rGO nanosheets was 1.51, implying an increase in the size of the sp² domains and a larger number of defects distributed over the graphene sheets during the reduction of GO via the hydrothermal process [36]. These results confirmed formation of the MoSe₂/rGO nanosheets. The morphology of the as-prepared MoSe₂/rGO nanosheets was examined using FE-SEM. Figure 7.3 show FE-SEM images of the MoSe₂/rGO nanosheets. The FE-SEM images revealed that the MoSe₂ nanosheets were uniformly distributed on the surface of the rGO nanosheets.

XPS analysis was used to further verify the chemical composition of the as-prepared sample. Figure 7.4a

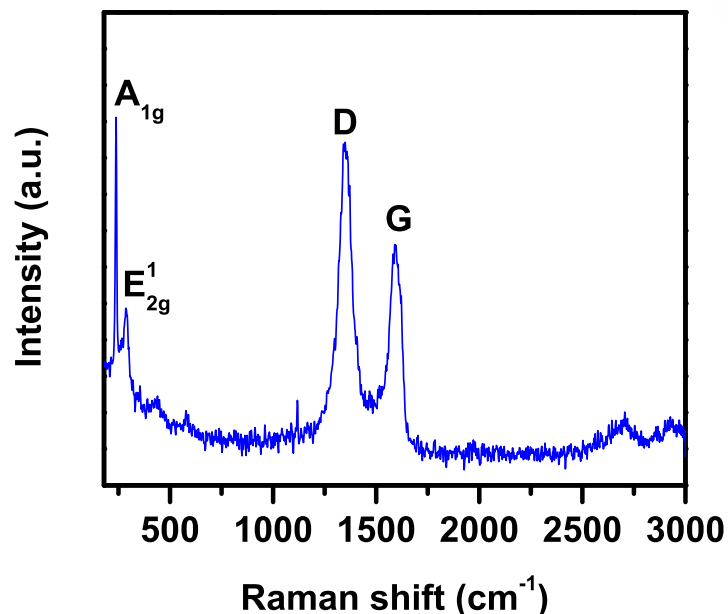


Fig. 7.2 Raman spectrum of MoSe₂/reduced graphene oxide nanosheets.

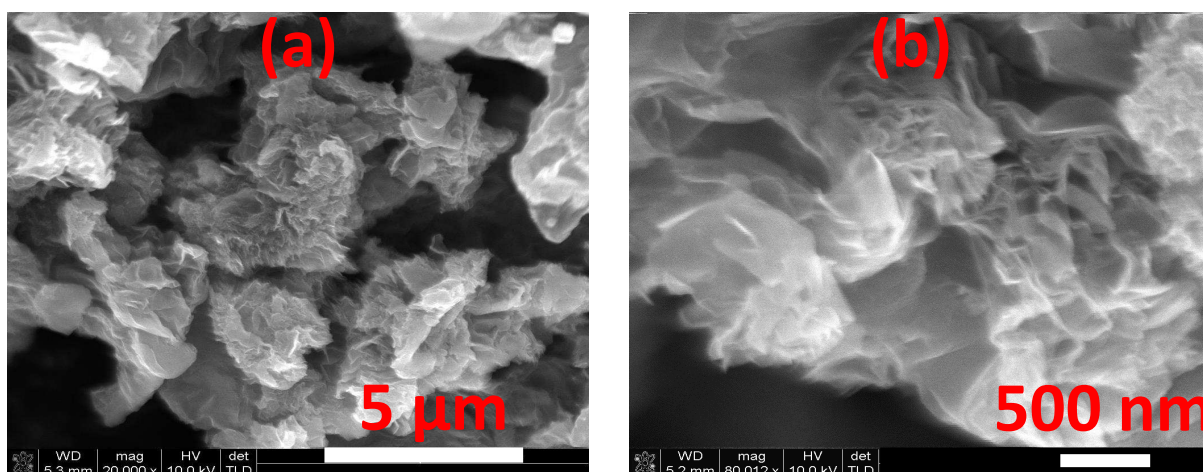


Fig. 7.3 FE-SEM images of MoSe₂/rGO nanosheets at (a) lower and (b) higher magnifications.

shows the survey spectrum of the MoSe₂/reduced graphene oxide nanosheets. The wide scan XPS spectrum confirmed the existence of Mo, Se, and C in the corresponding oxidation states for the MoSe₂/rGO hybrid structure. The presence of O in the sample may be due to surface-adsorbed CO₂ and O₂ [37]. The core-level spectrum of the Mo 3d spin orbital (Fig. 7.4b) was split into two well defined peaks of the 3d_{5/2} and 3d_{3/2} states at respective binding energies of 228.6 and 231.7 eV, which confirms that molybdenum was in the tetravalent state [23, 34, 35, 38]. The Se 3d core-level spectrum (Fig. 7.4c) shows peaks located at 54.2 and 54.9 eV that can be assigned to the 3d_{5/2} and 3d_{3/2} spin orbit couple, indicative of the divalent state of Se in MoSe₂ [23, 34, 35, 38]. Figure 7.4d displays the C 1s core-level spectrum of the MoSe₂/rGO nanosheets. The main peak appearing at 284.4 eV corresponds to the non-oxygenated carbon (C–C). There are no additional peaks related to the C–O (hydroxyl groups), C=O (carbonyl groups), and O–C=O (carboxyl groups) in the C1s spectrum, which confirms complete reduction of most of the oxygen-containing functional groups (fully removed) during the high temperature hydrothermal

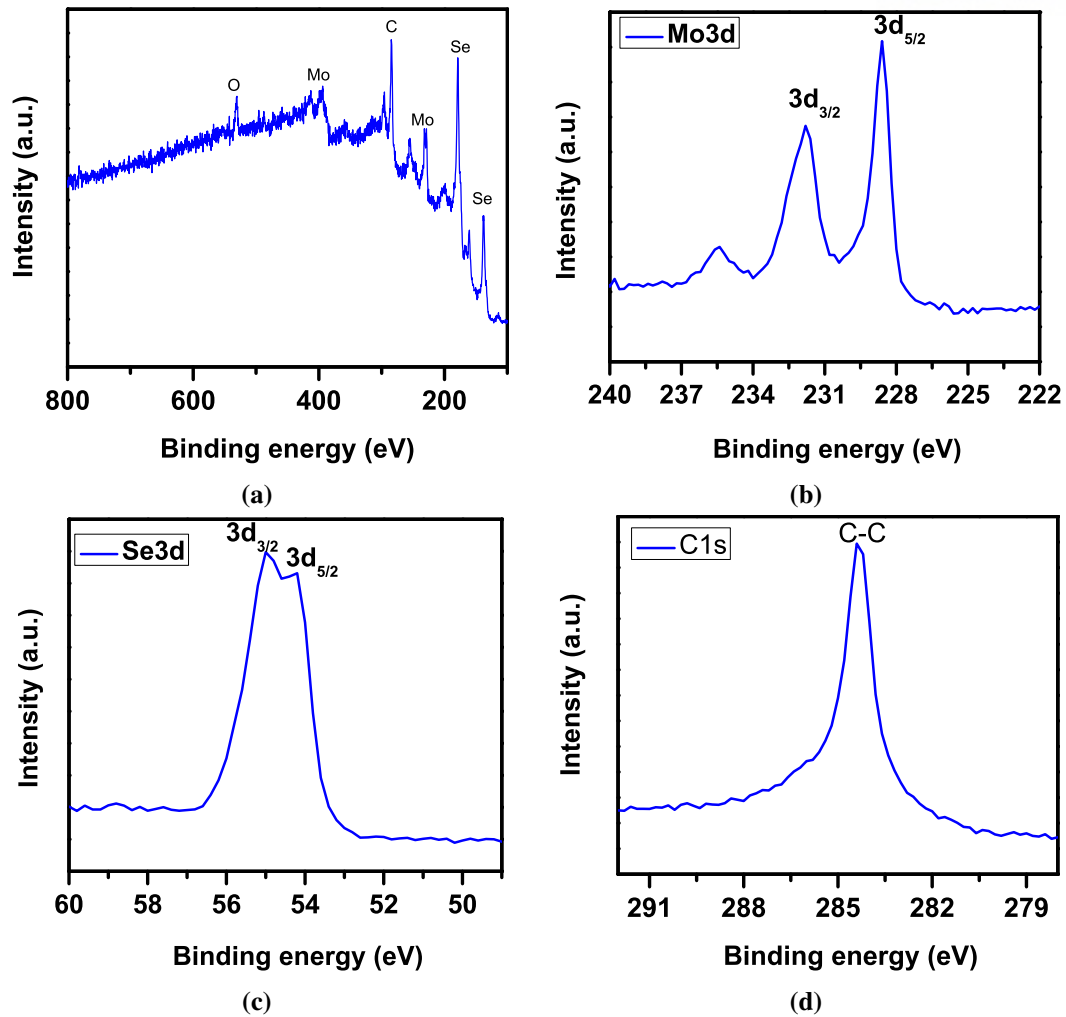


Fig. 7.4 XPS spectra of MoSe₂/reduced graphene oxide nanosheets (a) survey, (b) Mo 3d, (c) Se 3d, and (d) C 1s .

process [37]. These results further verified the formation of the MoSe₂/rGO nanosheets.

7.3.2 Electrochemical performance of MoSe₂/rGO and MoSe₂ electrodes

The electrochemical performance of the MoSe₂ and MoSe₂/rGO nanosheet electrodes was evaluated using cyclic voltammetry, galvanostatic charge/discharge, and electrochemical impedance spectroscopy techniques in 0.5 M H₂SO₄ electrolyte. Figure 7.5 presents a comparison of the CV curves of the MoSe₂ and MoSe₂/rGO nanosheet electrodes, acquired at a scan rate of 25 mV s⁻¹. Both CV curves clearly exhibited a near rectangular shape, indicating EDLC behavior. A pair of redox peaks was also observed, corresponding to the reversible redox reaction of Mo active atoms (from MoSe₂) with the electrolyte ions, indicating pseudocapacitance behavior as represented in Eqn.(7.1) [24].



Compared with the CV curve of MoSe₂, the MoSe₂/rGO electrode showed a larger integrated area, indicating the higher specific capacitance of the composite. This enhanced electrochemical charge storage

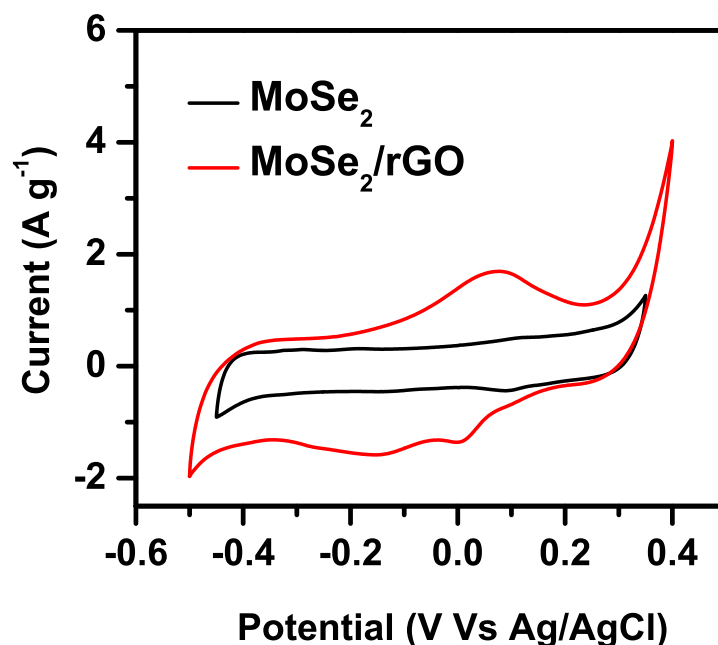


Fig. 7.5 Cyclic voltammetry curves of MoSe₂ and MoSe₂/rGO nanosheets electrodes at a scan rate of 25 mV s⁻¹.

behavior might be due to the synergistic effect of MoSe₂ and reduced graphene oxide. The CV profiles of the MoSe₂/rGO electrode acquired at various scan rates are shown in Fig. 7.6. Increasing the scan rate led to an increase in the area of the CV curves and the peak current density with retention of the deviated rectangular shape; a pair of redox peaks was still clearly apparent, even at the high scan rate of 125 mV s⁻¹, with no obvious distortion. The specific capacitance of the MoSe₂ and MoSe₂/rGO nanosheet electrodes was calculated from the CV curves using Eq.(2.1). The specific capacitance as a function of the scan rate is shown in Fig. 7.7. At the scan rate of 5 mV s⁻¹, the specific capacitance values of the MoSe₂ and MoSe₂/rGO nanosheets were 67 and 211 F g⁻¹, respectively. The enhanced electrochemical performance of the MoSe₂/rGO nanosheets is mainly attributed to the following features: (i) the hybrid nanostructure provides more electroactive sites for charge storage via electric double layer capacitance (EDLC) as well as pseudocapacitance (Faradaic reaction), (ii) MoSe₂ anchored on the rGO nanosheets effectively reduced agglomeration of the electroactive materials and also reduced the internal resistance, thereby enhancing the electronic conductivity of the electrode materials for fast charge transport.

Further, the capacitive behavior for real-time application of the as-prepared electrode materials was demonstrated in galvanostatic charge/discharge tests. Figure 7.8 shows the GCD curves of the MoSe₂ and MoSe₂/rGO nanosheet electrodes at 0.5 A g⁻¹ in 0.5 M H₂SO₄ electrolyte. The charge/discharge curves clearly have a nearly triangular shape with a voltage plateau (slight deviation from linearity), indicating the contribution of electrical double layer capacitance as well as pseudocapacitance, which is consistent with the CV results. Furthermore, at a constant current density, the MoSe₂/rGO nanosheet electrodes have a higher discharge time than pristine MoSe₂, as expected, which indicates the large storage capacity of the electrode material. The galvanostatic charge/discharge curves of the MoSe₂/rGO nanosheet electrodes at various current densities are presented in Fig. 7.9. All of the charge/discharge profiles displayed an almost

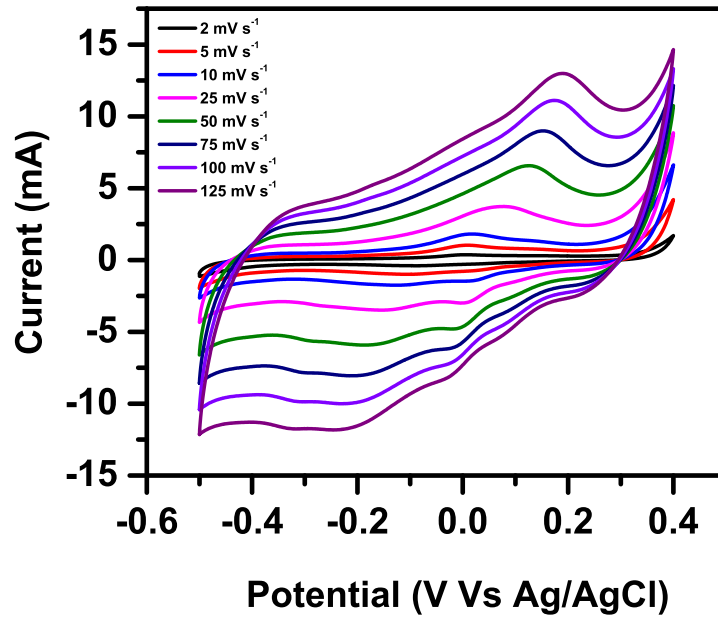


Fig. 7.6 CV curves of MoSe₂/rGO nanosheets electrode at various scan rates

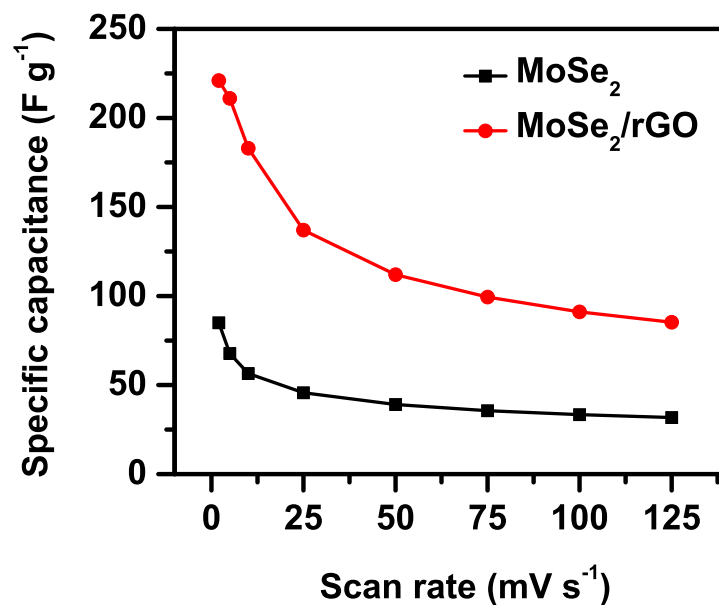


Fig. 7.7 Specific capacitance of MoSe₂ and MoSe₂/rGO nanosheets electrodes at different scan rates.

triangular shape with slight distortion from linearity, demonstrating that the hybrid material exhibited better electrochemical charge storage behavior via both the EDLC and pseudocapacitance mechanisms.

The specific capacitance of the as-prepared electrodes could be calculated from the GCD using eqn.(2.2). Based on the discharge time, the calculated specific capacitance values of the MoSe₂ and MoSe₂/rGO nanosheet electrodes were 13 and 29 F g⁻¹ at the current density of 0.5 A g⁻¹, respectively. Moreover, the relationship between the specific capacitance and current density is shown in Fig. 7.10. The specific capacitance of the MoSe₂/rGO nanosheet electrode was clearly enhanced relative to that of pristine MoSe₂ at all the current densities, which is ascribed to the higher electrical conductivity and electrical double layer charge storage nature of rGO in addition to the redox (pseudocapacitance) behavior of

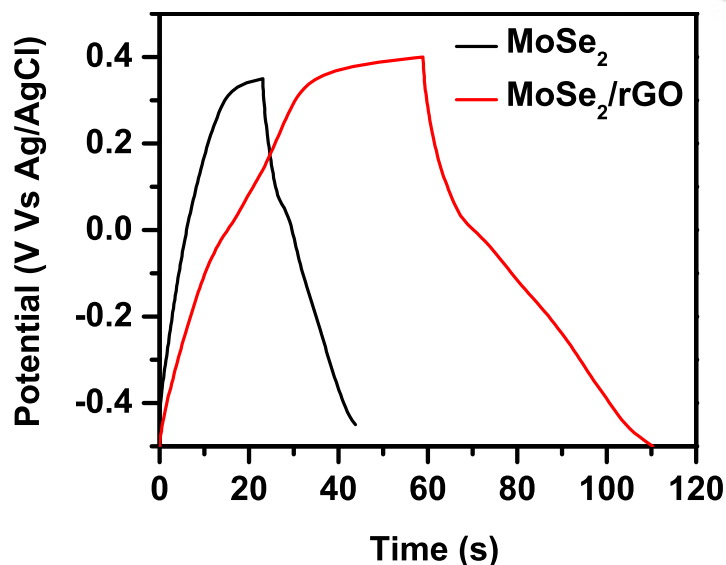


Fig. 7.8 Galvanostatic charge-discharge curves of MoSe₂ and MoSe₂/rGO nanosheets electrodes.

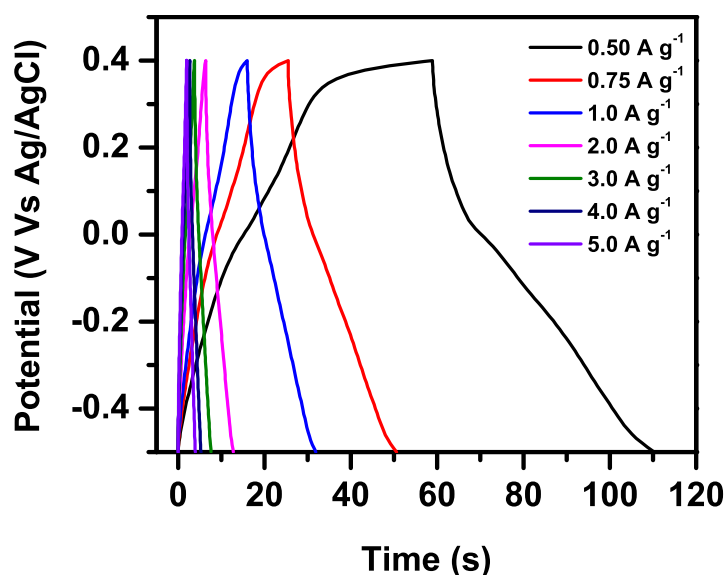


Fig. 7.9 GCD curves of MoSe₂/rGO nanosheets electrode at different current densities.

MoSe₂. The specific capacitance decreased as the current density increased from 0.5 to 5 A g⁻¹. This may be due to the insufficient time available for diffusion of the electrolyte ions into the inner electrode surface (kinetics of mass-transport limitation) [39, 40].

Long-term cycling stability is a crucial parameter for utilization of the electrode material for real-time application in supercapacitors. The cycling stability of the MoSe₂/rGO nanosheet electrode was measured by repeating the charge/discharge test at a current density of 5 A g⁻¹ for 10,000 cycles, as shown in Fig. 7.11. The capacitance retention gradually decreased over the initial 4000 cycles, after which, interestingly, the capacitance retention increased continuously upon repeated cycling up to 10,000 cycles. The initial decrease of the capacitance may be due to the loss of a few loosely attached nanosheets or dissolution of some of the pseudocapacitive electroactive materials during the repeated cycling. The increasing trend beyond 4000 cycles may be due to "electroactivation" of the two-dimensional active

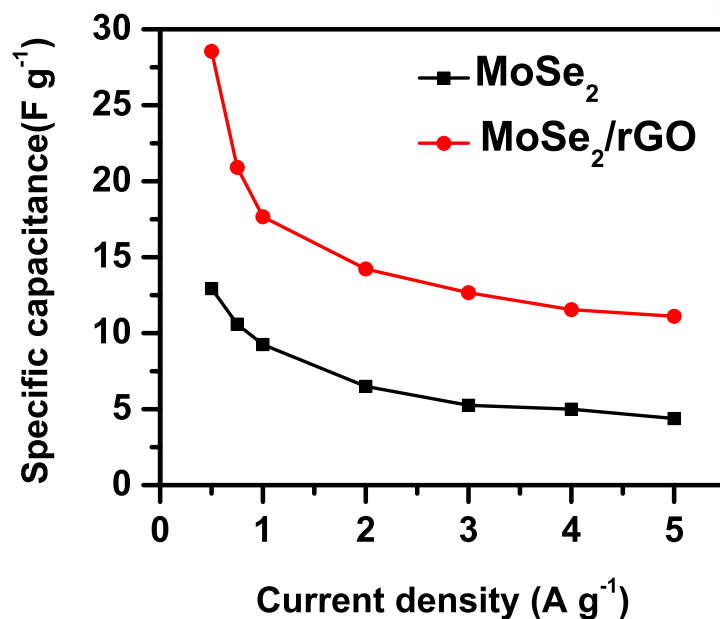


Fig. 7.10 Specific capacitance vs. current density of MoSe₂/rGO nanosheets electrode.

materials (rGO and/or MoSe₂) via continuous intercalation/deintercalation of the electrolyte ions, resulting in partial re-exfoliation, which also provides a large surface area for electrochemical charge storage. This partial re-exfoliation process causes a continuous increase in the specific capacitance with repeated charge/discharge cycling. A similar "electroactivation" process and increasing capacitance retention trend has previously been observed in graphene and MoS₂-based supercapacitor materials [27, 41–43]. After 10,000 cycles, the MoSe₂/rGO nanosheet electrode retained 180% of its initial specific capacitance, which demonstrates that the electroactive material has good cycling stability and reversibility during the repetitive charge-discharge cycling process. The inset of Fig. 7.11 presents the charge/discharge curves of the first and last four cycles of the 10,000 cycles. It can be seen the charge/discharge profiles display a linear and symmetrical shape in the first and last four cycles of the 10,000 cycles, further confirming the better capacitive behavior and electrochemical reversibility of the composite.

In order to further understand the cycling stability and fundamental behavior of the as-prepared electroactive materials, EIS analyses were performed before and after the cycle test of the MoSe₂/rGO nanosheets and pristine MoSe₂ electrodes. Figure 7.12 shows the Nyquist plots for pristine MoSe₂ and the MoSe₂/rGO nanosheets before and after 10,000 cycling tests. In the high-frequency region, the x-intercept at the beginning of the semicircle on the Z-real axis represents the equivalent series resistance (ESR), including the electrolyte resistance, contact resistance at the interface between the electro-active material and substrate, and intrinsic resistance of the electro-active material [44, 45]. The ESR of the pristine MoSe₂ and MoSe₂/rGO nanosheets before and after the cycling tests were estimated to be 1.16, 0.96, and 0.98 Ω, respectively. Further, all the curves consist of a semi-circular arc in the high-medium frequency region, followed by an inclined line in the low frequency region. The semi-circle in the high-medium frequency region is related to the charge transfer resistance (R_{ct}) at the electrode/electrolyte interface, and the inclined line in the low frequency region corresponds to the diffusive resistance of electrolyte ions inside the electrode materials (Warburg impedance) [3, 46, 47]. The respective charge transfer

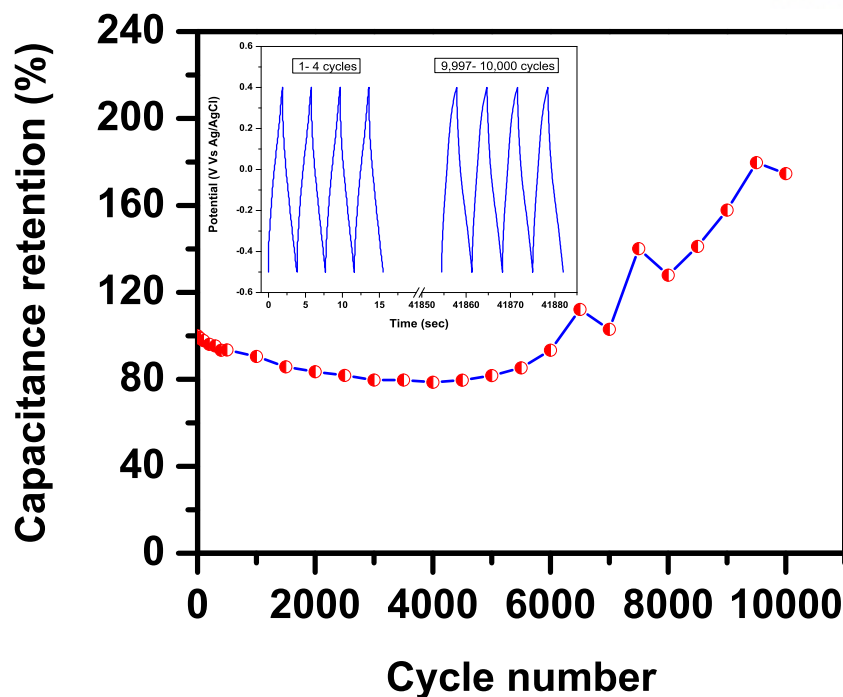


Fig. 7.11 Cycling performance of MoSe₂/rGO nanosheets electrode at 5 A g⁻¹ for 10,000 cycles. The inset shows the charge-discharge curves of the initial and the final four cycles.

resistance values of the MoSe₂ and MoSe₂/rGO nanosheet electrodes were 3.86 and 1.64 Ω. Compared to MoSe₂, the MoSe₂/rGO nanosheet electrode exhibited lower ESR and R_{ct} values, indicating the higher electrical conductivity of the composite electrode. After 10,000 cycles, the R_{ct} value of the MoSe₂/rGO nanosheet electrode decreased to 0.47 Ω, which demonstrates higher electrical conductivity and better charge transport of electrolyte ions by the composite. Furthermore, the inclined line in the low frequency region is almost perpendicular to the real axis, indicating the near-ideal capacitive behavior [48]. These results confirmed the better electronic conductivity and cycling stability of the as-prepared MoSe₂/rGO nanosheet electrode.

7.4 Summary

In summary, we successfully synthesized MoSe₂/rGO nanosheet composites via a facile hydrothermal method. The MoSe₂/rGO hybrid nanostructure exhibited improved electrochemical performance in terms of the specific capacitance (211 F g⁻¹ at 5 mV s⁻¹) and enhanced cyclic stability (180% capacitance retention for 10,000 cycles) relative to pristine MoSe₂. The enhanced electrochemical performance of the MoSe₂/rGO electrode is mainly attributed to the combined effects of pseudocapacitance and EDLC. Further, the hybrid nanostructure provides more electroactive sites for charge storage, higher electrical conductivity, and a short ion/electron diffusion path length for fast charge transport, which ensures excellent electrochemical performance and in turn high charge storage capacity. These results suggest that the MoSe₂/rGO hybrid nanostructure has great potential for application in high performance supercapacitor devices.

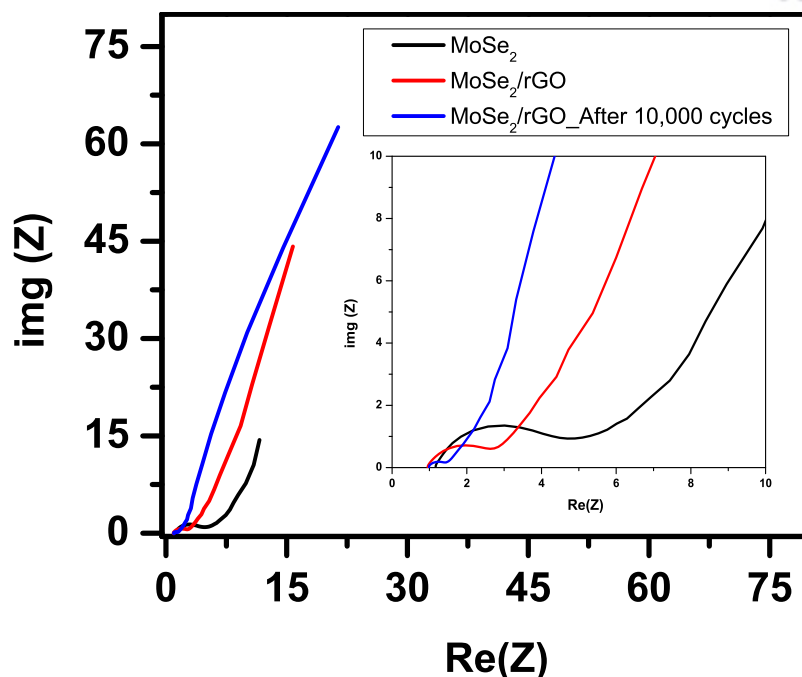


Fig. 7.12 Nyquist plots of MoSe₂ and MoSe₂/rGO nanosheets at the initial cycle and after 10000 cycles. The inset indicates the magnified portion of the high-frequency EIS.

References

- [1] Frackowiak, E., Carbon materials for supercapacitor application, *Physical Chemistry Chemical Physics* 2007, 9 (15), 1774–1785. doi:[10.1039/B618139M](https://doi.org/10.1039/B618139M).
- [2] Shao, Y., El-Kady, M.F., Wang, L.J., Zhang, Q., Li, Y., Wang, H., Mousavi, M.F., Kaner, R.B., Graphene-based materials for flexible supercapacitors, *Chemical Society Reviews* 2015, 44 (11), 3639–3665. doi:[10.1039/C4CS00316K](https://doi.org/10.1039/C4CS00316K).
- [3] Zhang, L.L., Zhao, X.S., Carbon-based materials as supercapacitor electrodes, *Chemical Society Reviews* 2009, 38 (9), 2520–2531. doi:[10.1039/B813846J](https://doi.org/10.1039/B813846J).
- [4] Zhang, X., Zhang, H., Li, C., Wang, K., Sun, X., Ma, Y., Recent advances in porous graphene materials for supercapacitor applications, *RSC Advances* 2014, 4 (86), 45862–45884. doi:[10.1039/C4RA07869A](https://doi.org/10.1039/C4RA07869A).
- [5] Barbieri, O., Hahn, M., Herzog, A., Kotz, R., Capacitance limits of high surface area activated carbons for double layer capacitors, *Carbon* 2005, 43 (6), 1303–1310. doi:[10.1016/j.carbon.2005.01.001](https://doi.org/10.1016/j.carbon.2005.01.001).
- [6] Zhu, Y., Murali, S., Stoller, M.D., Ganesh, K.J., Cai, W., Ferreira, P.J., Pirkle, A., Wallace, R.M., Cychosz, K.A., Thommes, M., Su, D., Stach, E.A., Ruoff, R.S., Carbon-based supercapacitors produced by activation of graphene, *Science* 2011, 332 (6037), 1537–1541. doi:[10.1126/science.1200770](https://doi.org/10.1126/science.1200770).

- [7] Lang, X., Hirata, A., Fujita, T., Chen, M., Nanoporous metal/oxide hybrid electrodes for electrochemical supercapacitors, *Nature Nanotechnology* 2011, 6 (4), 232–236. doi:[10.1038/nnano.2011.13](https://doi.org/10.1038/nnano.2011.13).
- [8] Lokhande, C.D., Dubal, D.P., Joo, O.S., Metal oxide thin film based supercapacitors, *Current Applied Physics* 2011, 11 (3), 255–270. doi:[10.1016/j.cap.2010.12.001](https://doi.org/10.1016/j.cap.2010.12.001).
- [9] Faraji, S., Ani, F.N., Microwave-assisted synthesis of metal oxide/hydroxide composite electrodes for high power supercapacitors – a review, *Journal of Power Sources* 2014, 263, 338 – 360. doi:[10.1016/j.jpowsour.2014.03.144](https://doi.org/10.1016/j.jpowsour.2014.03.144).
- [10] Shi, F., Li, L., Wang, X.L., Gu, C.d., Tu, J.p., Metal oxide/hydroxide-based materials for supercapacitors, *RSC Advances* 2014, 4 (79), 41910–41921. doi:[10.1039/C4RA06136E](https://doi.org/10.1039/C4RA06136E).
- [11] Yang, Q., Lu, Z., Liu, J., Lei, X., Chang, Z., Luo, L., Sun, X., Metal oxide and hydroxide nanoarrays: Hydrothermal synthesis and applications as supercapacitors and nanocatalysts, *Progress in Natural Science: Materials International* 2013, 23 (4), 351–366. doi:[10.1016/j.pnsc.2013.06.015](https://doi.org/10.1016/j.pnsc.2013.06.015).
- [12] Snook, G.A., Kao, P., Best, A.S., Conducting-polymer-based supercapacitor devices and electrodes, *Journal of Power Sources* 2011, 196 (1), 1–12. doi:[10.1016/j.jpowsour.2010.06.084](https://doi.org/10.1016/j.jpowsour.2010.06.084).
- [13] Chia, X., Eng, A.Y.S., Ambrosi, A., Tan, S.M., Pumera, M., Electrochemistry of nanostructured layered transition-metal dichalcogenides, *Chemical Reviews* 2015, 115 (21), 11941–11966. doi:[10.1021/acs.chemrev.5b00287](https://doi.org/10.1021/acs.chemrev.5b00287).
- [14] Pumera, M., Sofer, Z., Ambrosi, A., Layered transition metal dichalcogenides for electrochemical energy generation and storage, *Journal of Materials Chemistry A* 2014, 2 (24), 8981–8987. doi:[10.1039/C4TA00652F](https://doi.org/10.1039/C4TA00652F).
- [15] Xiong, G., He, P., Liu, L., Chen, T., Fisher, T.S., Plasma-grown graphene petals templating Ni-Co-Mn hydroxide nanoneedles for high-rate and long-cycle-life pseudocapacitive electrodes, *Journal of Materials Chemistry A* 2015, 3 (45), 22940–22948. doi:[10.1039/C5TA05441A](https://doi.org/10.1039/C5TA05441A).
- [16] Zhi, M., Xiang, C., Li, J., Li, M., Wu, N., Nanostructured carbon-metal oxide composite electrodes for supercapacitors: a review, *Nanoscale* 2013, 5 (1), 72–88. doi:[10.1039/C2NR32040A](https://doi.org/10.1039/C2NR32040A).
- [17] Butler, S.Z., Hollen, S.M., Cao, L., Cui, Y., Gupta, J.A., Gutierrez, H.R., Heinz, T.F., Hong, S.S., Huang, J., Ismach, A.F., Johnston Halperin, E., Kuno, M., Plashnitsa, V.V., Robinson, R.D., Ruoff, R.S., Salahuddin, S., Shan, J., Shi, L., Spencer, M.G., Terrones, M., Windl, W., Goldberger, J.E., Progress, challenges, and opportunities in two-dimensional materials beyond graphene, *ACS Nano* 2013, 7 (4), 2898–2926. doi:[10.1021/nn400280c](https://doi.org/10.1021/nn400280c).
- [18] Ramadoss, A., Kim, T., Kim, G.S., Kim, S.J., Enhanced activity of a hydrothermally synthesized mesoporous MoS₂ nanostructure for high performance supercapacitor applications, *New Journal of Chemistry* 2014, 38 (6), 2379–2385. doi:[10.1039/C3NJ01558K](https://doi.org/10.1039/C3NJ01558K).
- [19] Wang, H., Yuan, H., Sae Hong, S., Li, Y., Cui, Y., Physical and chemical tuning of two-dimensional transition metal dichalcogenides, *Chemical Society Reviews* 2015, 44 (9), 2664–2680. doi:[10.1039/C4CS00287C](https://doi.org/10.1039/C4CS00287C).

- [20] Ko, Y.N., Choi, S.H., Park, S.B., Kang, Y.C., Hierarchical MoSe₂ yolk-shell microspheres with superior Na-ion storage properties, *Nanoscale* 2014, 6 (18), 10511–10515. doi:[10.1039/C4NR02538E](https://doi.org/10.1039/C4NR02538E).
- [21] Zhang, Z., Fu, Y., Yang, X., Qu, Y., Zhang, Z., Hierarchical MoSe₂ nanosheets/reduced graphene oxide composites as anodes for lithium-ion and sodium-ion batteries with enhanced electrochemical performance, *ChemNanoMat* 2015, 1 (6), 409–414. doi:[10.1002/cnma.201500097](https://doi.org/10.1002/cnma.201500097).
- [22] Chen, H., Xie, Y., Cui, H., Zhao, W., Zhu, X., Wang, Y., Lu, X., Huang, F., In situ growth of a MoSe₂/Mo counter electrode for high efficiency dye-sensitized solar cells, *Chemical Communications* 2014, 50 (34), 4475–4477. doi:[10.1039/C3CC49600G](https://doi.org/10.1039/C3CC49600G).
- [23] Tang, H., Dou, K., Kaun, C.C., Kuang, Q., Yang, S., MoSe₂ nanosheets and their graphene hybrids: synthesis, characterization and hydrogen evolution reaction studies, *Journal of Materials Chemistry A* 2014, 2 (2), 360–364. doi:[10.1039/C3TA13584E](https://doi.org/10.1039/C3TA13584E).
- [24] Balasingam, S.K., Lee, J.S., Jun, Y., Few-layered MoSe₂ nanosheets as an advanced electrode material for supercapacitors, *Dalton Transactions* 2015, 44 (35), 15491–15498. doi:[10.1039/C5DT01985K](https://doi.org/10.1039/C5DT01985K).
- [25] Huang, K.J., Zhang, J.Z., Cai, J.L., Preparation of porous layered molybdenum selenide-graphene composites on Ni foam for high-performance supercapacitor and electrochemical sensing, *Electrochimica Acta* 2015, 180, 770–777. doi:[10.1016/j.electacta.2015.09.016](https://doi.org/10.1016/j.electacta.2015.09.016).
- [26] Huang, K.J., Zhang, J.Z., Fan, Y., Preparation of layered MoSe₂ nanosheets on Ni-foam substrate with enhanced supercapacitor performance, *Materials Letters* 2015, 152, 244–247. doi:[10.1016/j.matlet.2015.03.130](https://doi.org/10.1016/j.matlet.2015.03.130).
- [27] Shi, Y., Hua, C., Li, B., Fang, X., Yao, C., Zhang, Y., Hu, Y.S., Wang, Z., Chen, L., Zhao, D., Stucky, G.D., Highly ordered mesoporous crystalline MoSe₂ material with efficient visible-light-driven photocatalytic activity and enhanced lithium storage performance, *Advanced Functional Materials* 2013, 23 (14), 1832–1838. doi:[10.1002/adfm.201202144](https://doi.org/10.1002/adfm.201202144).
- [28] Cao, X., Yin, Z., Zhang, H., Three-dimensional graphene materials: preparation, structures and application in supercapacitors, *Energy & Environmental Science* 2014, 7 (6), 1850–1865. doi:[10.1039/C4EE00050A](https://doi.org/10.1039/C4EE00050A).
- [29] He, Y., Chen, W., Gao, C., Zhou, J., Li, X., Xie, E., An overview of carbon materials for flexible electrochemical capacitors, *Nanoscale* 2013, 5 (19), 8799–8820. doi:[10.1039/C3NR02157B](https://doi.org/10.1039/C3NR02157B).
- [30] Li, A., Liu, J., Feng, S., Applications of graphene based materials in energy and environmental science, *Science of Advanced Materials* 2014, 6 (2), 209–234. doi:[10.1166/sam.2014.1706](https://doi.org/10.1166/sam.2014.1706).
- [31] Yuan, W., Chen, J., Shi, G., Nanoporous graphene materials, *Materials Today* 2014, 17 (2), 77 – 85. doi:[10.1016/j.mattod.2014.01.021](https://doi.org/10.1016/j.mattod.2014.01.021).
- [32] Lee, M., Balasingam, S.K., Jeong, H.Y., Hong, W.G., Lee, H.B.R., Kim, B.H., Jun, Y., One-step hydrothermal synthesis of graphene decorated V₂O₅ nanobelts for enhanced electrochemical energy storage, *Scientific Reports* 2015, 5, 8151. doi:[10.1038/srep08151](https://doi.org/10.1038/srep08151).

- [33] Ramadoss, A., Kim, S.J., Improved activity of a graphene-TiO₂ hybrid electrode in an electrochemical supercapacitor, *Carbon* 2013, 63, 434 – 445. doi:[10.1016/j.carbon.2013.07.006](https://doi.org/10.1016/j.carbon.2013.07.006).
- [34] Guo, J., Shi, Y., Bai, X., Wang, X., Ma, T., Atomically thin MoSe₂/graphene and WSe₂/graphene nanosheets for the highly efficient oxygen reduction reaction, *Journal of Materials Chemistry A* 2015, 3, 24397–24404. doi:[10.1039/C5TA06909B](https://doi.org/10.1039/C5TA06909B).
- [35] Bi, E., Chen, H., Yang, X., Ye, F., Yin, M., Han, L., Fullerene-structured MoSe₂ hollow spheres anchored on highly nitrogen-doped graphene as a conductive catalyst for photovoltaic applications, *Scientific Reports* 2015, 5, 13214. doi:[10.1038/srep13214](https://doi.org/10.1038/srep13214).
- [36] Wu, Y., Liu, S., Wang, H., Wang, X., Zhang, X., Jin, G., A novel solvothermal synthesis of Mn₃O₄/graphene composites for supercapacitors, *Electrochimica Acta* 2013, 90, 210–218. doi:[10.1016/j.electacta.2012.11.124](https://doi.org/10.1016/j.electacta.2012.11.124).
- [37] Huang, K.J., Zhang, J.Z., Liu, Y., Liu, Y.M., Synthesis of reduced graphene oxide wrapped-copper sulfide hollow spheres as electrode material for supercapacitor, *International Journal of Hydrogen Energy* 2015, 40 (32), 10158–10167. doi:[10.1016/j.ijhydene.2015.05.152](https://doi.org/10.1016/j.ijhydene.2015.05.152).
- [38] Wang, H., Kong, D., Johanes, P., Cha, J.J., Zheng, G., Yan, K., Liu, N., Cui, Y., MoSe₂ and WSe₂ nanofilms with vertically aligned molecular layers on curved and rough surfaces, *Nano Letters* 2013, 13 (7), 3426–3433. doi:[10.1021/nl401944f](https://doi.org/10.1021/nl401944f).
- [39] Ramadoss, A., Kim, G.S., Kim, S.J., Fabrication of reduced graphene oxide/TiO₂ nanorod/reduced graphene oxide hybrid nanostructures as electrode materials for supercapacitor applications, *CrysoComm* 2013, 15 (47), 10222–10229. doi:[10.1039/C3CE41517A](https://doi.org/10.1039/C3CE41517A).
- [40] Wang, J., Gao, Z., Li, Z., Wang, B., Yan, Y., Liu, Q., Mann, T., Zhang, M., Jiang, Z., Green synthesis of graphene nanosheets/ZnO composites and electrochemical properties, *Journal of Solid State Chemistry* 2011, 184 (6), 1421–1427. doi:[10.1016/j.jssc.2011.03.006](https://doi.org/10.1016/j.jssc.2011.03.006).
- [41] Bissett, M.A., Kinloch, I.A., Dryfe, R.A.W., Characterization of MoS₂ graphene composites for high performance coin cell supercapacitors, *ACS Applied Materials & Interfaces* 2015, 7 (31), 17388–17398. doi:[10.1021/acsami.5b04672](https://doi.org/10.1021/acsami.5b04672).
- [42] Cheng, Q., Tang, J., Ma, J., Zhang, H., Shinya, N., Qin, L.C., Graphene and carbon nanotube composite electrodes for supercapacitors with ultra-high energy density, *Physical Chemistry Chemical Physics* 2011, 13 (39), 17615–17624. doi:[10.1039/C1CP21910C](https://doi.org/10.1039/C1CP21910C).
- [43] Cheng, Q., Tang, J., Ma, J., Zhang, H., Shinya, N., Qin, L.C., Graphene and nanostructured MnO₂ composite electrodes for supercapacitors, *Carbon* 2011, 49 (9), 2917–2925. doi:[10.1016/j.carbon.2011.02.068](https://doi.org/10.1016/j.carbon.2011.02.068).
- [44] Yan, J., Fan, Z., Wei, T., Qian, W., Zhang, M., Wei, F., Fast and reversible surface redox reaction of graphene MnO₂ composites as supercapacitor electrodes, *Carbon* 2010, 48 (13), 3825–3833. doi:[10.1016/j.carbon.2010.06.047](https://doi.org/10.1016/j.carbon.2010.06.047).

- [45] Zhang, W., Lin, H., Lin, Z., Yin, J., Lu, H., Liu, D., Zhao, M., 3-d hierarchical porous carbon for supercapacitors prepared from lignin through a facile template-free method, *ChemSusChem* 2015, 8 (12), 2114–2122. doi:[10.1002/cssc.201403486](https://doi.org/10.1002/cssc.201403486).
- [46] Jin, G., Xiao, X., Li, S., Zhao, K., Wu, Y., Sun, D., Wang, F., Strongly coupled graphene/Mn₃O₄ composite with enhanced electrochemical performance for supercapacitor electrode, *Electrochimica Acta* 2015, 178, 689–698. doi:[10.1016/j.electacta.2015.08.032](https://doi.org/10.1016/j.electacta.2015.08.032).
- [47] Niu, L., Wang, J., Hong, W., Sun, J., Fan, Z., Ye, X., Wang, H., Yang, S., Solvothermal synthesis of Ni/reduced graphene oxide composites as electrode material for supercapacitors, *Electrochimica Acta* 2014, 123, 560–568. doi:[10.1016/j.electacta.2014.01.005](https://doi.org/10.1016/j.electacta.2014.01.005).
- [48] Kim, T.Y., Lee, H.W., Stoller, M., Dreyer, D.R., Bielawski, C.W., Ruoff, R.S., Suh, K.S., High-performance supercapacitors based on poly(ionic liquid)-modified graphene electrodes, *ACS Nano* 2011, 5 (1), 436–442. doi:[10.1021/nn101968p](https://doi.org/10.1021/nn101968p).

Amorphous MoSe_x Nanostructures Coated Carbon Fiber Paper

8.1 Introduction

Traditional carbon based capacitors are best known for their high power density, still their energy density is low. In order to obtain both high power and energy density in a single device, supercapacitors (also known as ultracapacitors or electrochemical double-layer capacitors, EDLC) are developed by researchers with the combination of double layer capacitance materials with the redox active pseudocapacitance materials [1]. Carbon based materials provide double layer capacitance to the traditional capacitors. Redox active materials provide pseudocapacitance (faradaic behaviour), which is the key factor to obtain the high energy density in supercapacitors. Various redox active materials such as transition metal oxides, transition metal hydroxides, transition metal dichalcogenides, conducting polymer etc. have been investigated [2–7]. Of these transition metal dichalcogenides (TMDC) have attracted many researchers due to its superior electronic, magnetic and electrochemical properties [8]. Various TMDC class of materials such as MoS_2 , WS_2 , SnS , NiS , Ni_3S_2 , VS_2 , MoSe_2 , WeS_2 , etc. have been investigated as active materials for supercapacitor applications [4, 9]. To the best of our knowledge, a few number of articles only published on molybdenum selenide based materials for supercapacitor applications [8, 10, 11]. Therefore, the combination of carbon based materials with the redox active molybdenum selenide based pseudocapacitance materials provide high energy and power density in supercapacitors. Moreover a highly conducting carbon based materials increase the conductivity and reduces the IR drop. So far many different carbon based materials such as activated carbon, graphite, carbon nanotube and graphene have been investigated either individually or mixed with the redox active materials to get higher performance [12]. Usually, the electrode materials are mixed with the polymeric binder to make a proper adhesion on the conducting substrate. In general metal foil based current collectors are used as a highly conducting substrate. The binder and the heavy metal substrates have a bottle neck that gravimetric specific capacitance of the final product is reduced, which prevent the commercialization of supercapacitors from the practical applications [13, 14]. Also the polymeric binders are usually ionic conductors, therefore electrical resistance of the electrode increases which in turn affect the electrochemical reaction kinetics. In this article, we have employed a binder free deposition of amorphous molybdenum selenide on the three dimensional (3-D) carbon fiber paper (CFP) substrate via facile hydrothermal route. CFP has a light weight, high conductivity and chemical stability. Moreover, 3-D network structure provides high porosity which enhances the surface area for the effective loading of electrode materials.

8.2 Experimental

8.2.1 Synthesis of amorphous MoSe_x nanostructures coated carbon fiber paper

The precursors sodium molybdate (Na₂MoO₄ · 2 H₂O), selenium powder (Se) and sodium borohydride (NaBH₄) were purchased from Sigma Aldrich (ACS grade) and used without further purification. In a typical hydrothermal synthesis, exactly 1.32 g of Na₂MoO₄ · 2 H₂O, 1.24 g of Se and 0.4 g of NaBH₄ were weighed and dissolved in 80 ml of DI water. The mixture was continuously stirred until to get red color solution, which is an indication of uniform distribution of selenium metal powder. The low weight, three-dimensional carbon fiber paper was used as a substrate. The as purchased CFP is hydrophobic in nature. The hydrophobicity of CFP should be converted into hydrophilic to make a uniform contact of precursor solution with the substrate by the plasma cleaning. The appropriate dimension of CFP was placed into the chamber and then activated with the oxygen plasma for 15 minutes. This plasma cleaned carbon fiber paper was abbreviated as PC-CFP. Also, another CFP with different geometrical dimension was pretreated using electrochemical method. In a conventional three-electrode setup, 1 M H₂SO₄ was used as electrolyte, CFP was used as a working electrode, Ag/AgCl and large area Pt-gauze were used as reference electrode and counter electrode, respectively. The electrochemical pretreatment was conducted via potentiostatic method at a constant voltage of 2 V for 10 min. This electrochemically etched CFP is abbreviated as EE-CFP. The both pre-treated PC-CFP and EE-CFP were placed into the same Teflon-lined stainless steel autoclave. The previously prepared precursor solution was transferred into the autoclave, sealed tightly and then placed inside the electric oven. The hydrothermal reaction was carried out at 200 °C for 12 h, after that the autoclave was turned off and wait for few hours until it cooled down naturally to room temperature. After that, amorphous MoSe_x coated PC-CFP (PC-CFP/a-MoSe_x) and amorphous MoSe_x coated EE-CFP (EE-CFP/a-MoSe_x) were taken out and washed with DI water for several times in order to remove the residuals and then finally both MoSe_x coated CFPs were dried at 40 °C for few hours in an electric oven.

8.2.2 Materials characterization

The crystal structure of the as-prepared sample was analyzed using an X-ray diffractometer (XRD, Rigaku) with Cu K α radiation ($\lambda = 0.15141$ nm) and Raman spectroscopy (WITec) using 532 nm laser excitation, after calibrating the Raman shift with a silicon reference at 521 cm⁻¹. The surface morphology of the hybrid nanostructure was examined by field emission scanning electron microscopy (FE-SEM, Nano230, FEI Co.). The chemical composition of the sample was examined using X-ray photoelectron spectroscopy with Al K α radiation (XPS, Thermo Fisher, UK).

8.2.3 Cell fabrication and electrochemical characterization

An exactly 1 cm² (1cm x 1cm) area of MoSe_x coated CFP was used as a single electrode. The two electrodes were sandwiched together with the Whatman filter paper as a separator. The assembled electrodes were placed in a test cell rig, few drops of 0.5 M sulfuric acid was added as electrolyte. The test cell is sealed with the O-ring and kept it for few minutes to ensure the uniform soaking of electrodes into

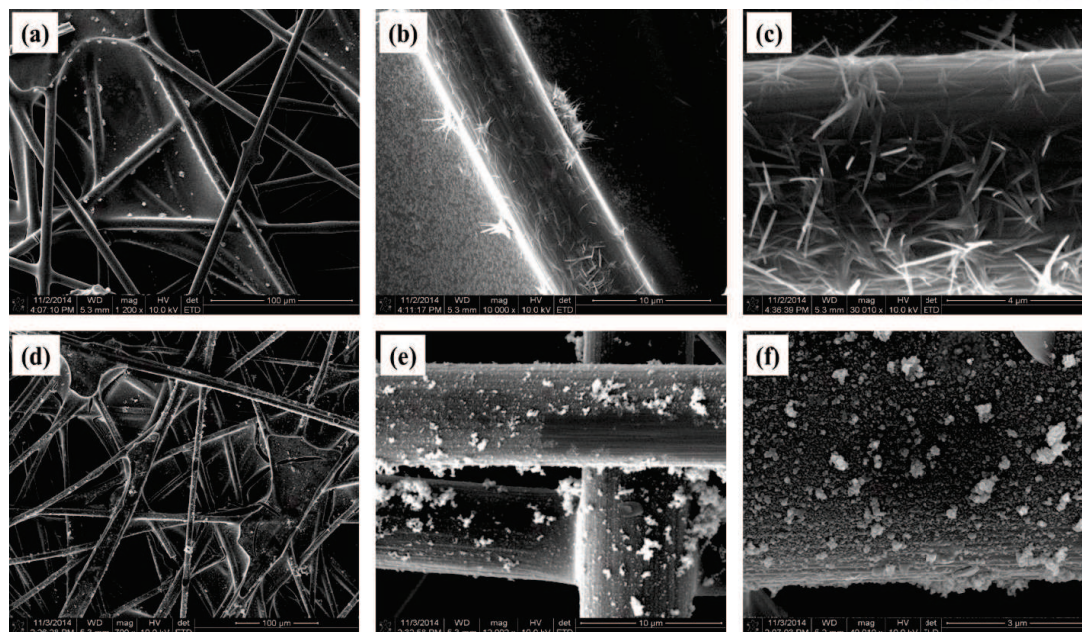


Fig. 8.1 FE-SEM images of (a-c) PC-CFP/a-MoSe_x and (d-f) EE-CFP/a-MoSe_x at different magnifications.

the electrolyte solution prior to the electrochemical measurements. Electrochemical experiments were carried out using a potentiostat/galvanostat (Biologic/VSP) at room temperature. Cyclic voltammograms (CV) and galvanostatic charge/discharge curves were obtained at various scan rates and current densities, respectively. Electrochemical impedance spectroscopy (EIS) measurements were carried out over the frequency range of 0.1 Hz to 100 KHz with the AC amplitude of 10 mV s⁻¹.

8.3 Results and Discussion

8.3.1 Physico-chemical analysis

FE-SEM images of PC-CFP/a-MoSe_x and EE-CFP/a-MoSe_x are shown in Fig. 8.1. Due to the difference in surface activation using plasma cleaning and electro etching process, the different MoSe_x nanostructures are formed on the PC-CFP and EE-CFP. There are less dense uneven distribution of MoSe_x nanoneedles are observed on PC-CFP, where as an uniform coating of MoSe_x nanoparticles are deposited on the EE-CFP. From the XRD (Fig. 8.2), there is no obvious MoSe₂ peaks are observed. The MoSe_x coated on EE-CFP shows only carbon fiber paper peak. From the Raman spectrum (Fig. 8.3) also there is no obvious Raman active modes of MoSe₂ observed, which confirmed the formation of amorphous molybdenum selenide. XPS spectra of MoSe_x coated EE-CFP are shown in Fig. 8.4. A typical survey spectrum of MoSe_x coated EE-CFP is shown in Fig. 8.4a, which indicates the presence of Mo, Se, O and C elements [15, 16]. The high resolution spectrum of Mo 3d displayed in Fig. 8.4b. The two strong peaks appeared at 228.8 and 232.0 eV corresponds to the Mo 3d_{5/2} and Mo 3d_{3/2} spin orbits of Mo-Se bonds [15, 16]. The two minor characteristics peaks located at 229.8 and 235.2 eV can be assigned to the Mo-O bonds. The high resolution Se 2p spectrum (Fig. 8.4c) shows the unresolved broad peak, which upon deconvolution clearly shows the two well-defined peaks at 54.5 and 55.2 eV corresponds to the

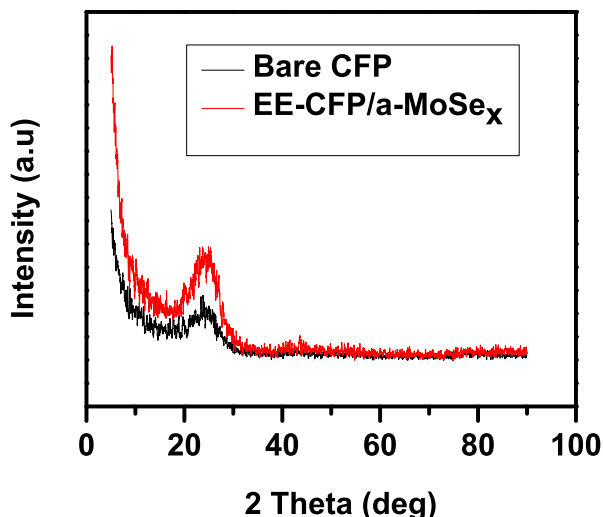


Fig. 8.2 XRD pattern of bare CFP and EE-CFP/a-MoSe_x

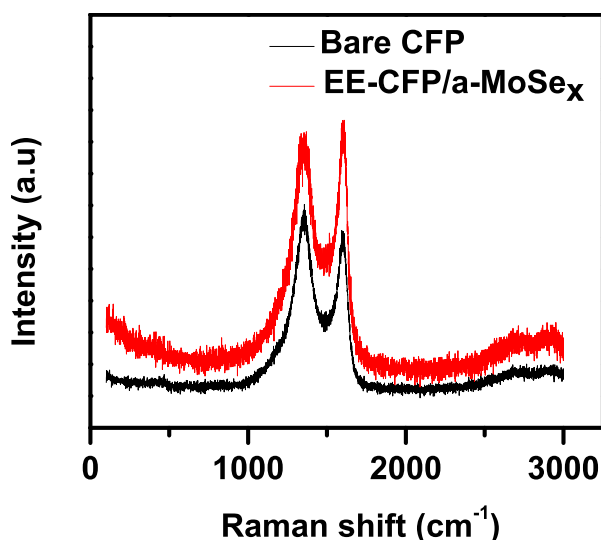


Fig. 8.3 Raman spectra of bare CFP and EE-CFP/a-MoSe_x

binding energies of Se 3d_{5/2} and Se 3d_{3/2} spin orbits of Se-Mo bonds [15, 16]. The presence of O and C (Fig. 8.4d) in MoSe_x coated EE-CFP is un-avoided surface contamination from absorbed gaseous molecules.

8.3.2 Electrochemical performance

The electrochemical performance of the bare-CFP, MoSe_x on plasma cleaned CFP (PC-CFP/a-MoSe_x), and MoSe_x on electrochemical pretreated CFP (EE-CFP/a-MoSe_x) electrodes were investigated using cyclic voltammetry (CV), galvanostatic charge-discharge (GCD) and electrochemical impedance spectroscopy measurements in a two electrode configuration using 0.5 M H₂SO₄ as the electrolyte. As shown in Fig. 8.5, the CV curves of the bare-CFP symmetric supercapacitor, exhibited a typical rectangular shape, demonstrates an electrochemical double layer capacitive behavior (EDLC) of conventional carbon electrodes. However, the symmetric capacitor made of PC-CFP/a-MoSe_x-based electrodes and the sym-

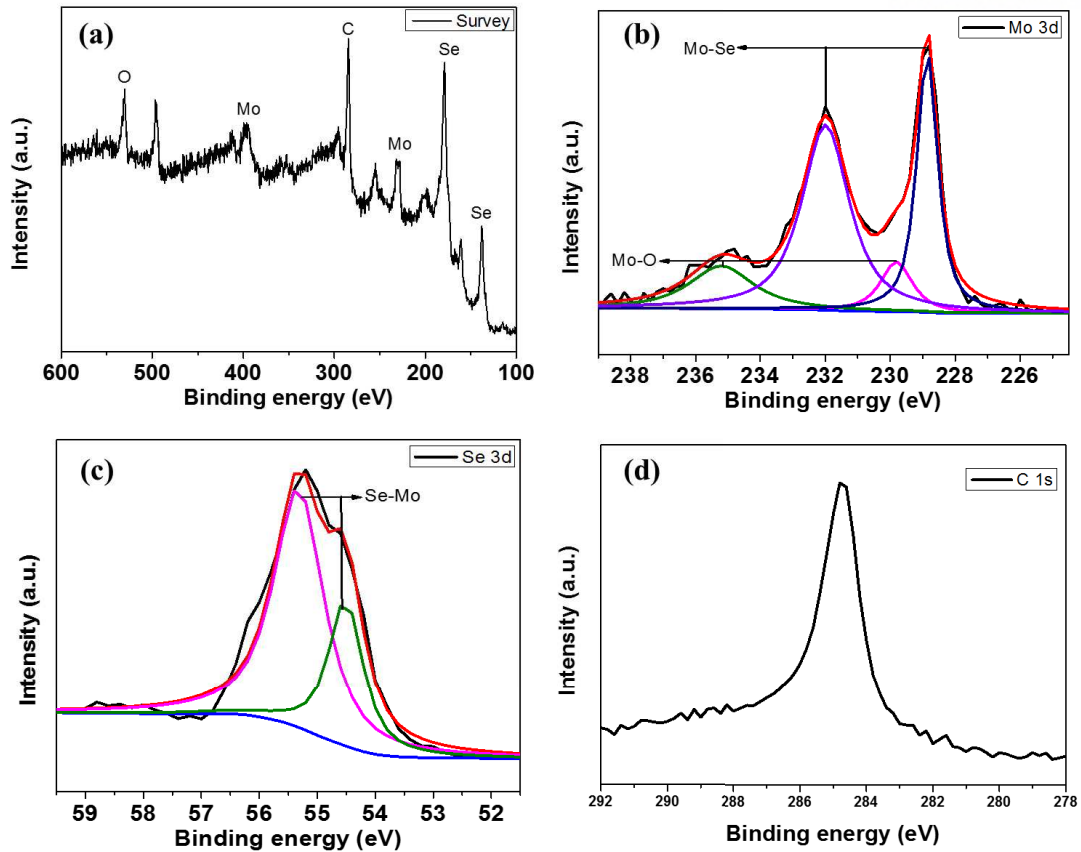


Fig. 8.4 XPS spectra of (a) survey, (b) Mo 3d, (c) Se 3d and (d) C 1s for EE-CFP/a-MoSe_x

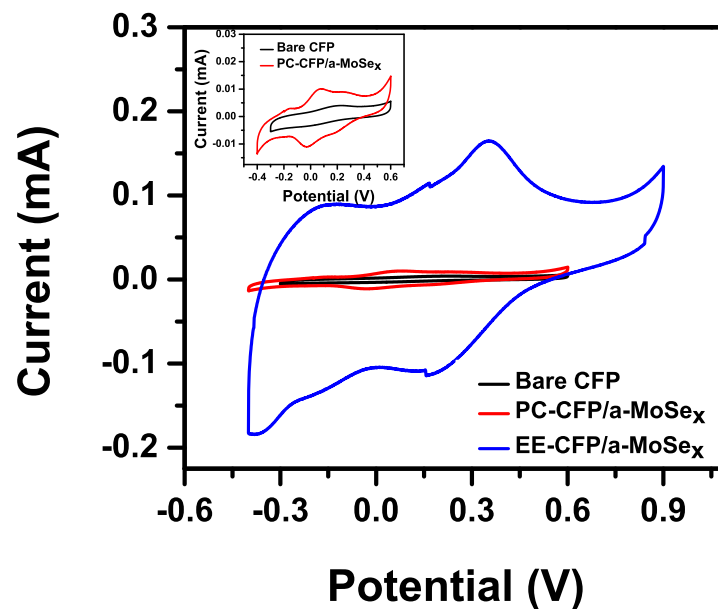


Fig. 8.5 Cyclic voltammetry curves of CFP, PC-CFP/a-MoSe_x and EE-CFP/a-MoSe_x at a scan rate of 5 mV s⁻¹

metric capacitor made of EE-CFP/a-MoSe_x electrodes-based electrodes displayed a quasi-rectangular shape CV curves with a couple of clear redox peaks, which indicates the combination of EDLC with

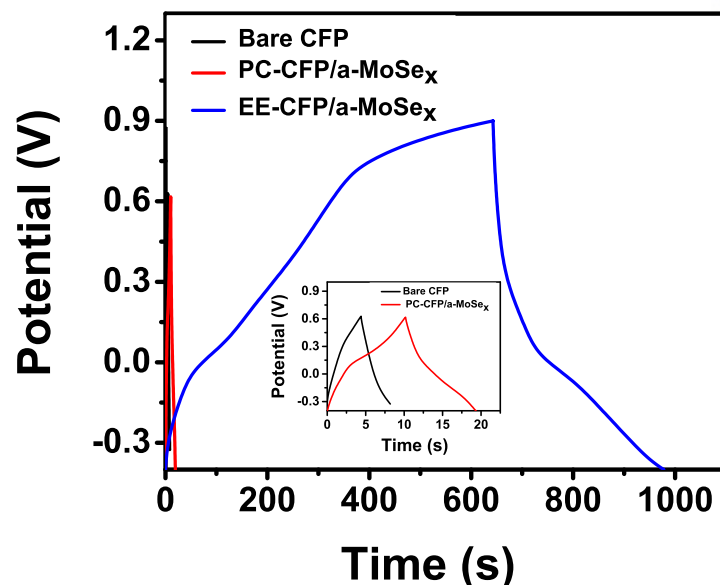


Fig. 8.6 Galvanostatic charge/discharge curves of CFP, PC-CFP/a-MoSe_x and EE-CFP/a-MoSe_x at a current density of 0.1 mA cm⁻².

pseudocapacitive characteristics. The observed anodic/cathodic peaks is related to the redox reaction of molybdenum atoms.

While compared to the bare-CFP based symmetric capacitors, PC-CFP/a-MoSe_x and EE-CFP/a-MoSe_x-based symmetric supercapacitors delivered a larger enclosed area in the CV curve, which demonstrates the high charge-storage capacity in turn the higher specific capacitance value at the same scan rate. Figure. 8.6 represents the galvanostatic charge-discharge curves of the symmetric supercapacitors made using bare-CFP, PC-CFP/a-MoSe_x and EE-CFP/a-MoSe_x electrodes at a constant current density of 0.1 mA cm⁻². The bare CFP-based symmetric capacitor shows symmetrical and triangular in shape GCD curve, which signifying an ideal capacitive behavior. In case of PC-CFP/a-MoSe_x and EE-CFP/a-MoSe_x-based symmetric capacitor the charge-discharge profiles follow non-linear behavior and they showed the voltage plateaus during the charge/discharge process that implies a pseudocapacitive characteristics of the electrodes, which is in well agreement with the CV curves. Also the GCD curve of EE-CFP/a-MoSe_x-based supercapacitors exhibited longer discharge time than the PC-CFP/a-MoSe_x and bare-CFP based capacitors, which indicates the higher capacitance of EE-CFP/a-MoSe_x-based symmetric capacitors.

The CV curves of symmetric supercapacitors based on PC-CFP/a-MoSe_x and EE-CFP/a-MoSe_x electrodes at various scan rates are displayed in Fig. 8.7a and 8.9a, respectively. It can be seen that the CV curves are maintained the quasi-rectangular shape with a couple of redox peaks even at higher scan rates indicating the remarkable capacitive performance attained from the combination of EDLC with pseudocapacitance. With increasing scan rate, the current is also linearly increased. In addition, the anodic and cathodic peaks shifted towards positive and negative potential directions with the rise of scan rates, specified the larger kinetic irreversibility in the redox process due to the increased polarization and ohmic resistance during the faradaic process in electroactive materials [17].

The areal capacitance of a single electrode and the device (symmetric supercapacitors) are calculated from the CV curves according to the Eqs. (2.10) and (2.8). The PC-CFP/a-MoSe_x and EE-CFP/a-

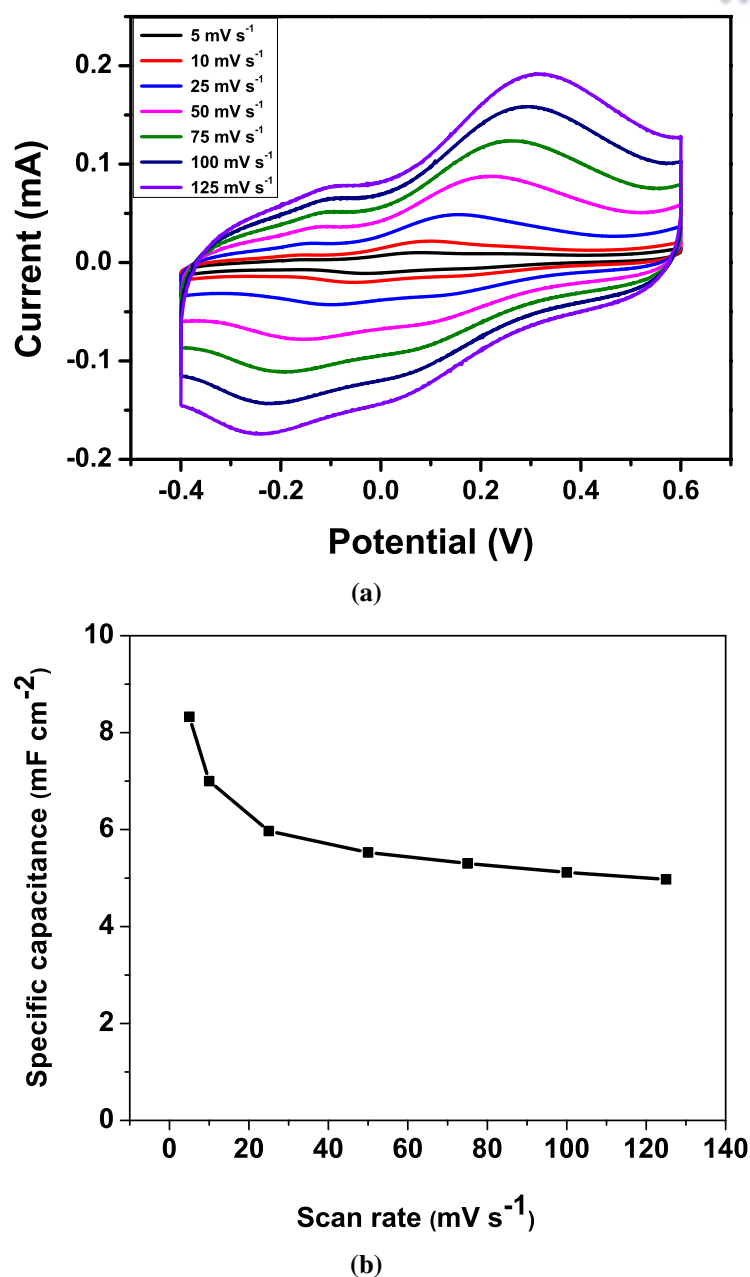


Fig. 8.7 Cyclic voltammety profiles (a) and specific capacitances (b) of PC-CFP/a-MoSe_x-based supercapacitors at various scan rates,

MoSe_x electrodes based-symmetric supercapacitors exhibits the maximum specific capacitance of 8.32 and 101.9 mF cm⁻² at a scan rate 5 mV s⁻¹, respectively. The device capacitance of the symmetric supercapacitors based on PC-CFP/a-MoSe_x and EE-CFP/a-MoSe_x electrodes are 4.16 and 50.95 mF cm⁻², respectively. The relationship between specific capacitances and the scan rates of PC-CFP/a-MoSe_x and EE-CFP/a-MoSe_x are shown in Fig. 8.7b and 8.9b, respectively. It can be seen that, the EE-CFP/a-MoSe_x exhibited a higher specific capacitance than the PC-CFP/a-MoSe_x. The specific capacitances of EE-CFP/a-MoSe_x are calculated to be 154.3, 101.9, 90.3, 79.5, 71.2, 67.9, 66.1, 64.3, 62.8, and 54.8 mF cm⁻² at a scan rates of 2, 5, 10, 25, 50, 75, 100, 125, 200 and 500 mV s⁻¹, respectively. As specified by the outcomes, the specific capacitance decreases gradually with the increase of scan rates,

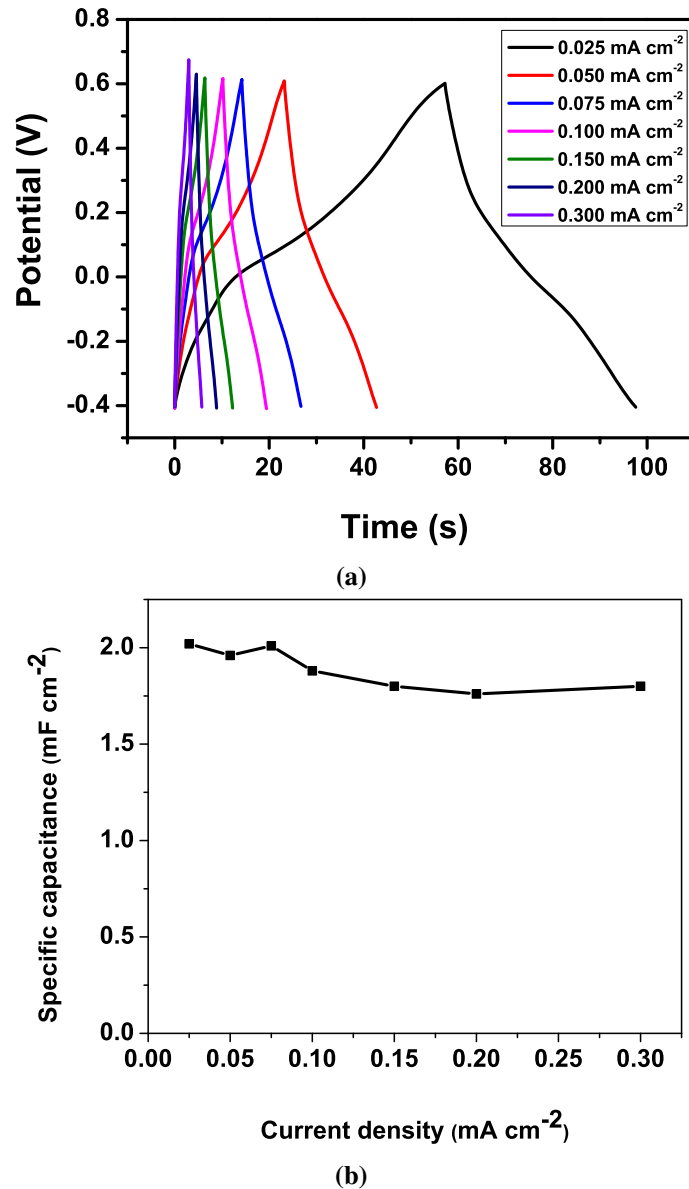


Fig. 8.8 GCD curves (a) and specific capacitances (b) of PC-CFP/a-MoSe_x-based supercapacitors at various current densities.

which can be attributed to the diffusion and migration limitation of electrolytic ions into the electroactive materials (most of the bulk inner electrode region of electrodes are inaccessible for the charge storage) at higher scan rates [18, 19]. Even at the highest scan rate of 500 mV s⁻¹, the EE-CFP/a-MoSe_x still retains 35% of its initial specific capacitance, which is an evidence of high rate capability of this electrode material. The obtained cell capacitance value of EE-CFP/a-MoSe_x electrode-based symmetric supercapacitor (45.15 mF cm⁻² @ 10 mV s⁻¹) is much higher than those of the previously reported MoS₂ (1.83 mF cm⁻² @ 10 mV s⁻¹), graphene-exfoliated MoS₂ (4.29 mF cm⁻² @ 10 mV s⁻¹), and bulk MoS₂ (0.5 mF cm⁻² @ 10 mV s⁻¹). The enhanced electrochemical performance of EE-CFP/a-MoSe_x electrode-based symmetric supercapacitor might be due to the following points: (i) By direct growth of MoSe_x on CFP without any polymeric binders, and conductive additives, lead to the low interfacial resistance, good mechanical adhesion which improves the fast charge transfer rate. (ii) MoSe_x grafted on

the CFP backbone are beneficial for enhancing the electrochemical capacity and cycling stability of the electrode due to the high conductivity, EDLC characteristics and structural stability of CFP. (iii) The three dimensional (3-D) highly porous architecture with a high specific surface area of CFP resulting to the higher mass loading of MoSe_x when compared to the corresponding geometrical area of CFP that ensures a large density of electroactive sites for better ionic transport. (iv) Although, the pseudocapacitive MoSe_x materials having amorphous nature and poor conductivity (when compared to its crystalline counterpart), a thin layer coating of MoSe_x on highly conducting CFP-network reduced the electron/ion diffusion path of the active species and beneficial for the fast penetration of the electrolyte ions into the inner (bulk) region of the MoSe_x thin film which also resulting to an enhanced capacitance and high rate capability. (v) When compared to the surface plasma cleaning process, the electrochemical pretreatment roughens the specific surface area of CFP via formation of more number of oxygen functional group that support the dense MoSe_x nuclei formation and uniform distribution of MoSe_x nanoparticles on the CFP surface. However in case of PC-CFP, plasma cleaning just activate the physical absorption of oxygen functional groups, therefore the less dense and uneven distribution of nanoneedles are formed.

Further to evaluate the rate capability of the symmetric supercapacitors, the galvanostatic charge/discharge test was performed at various current densities. Figure. 8.8a and 8.10a shows the charge/discharge curves for symmetric supercapacitors based on PC-CFP/a- MoSe_x and EE-CFP/a- MoSe_x electrode materials. The GCD curves are obviously non-linear which displays a pair of clear charge/discharge plateau at each curves that indicating the pseudocapacitance characteristics, which is consisted well with the redox properties of CV results. The specific areal capacitances of the symmetric supercapacitors are also calculated from the discharge profiles using Eqs. (2.7) and (2.8). The areal capacitance of the PC-CFP/a- MoSe_x and EE-CFP/a- MoSe_x electrode- based supercapacitors are 1.88 and 51.6 mF cm^{-2} at constant current density of 0.1 mA cm^{-2} , respectively. The cell capacitance of the PC-CFP/a- MoSe_x and EE-CFP/a- MoSe_x electrodes - based symmetric capacitors are 0.94 and 25.8 mF cm^{-2} , respectively. Figure. 8.8b and 8.10b shows the specific capacitance of PC-CFP/a- MoSe_x and EE-CFP/a- MoSe_x electrodes based supercapacitors at various current densities. The specific capacitance of EE-CFP/a- MoSe_x symmetric capacitors remarkably higher than that of the PC-CFP/a- MoSe_x and the capacitance performance of EE-CFP/a- MoSe_x symmetric capacitors is better. The specific capacitance values for the EE-CFP/a- MoSe_x -based supercapacitor (Fig 8.10b) is calculated to be 51.6, 43.5, 41.3, 37.9, 36.4, 35.4, 34.5, 32.9, 31.6, and 27.8 mF cm^{-2} at current densities of 0.1, 0.15, 0.2, 0.4, 0.6, 0.8, 1, 1.5, 2 and 4 mA cm^{-2} , respectively. Further, it can be observed that, the specific capacitance gradually decreases with the increase of charge/discharge current densities, which may be due to the fact that electroactive material cannot fully participate in redox reaction (Diffusion limitation at higher current densities) [20]. Moreover, it can be found that the specific capacitance obtained at a high current density of 4 mA cm^{-2} still retains 54 % of its specific capacitance at 0.1 mA cm^{-2} , specifying the better rate capability, which is significant to the real-world application of the electrode materials for high-performance supercapacitors.

Long-term cycling stability of supercapacitors is an important parameter for practical application of the device in day-to-day applications. Life cycle testing of M PC-CFP/a- MoSe_x (Fig. 8.11a) and EE-CFP/a- MoSe_x (Fig. 8.12a) supercapacitors were conducted by repeated charge/discharge cycling process at galvanostatic mode for 10,000 and 25,000 cycles, respectively. For the PC-CFP/a- MoSe_x based symmetric capacitors, the initial specific capacitance value slightly decreases, which may be due to the

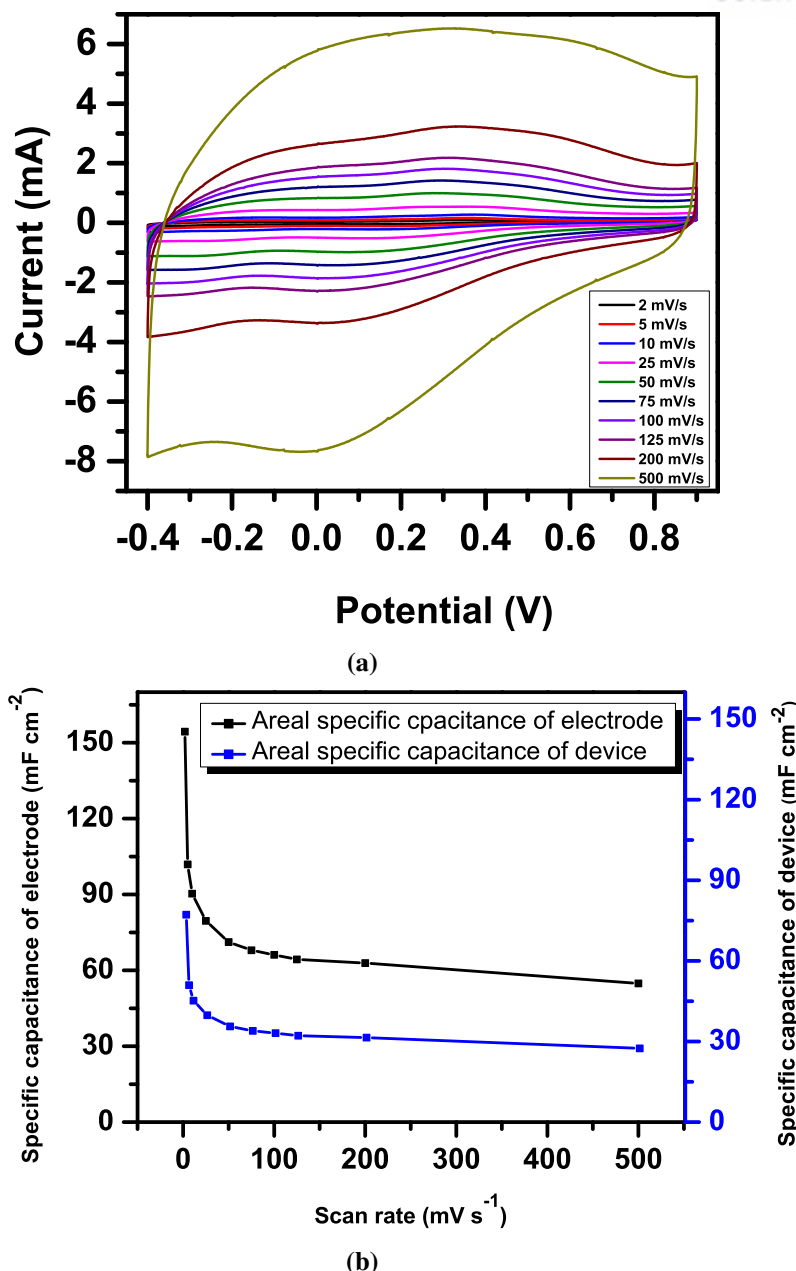
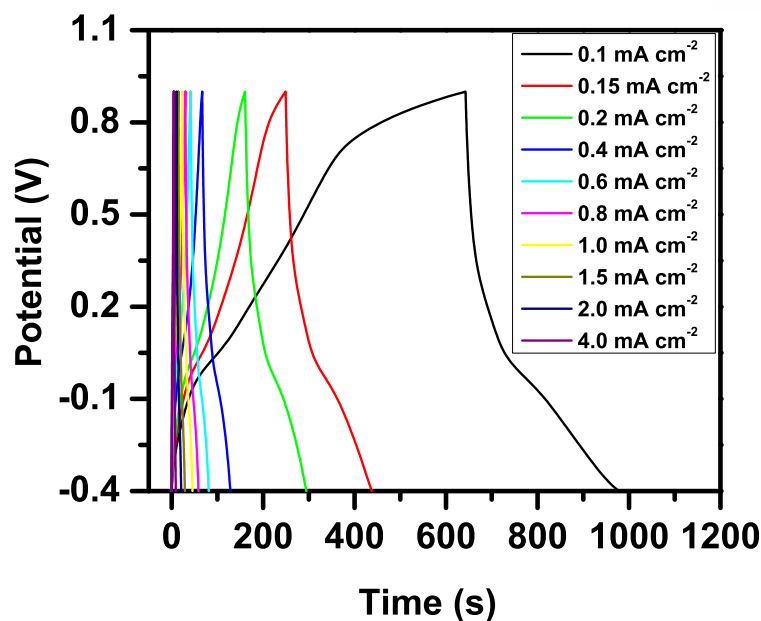
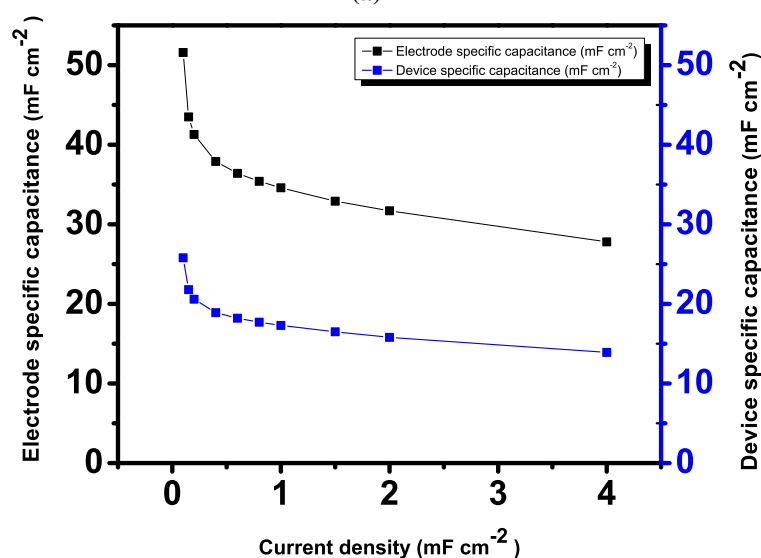


Fig. 8.9 Cyclic voltammety curves (a) and specific capacitances (b) of EE-CFP/a-MoSe_x-based supercapacitors at various scan rates

fact that electroactive materials are not fully activated before 1000 cycles. After 1000 cycles, the specific capacitance in turn the capacitance retention was gradually increased and even after 10,000 cycles 114% capacitance retention was observed. Interestingly, the EE-CFP/a-MoSe_x-based supercapacitors showed gradual increasing trend of specific capacitance and finally even after 25,000 consecutive charge/discharge cycles, the capacitance retention of 150% of the initial capacitance was observed. Furthermore, the increase in specific capacitance with the consecutive charge/discharge process are ascribed to the electro-activation process [13, 21, 22]. Most of the electroactive materials are fully active after several thousands of charge/discharge cycles, resulting the increase in capacitance. These results demonstrate that the symmetric capacitors made of MoSe_x deposited on electrochemical pre-treated CFP (EE-CFP/a-MoSe_x)



(a)

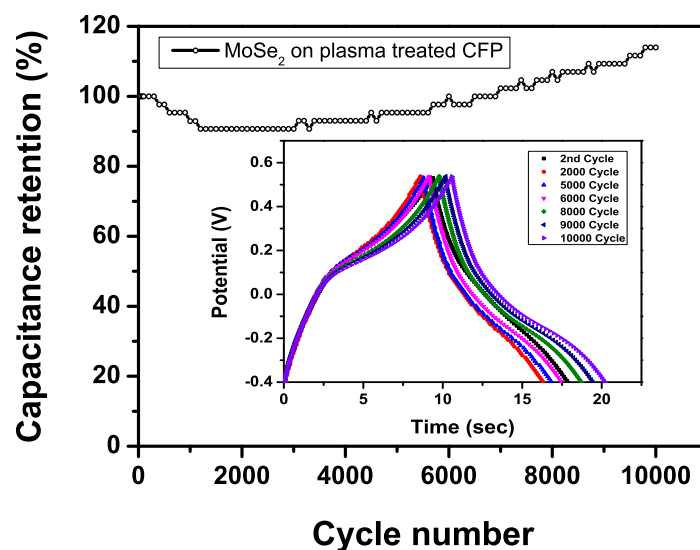


(b)

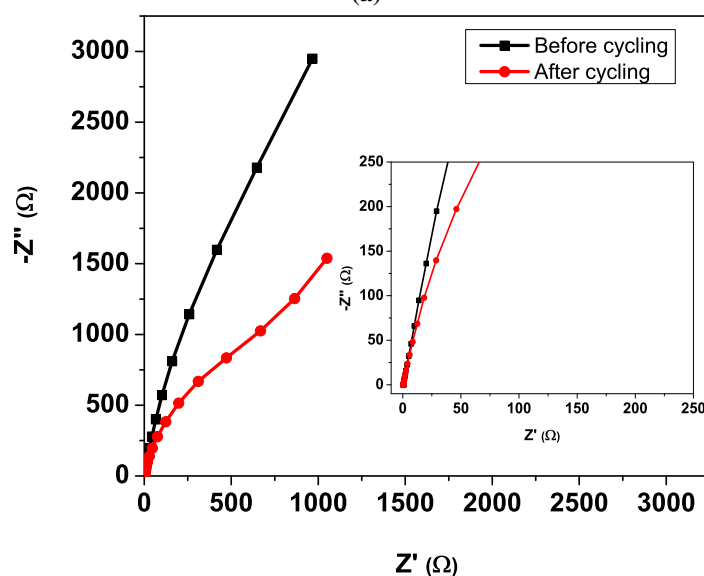
Fig. 8.10 GCD curves (a) and specific capacitances (b) of EE-CFP/a-MoSe_x-based supercapacitors at various current densities.

electrodes showed enhanced energy storage (inturn high specific capacitance), a superior long-term electrochemical stability which confirms that the material could be a promising candidate for next generation high-performance supercapacitors.

In order to further understand the fundamental behavior of the electrodes for supercapacitors, EIS was performed before and after completing charge/discharge cycles. Figure. 8.11b and 8.12b shows the Nyquist plots of PC-CFP/a-MoSe_x (Fig. 8.11b) and EE-CFP/a-MoSe_x (Fig. 8.12b) supercapacitors before and after long-term cycling test. The intercept at the Z-real axis in the high-frequency region is related to the internal resistance (R_s), which is a contribution of solution resistance, the intrinsic resistance of electroactive materials and the contact resistance of electrode-electrolyte interface [23, 24]. The



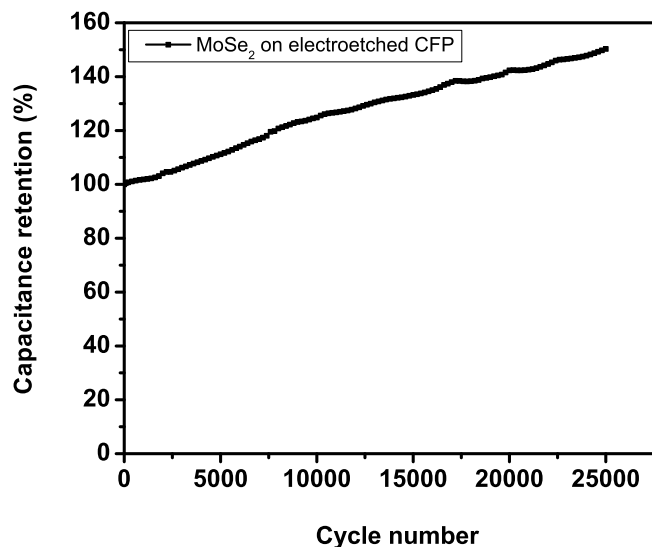
(a)



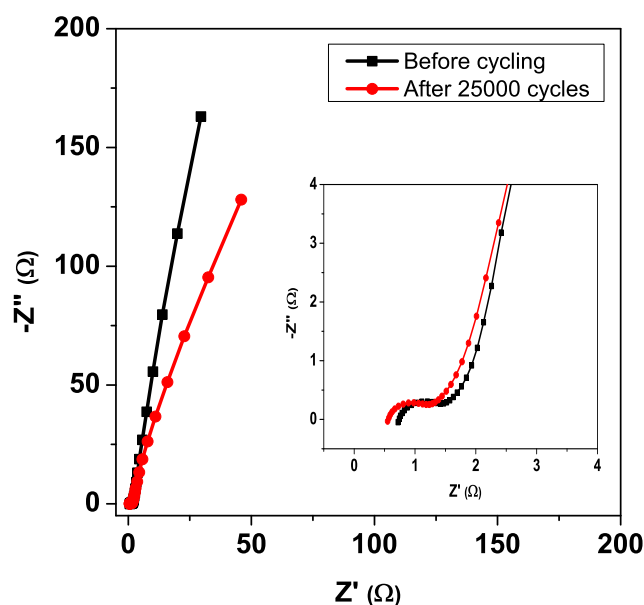
(b)

Fig. 8.11 (a) Cycling performance of PC-CFP/a-MoSe_x-based supercapacitors. (b) EIS spectra of before and after 10000th cycles; inset is the magnified portion of high-frequency region.

internal resistance of the PC-CFP/a-MoSe_x supercapacitor before and after cycling test is 0.41 and 0.34 Ω. Likewise, the internal resistance of EE-CFP/a-MoSe_x supercapacitor is 0.72 and 0.54 Ω. Further, the negligible semicircle at the high-medium frequency region before and after cycling test indicating the better electrical conductivity and fast charge-transfer reaction. The inclined line at low frequency region signifies the diffusion of electrolyte ions. Almost a 90° vertical line to the imaginary axis at low frequency region, indicates an ideal capacitive behavior. After the long-term cycling test, the vertical line at low frequency regions are inclined towards real axis, which indicating the easy access of the electrolyte ions into the electroactive materials (lower diffusion resistance). This result demonstrated that the assembled symmetric supercapacitor showed better electronic conductivity (fast charge transfer process), ionic conductivity, low internal resistance, and well attachment of electroactive material and current collector



(a)



(b)

Fig. 8.12 (a) Cycling performance of EE-CFP/a-MoSe_x-based supercapacitors. (b) EIS spectra of EE-CFP/a-MoSe_x-based supercapacitors before and after 25000th cycles; inset is the magnified portion of high-frequency region.

throughout the cycling process.

8.4 Summary

In summary, the binder free amorphous MoSe_x nanostructures were grown on three-dimensional carbon fiber paper substrate. Due to the different surface pre-treatment conditions of CFP, nanoneedles of MoSe_x are formed on the PC-CFP and nanoparticles are formed on the EE-CFP. The exact mechanism of the effect of pretreatment of CFP on the different MoSe_x nanostructure formation is still under investigation. When compared to the PC-CFP/a-MoSe_x electrode-based symmetric capacitors, EE-CFP/a-MoSe_x electrode-

based symmetric capacitors showed better charge storage behavior. One possible reason may be that PC-CFP has less dense and uneven distribution of MoSe_x nanoneedles, however in the case of EE-CFP, the nanoparticles are uniformly covered all over the surface of CFP.

References

- [1] Ramadoss, A., Saravanakumar, B., Kim, S.J., Vanadium pentoxide/reduced graphene oxide composite as an efficient electrode material for high-performance supercapacitors and self-powered systems, *Energy Technology* 2015, 3 (9), 913–924. doi:[10.1002/ente.201500059](https://doi.org/10.1002/ente.201500059).
- [2] Faraji, S., Ani, F.N., Microwave-assisted synthesis of metal oxide/hydroxide composite electrodes for high power supercapacitors – a review, *Journal of Power Sources* 2014, 263, 338 – 360. doi:[10.1016/j.jpowsour.2014.03.144](https://doi.org/10.1016/j.jpowsour.2014.03.144).
- [3] Lang, X., Hirata, A., Fujita, T., Chen, M., Nanoporous metal/oxide hybrid electrodes for electrochemical supercapacitors, *Nat Nano* 2011, 6 (4), 232–236. doi:[10.1038/nnano.2011.13](https://doi.org/10.1038/nnano.2011.13).
- [4] Pumera, M., Sofer, Z., Ambrosi, A., Layered transition metal dichalcogenides for electrochemical energy generation and storage, *Journal of Materials Chemistry A* 2014, 2 (24), 8981–8987. doi:[10.1039/C4TA00652F](https://doi.org/10.1039/C4TA00652F).
- [5] Shi, F., Li, L., Wang, X.L., Gu, C.d., Tu, J.p., Metal oxide/hydroxide-based materials for supercapacitors, *RSC Advances* 2014, 4 (79), 41910–41921. doi:[10.1039/C4RA06136E](https://doi.org/10.1039/C4RA06136E).
- [6] Snook, G.A., Kao, P., Best, A.S., Conducting-polymer-based supercapacitor devices and electrodes, *Journal of Power Sources* 2011, 196 (1), 1–12. doi:[10.1016/j.jpowsour.2010.06.084](https://doi.org/10.1016/j.jpowsour.2010.06.084).
- [7] Yang, Q., Lu, Z., Liu, J., Lei, X., Chang, Z., Luo, L., Sun, X., Metal oxide and hydroxide nanoarrays: Hydrothermal synthesis and applications as supercapacitors and nanocatalysts, *Progress in Natural Science: Materials International* 2013, 23 (4), 351–366. doi:[10.1016/j.pnsc.2013.06.015](https://doi.org/10.1016/j.pnsc.2013.06.015).
- [8] Balasingam, S.K., Lee, J.S., Jun, Y., Few-layered MoSe_2 nanosheets as an advanced electrode material for supercapacitors, *Dalton Transactions* 2015, 44 (35), 15491–15498. doi:[10.1039/C5DT01985K](https://doi.org/10.1039/C5DT01985K).
- [9] Chia, X., Eng, A.Y.S., Ambrosi, A., Tan, S.M., Pumera, M., Electrochemistry of nanostructured layered transition-metal dichalcogenides, *Chemical Reviews* 2015, 115 (21), 11941–11966. doi:[10.1021/acs.chemrev.5b00287](https://doi.org/10.1021/acs.chemrev.5b00287).
- [10] Huang, K.J., Zhang, J.Z., Fan, Y., Preparation of layered MoSe_2 nanosheets on ni-foam substrate with enhanced supercapacitor performance, *Materials Letters* 2015, 152, 244–247. doi:[10.1016/j.matlet.2015.03.130](https://doi.org/10.1016/j.matlet.2015.03.130).
- [11] Huang, K.J., Zhang, J.Z., Cai, J.L., Preparation of porous layered molybdenum selenide-graphene composites on ni foam for high-performance supercapacitor and electrochemical sensing, *Electrochimica Acta* 2015, 180, 770–777. doi:[10.1016/j.electacta.2015.09.016](https://doi.org/10.1016/j.electacta.2015.09.016).

- [12] Zhang, L.L., Zhao, X.S., Carbon-based materials as supercapacitor electrodes, *Chemical Society Reviews* 2009, 38, 2520–2531. doi:[10.1039/B813846J](https://doi.org/10.1039/B813846J).
- [13] Bissett, M.A., Kinloch, I.A., Dryfe, R.A.W., Characterization of MoS₂ graphene composites for high performance coin cell supercapacitors, *ACS Applied Materials & Interfaces* 2015, 7 (31), 17388–17398. doi:[10.1021/acsami.5b04672](https://doi.org/10.1021/acsami.5b04672).
- [14] Zhu, G., He, Z., Chen, J., Zhao, J., Feng, X., Ma, Y., Fan, Q., Wang, L., Huang, W., Highly conductive three-dimensional MnO₂-carbon nanotube-graphene-ni hybrid foam as a binder-free supercapacitor electrode, *Nanoscale* 2014, 6, 1079–1085. doi:[10.1039/C3NR04495E](https://doi.org/10.1039/C3NR04495E).
- [15] Liu, Y., Zhu, M., Chen, D., Sheet-like MoSe₂/c composites with enhanced li-ion storage properties, *Journal of Materials Chemistry A* 2015, 3, 11857–11862. doi:[10.1039/C5TA02100F](https://doi.org/10.1039/C5TA02100F).
- [16] Huang, Y., Miao, Y.E., Fu, J., Mo, S., Wei, C., Liu, T., Perpendicularly oriented few-layer MoSe₂ on SnO₂ nanotubes for efficient hydrogen evolution reaction, *Journal of Materials Chemistry A* 2015, 3, 16263–16271. doi:[10.1039/C5TA03704B](https://doi.org/10.1039/C5TA03704B).
- [17] Liu, G., Wang, L., Wang, B., Gao, T., Wang, D., A reduced graphene oxide modified metallic cobalt composite with superior electrochemical performance for supercapacitors, *RSC Advances* 2015, 5, 63553–63560. doi:[10.1039/C5RA09748G](https://doi.org/10.1039/C5RA09748G).
- [18] Wang, J., Gao, Z., Li, Z., Wang, B., Yan, Y., Liu, Q., Mann, T., Zhang, M., Jiang, Z., Green synthesis of graphene nanosheets/ZnO composites and electrochemical properties, *Journal of Solid State Chemistry* 2011, 184 (6), 1421–1427. doi:[10.1016/j.jssc.2011.03.006](https://doi.org/10.1016/j.jssc.2011.03.006).
- [19] Ramadoss, A., Kim, G.S., Kim, S.J., Fabrication of reduced graphene oxide/TiO₂ nanorod/reduced graphene oxide hybrid nanostructures as electrode materials for supercapacitor applications, *Cryso-EngComm* 2013, 15 (47), 10222–10229. doi:[10.1039/C3CE41517A](https://doi.org/10.1039/C3CE41517A).
- [20] Ramadoss, A., Kim, S.J., Improved activity of a graphene-TiO₂ hybrid electrode in an electrochemical supercapacitor, *Carbon* 2013, 63, 434 – 445. doi:[10.1016/j.carbon.2013.07.006](https://doi.org/10.1016/j.carbon.2013.07.006).
- [21] Cheng, Q., Tang, J., Ma, J., Zhang, H., Shinya, N., Qin, L.C., Graphene and nanostructured MnO₂ composite electrodes for supercapacitors, *Carbon* 2011, 49 (9), 2917–2925. doi:[10.1016/j.carbon.2011.02.068](https://doi.org/10.1016/j.carbon.2011.02.068).
- [22] Cheng, Q., Tang, J., Ma, J., Zhang, H., Shinya, N., Qin, L.C., Graphene and carbon nanotube composite electrodes for supercapacitors with ultra-high energy density, *Physical Chemistry Chemical Physics* 2011, 13 (39), 17615–17624. doi:[10.1039/C1CP21910C](https://doi.org/10.1039/C1CP21910C).
- [23] Jagadale, A.D., Guan, G., Du, X., Hao, X., Li, X., Abudula, A., Cobalt hydroxide [Co(OH)₂] loaded carbon fiber flexible electrode for high performance supercapacitor, *RSC Adv.* 2015, 5, 56942–56948. doi:[10.1039/C5RA11366K](https://doi.org/10.1039/C5RA11366K).
- [24] Javed, M.S., Dai, S., Wang, M., Xi, Y., Lang, Q., Guo, D., Hu, C., Faradic redox active material of Cu₇S₄ nanowires with a high conductance for flexible solid state supercapacitors, *Nanoscale* 2015, 7, 13610–13618. doi:[10.1039/C5NR03363B](https://doi.org/10.1039/C5NR03363B).

CHAPTER 9

Concluding Remarks and Future Prospects

In the present study, various nanostructured materials are synthesized and investigated for supercapacitor applications which include transition metal oxides, transition metal dichalcogenides, and their carbon based composite materials. The transition metal oxide based materials include vanadium pentoxide (V_2O_5) and graphene decorated V_2O_5 nanobelts (GVNBs); the transition metal dichalcogenide based materials include molybdenum sulfide (MoS_2), amorphous molybdenum sulfide thin-layer coated carbon fiber paper (CFP/a- MoS_x), molybdenum selenide nanosheets ($MoSe_2$), molybdenum selenide/reduced graphene oxide hybrid structures ($MoSe_2/rGO$), and amorphous $MoSe_x$ nanostructures coated carbon fiber paper (CFP/a- $MoSe_x$). The nanostructured materials are synthesized using facile hydrothermal method. The physico-chemical properties of these materials are well characterized, and also the electrochemical energy storage performance is assessed for supercapacitor applications.

In the first part of the thesis (**Chapter 3**), the low temperature hydrothermal process is developed for the synthesis of GVNBs using graphene oxide as a mild oxidizing agent. In comparison to the bulk V_2O_5 materials, the as-synthesized GVNBs show enhanced electrochemical charge storage behavior which can be attributed due to the insertion of rGO into the layered V_2O_5 crystalline structure which further enhances the conductivity of GVNBs. Three different compositions of V_2O_5 and rGO materials are synthesized. The V_2O_5 rich composition shows the highest gravimetric specific capacitance of 288 F g^{-1} at a scan rate of 10 mV s^{-1} .

Although GVNBs possess good conductivity and exhibit high charge storage behavior, one of the key issues of pristine transition metal oxides (TMOs) is the poor electrical conductivity. To improve upon this issue, the transition metal dichalcogenide (TMDCs) based materials having higher electrical conductivity than TMOs, two-dimensional layered crystal structure with high surface area have been focused in this section. **Chapter 4** present the synthesis of freeze-dried MoS_2 nanosponge electrodes with high surface area along with the evaluation of their electrochemical performance for symmetric supercapacitors. The maximum specific capacitance of 510 A g^{-1} is recorded at a scan rate of 2 mV S^{-1} . In addition to the synthesis of freeze-dried MoS_2 crystalline material, a novel approach is developed for the synthesis of amorphous molybdenum sulfide on the highly conducting CFP substrate (**Chapter 5**). When compared to the crystalline MoS_2 electrode material, the amorphous structure having defect sites acts like a diffusion channel for electrolyte ion diffusion thereby enhancing the electrochemical charge storage characteristics.

In comparison to MoS_2 , molybdenum selenide based materials are rarely studied for supercapacitor application. To this end, as described in **Chapter 6**, molybdenum selenide nanosheets are synthesized using hydrothermal method and their supercapacitor properties are studied under two-electrode symmetric

cell configuration. The specific capacitance of MoSe_2 is much lower than MoS_2 which may be due to the presence of larger size selenium ions present in the two-dimensional MoSe_2 crystal structure. In order to improve the charge storage property, the MoSe_2 nanosheets are synthesized with reduced graphene oxide (rGO) nanosheets having high conductivity (**Chapter 7**). Due to the synergistic effect of Faradaic reaction (from MoSe_2) and non-Faradaic reaction (from rGO), the overall energy storage properties show a remarkable increase. The last chapter (**Chapter 8**) presented the formation of amorphous molybdenum selenide nanostructures on the highly conducting three dimensional substrate (CFP). Since CFP is hydrophobic in nature, the different pre-treatments (physical and electrochemical) such as plasma cleaning and electro etching are employed. Although the same experimental conditions are used for the growth of molybdenum selenide on both of the pre-treated CFPs, interestingly, the different morphologies of MoSe_x nanostructures are observed on plasma cleaned CFP and electro etched CFP. Additionally, the electrochemical performance of MoSe_x on electro etched CFP is shown to be much higher than that of MoSe_x on plasma cleaned CFP. The synthesis of various transition metal compounds and their carbon composites demonstrate the feasibility of these materials for application in high energy density supercapacitors.

The present study focused on the facile synthesis of nanomaterials, and their extensive physico-chemical and electrochemical characterizations. However, the growth mechanism of the amorphous phase of molybdenum sulfide and molybdenum selenide on the carbon fiber paper substrate is yet unclear even under high-temperature hydrothermal conditions. In the absence of carbon fiber paper, the as-formed MoS_2 and MoSe_2 retain their crystalline states. However, when the TMDCs are grown on CFP, such a crystalline structure is lost. This particular behavior of the growth mechanism demands further investigations for the future work.

APPENDIX A

Graphene Decorated V_2O_5 Nanobelts

A.1 Raman spectrum of GNVBs

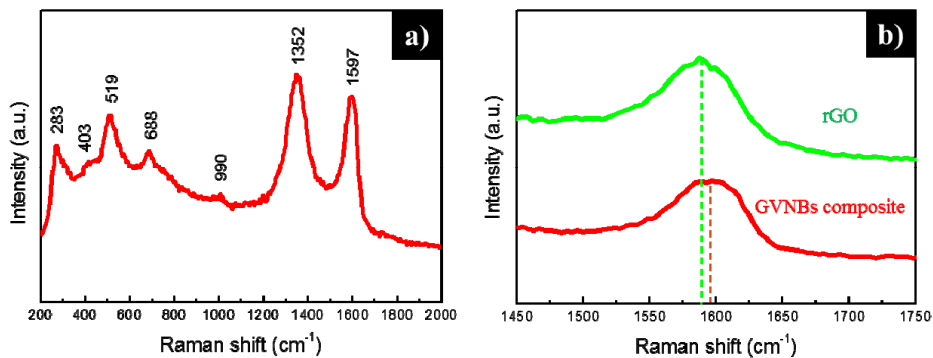


Fig. A.1 Raman spectra of (a) GNVBs (V_3G_1) composites and (b) comparison between the G bands of rGO and GNVBs composites.

A.2 XPS spectra of V2p

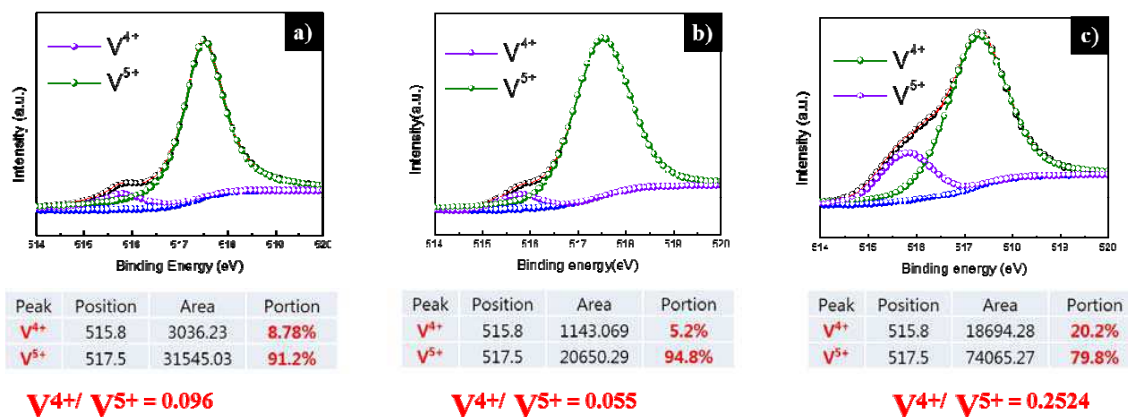


Fig. A.2 XPS spectrum of (a) V_2O_5 raw particles, (b) V_2O_5 mixed with GO in DI water after 1 day, (c) GNVBs (V_3G_1) after hydrothermal treatment.

A.3 XPS spectra of C1s

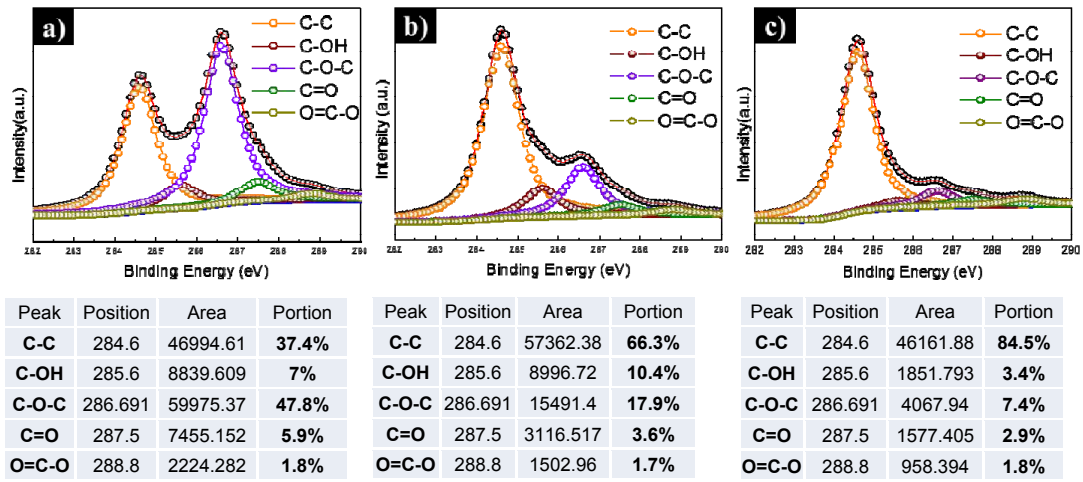


Fig. A.3 C1s XPS spectra of (a) GO before the hydrothermal treatment, (b) GO without V_2O_5 after the hydrothermal treatment, (c) mixture of GO and V_2O_5 (V_3G_1) after the hydrothermal treatment.

A.4 AFM image of GNVBs

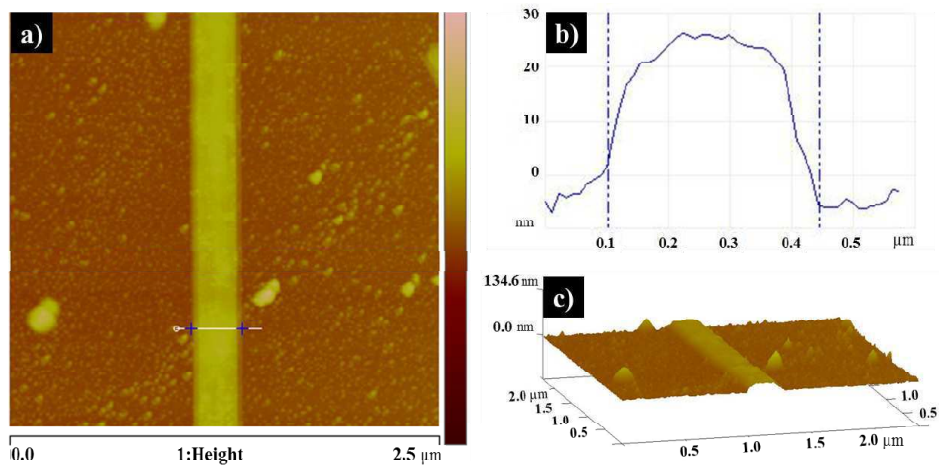


Fig. A.4 (a) AFM image of GNVBs prepared in the ratio V_3G_1 , (b) thickness analysis along the white line shown in frame (a), and (c) surface topographical AFM image of GNVBs.

APPENDIX B

Freeze-dried MoS₂ Nanosponges

B.1 SEM images of normal-dried MoS₂ particles and freeze-dried MoS₂ sponge materials

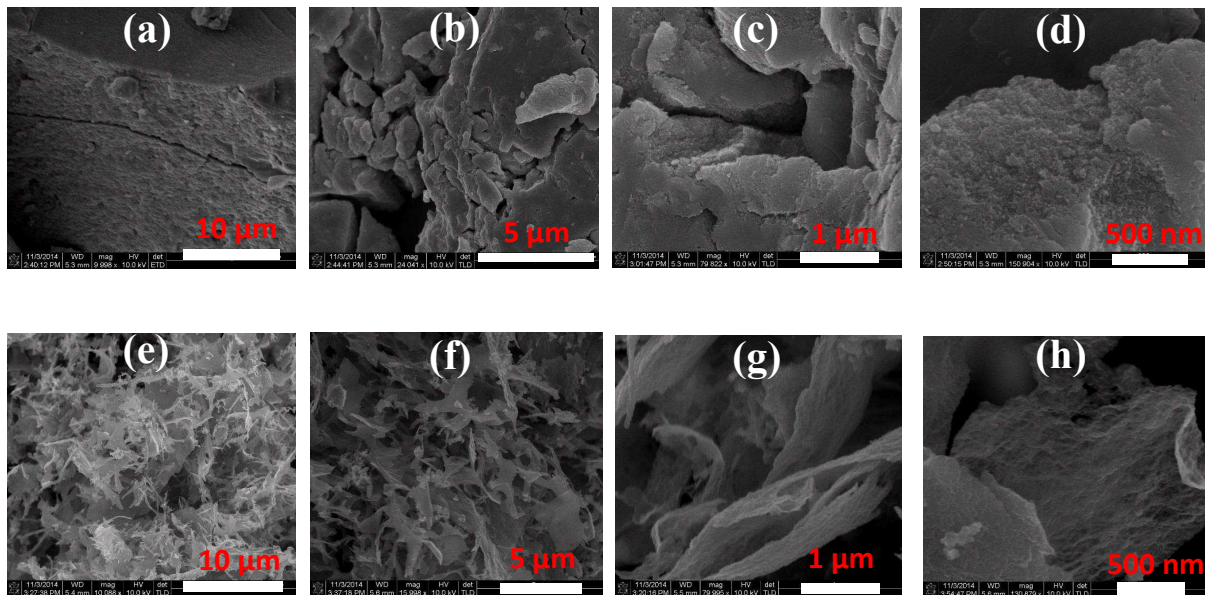


Fig. B.1 Scanning electron microscopic images of hydrothermally synthesized MoS₂ material. The agglomerated MoS₂ microparticles obtained by the normal air-drying method at various levels of magnification are shown in (a)-(d). The high surface area MoS₂ sponge electrodes obtained by freeze-drying method at various magnifications are shown in (e)-(f). For comparison purposes, similar scale bars are used.

APPENDIX **C**

Amorphous MoS_x Thin-layer Coated CFP

C.1 XRD pattern of amorphous MoS_x thin film coated CFP

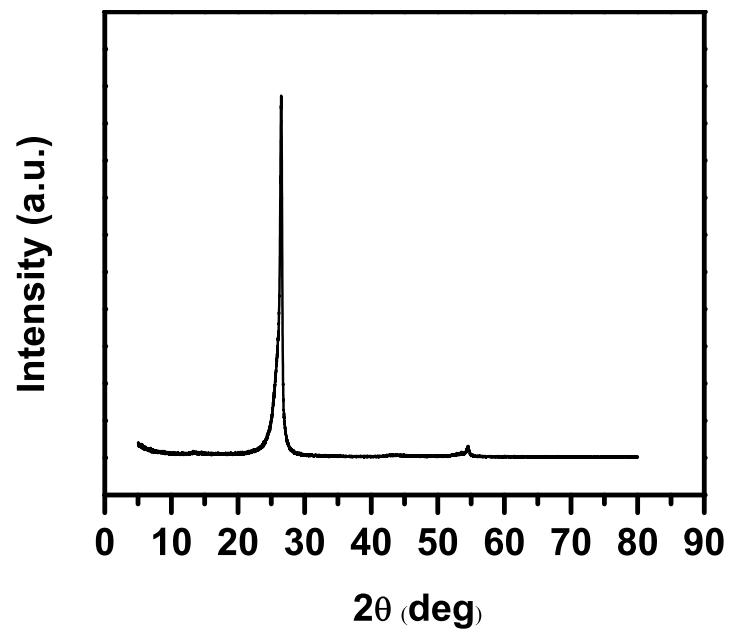


Fig. C.1 X-ray diffraction pattern of CFP/a-MoS_x showing the characteristic peak of CFP. No characteristic peaks of MoS₂ are observed.

C.2 Raman spectrum of amorphous MoS_x thin film coated CFP

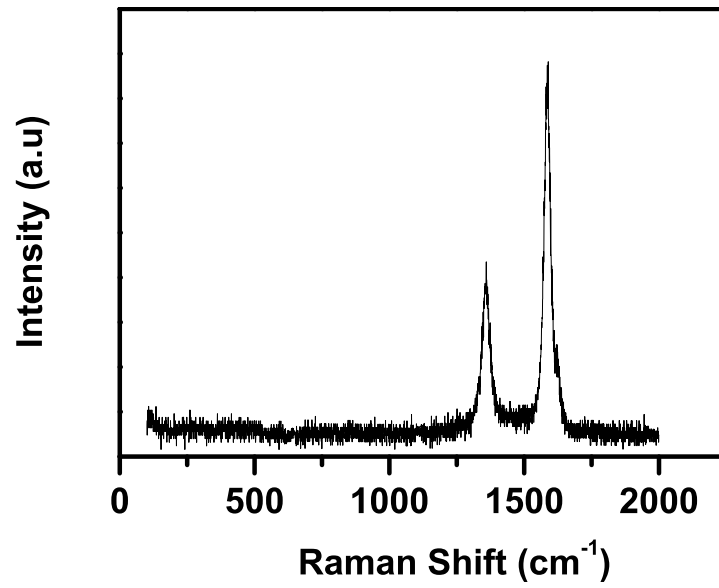


Fig. C.2 Raman spectrum of CFP/a- MoS_x . No distinctive Raman active modes of MoS_2 are observed.

List of Publications

1. Balasingam, S.K., Lee, J.S., Jun, Y., Few-layered MoSe₂ nanosheets as an advanced electrode material for supercapacitors, Dalton Transactions 2015, 44, 15491–15498. doi:10.1039/C5DT01985K
2. Lee, M., Balasingam, S.K.*, Jeong, H.Y., Hong, W.G., Lee, H.B.R., Kim, B.H., Jun, Y., One-step hydrothermal synthesis of graphene decorated V₂O₅ nanobelts for enhanced electrochemical energy storage, Scientific Reports 2015, 5. doi:10.1038/srep08151. *Equally contributed with First Author
3. Balasingam, S.K., Jun, Y., Recent progress on reduced graphene oxide-based counter electrodes for cost-effective dye-sensitized solar cells, Israel Journal of Chemistry 2015, 55, 955–965. doi:10.1002/ijch.201400213
4. Bose, R., Balasingam, S.K.* , Shin, S., Jin, Z., Kwon, D.H., Jun, Y., Min, Y.S., Importance of hydrophilic pretreatment in the hydrothermal growth of amorphous molybdenum sulfide for hydrogen evolution catalysis, Langmuir 2015, 31 (18), 5220–5227. doi:10.1021/acs.langmuir.5b00205. *Equally contributed with First Author
5. Lee, M., Hong, W.G., Jeong, H.Y., Balasingam, S.K., Lee, Z., Chang, S.J., Kim, B.H., Jun, Y., Graphene oxide assisted spontaneous growth of V₂O₅ nanowires at room temperature, Nanoscale 2014, 6 (19), 11066–11071. doi:10.1039/C4NR01780C
6. Balasingam, S.K., Lee, M., Kang, M.G., Jun, Y., Improvement of dye-sensitized solar cells toward the broader light harvesting of the solar spectrum, Chemical Communications 2013, 49 (15), 1471–1487. doi:10.1039/C2CC37616D
7. Balasingam, S.K., Kang, M.G., Jun, Y., Metal substrate based electrodes for flexible dye-sensitized solar cells: fabrication methods, progress and challenges, Chemical Communications 2013, 49 (98), 11457–11475. doi:10.1039/C3CC46224B
8. Lim, J., Lee, M., Balasingam, S.K., Kim, J., Kim, D., Jun, Y., Fabrication of panchromatic dye-sensitized solar cells using pre-dye coated TiO₂ nanoparticles by a simple dip coating technique, RSC Advances 2013, 3 (14), 4801–4805. doi:10.1039/C3RA40339D
9. Ko, K.W., Lee, M., Sekhon, S.S., Balasingam, S.K., Han, C.H., Jun, Y., Efficiency enhancement of dye-sensitized solar cells by the addition of an oxidizing agent to the TiO₂ paste, ChemSusChem 2013, 6 (11), 2117–2123. doi:10.1002/cssc.201300280
10. Venkatkarthick, R., Elamathi, S., Sangeetha, D., Balaji, R., Balasingam, S.K., Vasudevan, S., JonasDavidson, D., Sozhan, G., Ravichandran, S., Studies on polymer modified metal oxide anode for oxygen evolution reaction in saline water, Journal of Electroanalytical Chemistry 2013, 697, 1–4. doi:10.1016/j.jelechem.2013.02.015

List of Submitted Articles

1. Balasingam, S.K., Lee, M., Lee, J.S., Jun, Y., Freeze-dried MoS_2 sponge electrodes for high performance supercapacitors, 2016.
2. Balasingam, S.K., Lee, J.S., Jun, Y., Amorphous MoSe_x nanostructures coated three-dimensional electrodes for symmetric supercapacitors, 2016.
3. Balasingam, S.K., Lee, J.S., Jun, Y., Graphene- MoSe_2 based nanocomposites for enhanced electro-chemical energy storage, 2016.
4. Balasingam, S.K., Lee, J.S., Jun, Y., Amorphous MoS_2 thin-layer coated 3D electrode material for long-cycle life supercapacitors, 2016.

Acknowledgments

First of all, I thank the 'GOD ALMIGHTY' for showering me the abundant blessings, strength, and wisdom to achieve this task successfully.

I wish to thank Late Prof. Su Moon Park, an eminent electrochemist and the former chair-professor in school of energy engineering for the introduction of UNIST, a world class university for my doctoral course.

I avail this opportunity with great pleasure to ensure my unfathomable gratitude and whole hearted thanks to my former advisor (in UNIST, 2012-2013) & present informal co-advisor, Prof. Yongseok Jun, Department of Materials Chemistry and Engineering, Konkuk University. During my PhD course, I always admired by his incessant guidance, thought provoking ideas, valuable advices, constructive criticism, and constant encouragement for my doctoral research.

With profound sense of gratitude, I thank my advisor Prof. Jae Sung Lee, Vice President for Academic Affairs, Dean of Graduate School, and School of Energy and Chemical Engineering for his timely support to accept me as a PhD student when Prof. Yongseok Jun moved out of UNIST in 2013. I am thankful to him for all the motivation, encouragement, and valuable suggestions that he has given me. Kindness and concern for his students is an innate trait of him that deserves to be acknowledged.

There are no suitable words to express my ineffable sense of gratitude to my friend, Dr. Ananthakumar Ramadoss for his constant support, guidance, advice, and encouragement in both research and personal life help me to complete this task successfully in a designated time frame.

I wish to express my heartfelt and profound thanks to Mr. Jae-Young Park and Dr. Minoh Lee, former solarinno laboratory members, for their kind hearted help in research and my day-to-day life in Korea.

My earnest gratefulness to my friend & research guru, Dr. S. N. Karthick, Postdoctoral Researcher, Pusan National University for the initial inspiration and constant motivation through out my research career.

I am very much thankful to Mr. Manoj Kumar Dhadwal, Doctoral candidate, Department of Aerospace Engineering, Konkuk University, for the motivation to use \LaTeX typesetting software and proof-reading of my thesis. I am so grateful for his continuous assistance during the preparation of my PhD thesis.

I extend my heart-felt thanks to my friend Dr. T. Arun, Postdoctoral Researcher, Institute of Physics, India for his assistance in TEM-software and the proof-reading of my full thesis. I am so grateful to Dr. Azhagurajan Mukkannan, Postdoctoral Researcher, Tohoku University, for the support of 3D software and his constant motivation during my doctoral course.

It gives me an immense pleasure to express my gratitude to the current and former members of our research team, Dr. Yimhyun Jo, Dr. Jeongmin Lim, Dr. Cholong Jung, Mr. Jeonghun Yu, Ms. Hyun A Kim, Mr. Wooyeol Choi, Mr. Seong Young Kong, Dr. Yong Ju Yun, Mr. Yohan Ko, Mr. Chan Young Lee, and Ms. Young-lim Kim, for their constant support, helps rendered in the laboratory and valuable discussion during the weekly meetings to complete this research work successfully.

I express my sincere thanks to my former advisors, Dr. S. Vasudevan, Dr. S. Ravichandra and Dr. G. Sozhan, Scientists at Electroinorganic Chemicals Division, Central Electrochemical Research Institute, India, who initiated my research career and actively directed me in the research with constant support, encouragement, and enthusiastic advice.

I wish to thank Prof. P. Manisankar, Syndicate Member, Dean of Research, Head of the Department of Industrial Chemistry, Alagappa University, India for his constant support and motivation even after completion of my Master's course. I extend my sincere thanks to Prof. T. Vasudevan, a former Professor & Head, Department of Industrial Chemistry, Alagappa University and Prof. A. Subramania, Madanjeet School of Green Energy Technologies, Pondicherry University for their great support during my Master's course.

I would like to express my thanks to the former advisors, Dr. Karin Vels Hansen, and Prof. Torben Jacobsen, Technical University of Denmark, for the motivation, encouragement, and valuable suggestions during my research stay at DTU.

I wish to express my heartfelt and profound thanks to the following close friends and colleagues: Dr. Mohammed Hussain Abdul Jabbar, Dr. J. Anandharaj, Er. Muthupandi, Er. Rajesh Kumar, Prof. K. V. Hemalatha, Prof. D. Ragupathy, and Prof. C. Justin Raj for their constant support during the course of my PhD study.

I wish to extend my thanks to my UNIST friends: Dr. Sivaprakash Sengodan, Dr. Pradheep Thiyagarajan, Dr. Lalit Rajput & Dr. Magesh Ganesan; My Jeju friends: Dr. Thiyagu, Dr. Saravanakumar, Mr. Alluri & Mr. Arun; and all my friends in Busan & Seoul (numbers are too many).

Last, but certainly not the least, I must acknowledge with tremendous and deep thanks to my family members. I thank my beloved mother Mrs. Veerammal Balasingam who has dedicated her whole life for the betterment of my tomorrow with love and gratitude. Words can hardly substitute the debt that I owe to my inspiring brother Mr. Senthil Kumar Balasingam & family, and Mr. Pandiyarajan & family who stood behind me in all possible ways to complete this work successfully. Without the support of above members, I might have not been able to complete this research work.

Finally, my thanks are due to all those who have helped me directly or indirectly for the successful completion of my research work.

Suresh Kannan Balasingam

